Università degli Studi di Milano Bicocca

Dottorato di Ricerca in Scienza dei Materiali
XXVI ciclo

UNIVERSITA' DEGLI STUDI DI MILANO BICOCCA

CHARACTERIZATION OF DEFECTS AT THE INTERFACE BETWEEN GERMANIUM AND OXIDES BY ELECTRICALLY DETECTED MAGNETIC RESONANCE AND ADMITTANCE SPECTROSCOPY

Stefano Paleari

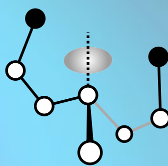

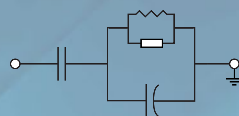

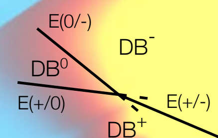

Università degli Studi di Milano Bicocca

Dottorato di Ricerca in Scienza dei Materiali
XXVI ciclo

CHARACTERIZATION OF DEFECTS AT THE INTERFACE BETWEEN GERMANIUM AND OXIDES BY ELECTRICALLY DETECTED MAGNETIC RESONANCE AND ADMITTANCE SPECTROSCOPY

Stefano Paleari

Relatore:
Professor Marco Fanciulli

Commissione:
Professor Emanuale Grilli
Professor Franco Marabelli
Professor Lamberto Duò

2 Luglio 2014

Non tutti gli spettri
riescono col picco

Introduction

Germanium has been the subject of a renewed interest as a promising material for future electronic devices. In particular its integration as channel material within Complementary-Metal-Oxide-Semiconductor (CMOS) architectures, the most widespread technology of integrated circuits, would be beneficial in terms of speed and energy performance.
Germanium is not new to the semiconductor industry. The early days of electronics, indeed, involved almost only Ge diodes and *Bipolar Junction Transistor* technology. Silicon took over as the dominant material in electronics after the discovery of the SiO_2 passivation of the interfaces and the planar *Metal Oxide Semiconductor Field Effect Transistor* (MOSFET).
What hindered the development of Ge was the poor characteristics of its oxide, contrasting the excellent properties of the Si/SiO_2. GeO_2 is quite unstable, it is prone to form compounds with different stoichiometry, and it is dissolved by water. Defects at the Ge/GeO_2 interface are not readily passivated and the standard *Forming Gas Annealing* adapted from the silicon process flow is ineffective. Therefore, the realization of performance gains is strictly bound to the physical identification of the interface traps and the development of new passivation strategies.

Context

Transistor scaling has been the driving force in semiconductor industry ability to increase exponentially the performance of the devices since the early '70s. The number of components per chip has doubled every two years along more than forty years and this historical trend has become known as "Moore's law" (Moore, 1965). The total chip size needs to be within practical limits, and the growth in terms of components can be achieved by continuous downscaling of the dimension of the building units. In terms of Moore's law, the gate length scales as $\approx 1/\sqrt{2}$ every two years. The continuous increase in the integration density was made possible by a dimensional scaling described by Dennard et al. (1974) and illustrated in Fig. 1: in CMOS technology, reducing the critical dimensions while keeping the electrical field constant, higher speed and a reduced power consumption are obtained at the same time.

To keep up with the trend as atomic dimension are nudging, new materials need to be incorporated into the devices and new transistor concepts must be applied. This

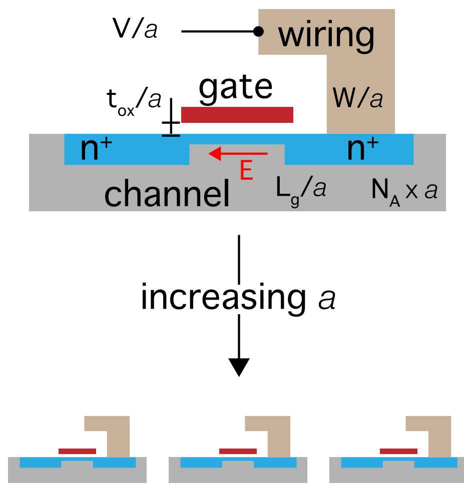

Figure 1: Constant field scaling theory described by Dennard et al. (1974). Reduction in transistor size benefits operation speed and power consumption (ITRS).

approach is within the framework of Moore's law and is labeled "More Moore". A complementary view identified by the expression "More than Moore" is under development in the last years, aiming at functional diversification. This aims at extending the application of integrated circuits, beyond logic and memory, to the interaction with the outside environment. The heterogeneous integration of digital and non-digital worlds into compact systems involve micro-mechanical systems, analog and mixed signal processing units, high performance capacitors, micro-fluidics devices, to bring together on the same platform different functionalities such as movement and magnetic field detection, microwave band communication, energy storage, and biological application such as DNA detection and sequencing.

Germanium as a Booster for Future Electronic Devices

In a *more Moore* approach, mobility is an essential parameter to improve the efficiency of MOSFET devices. Strain engineering has been applied to silicon channels since 2003 to increase drive current and, ultimately, speed (Thompson and Parthasarathy, 2006). Germanium, on the other hand, possesses an intrinsic high mobility for electrons and one of the highest hole mobilities among widespread semiconductors as shown in Fig. 2. (Pillarisetty, 2011).

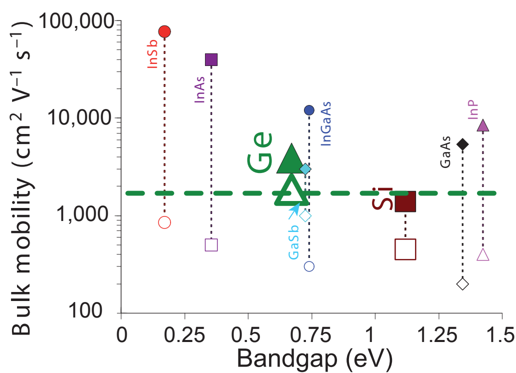

Figure 2: Bulk mobility and bandgap for mainstream group IV and III-V semiconductors. Filled symbols indicate electron and open symbols indicate hole mobility, respectively. Adapted from (Pillarisetty, 2011).

Moreover, the comparatively small bandgap of Ge enables low operating voltage with beneficial effect on the power consumption and heat generation. On the other hand, the bandgap is not too small, and low off-state leakage current may be achieved by careful device structure design.

Additionally, germanium is easier to integrate on the silicon platform with respect to III-V compounds and it raises less stringent requirements from the health and environmental points of view. These are needed considerations in a Very Large-Scale Integration (VLSI) implementation. The main issue is represented by the lattice mismatch between Si and Ge, but it can be addressed by means of graded SiGe alloys as buffer layers.

Furthermore, germanium is a promise in the "More than Moore" approach, too. The higher hole mobility, long spin coherence time, and accessibility to the direct gap would benefit spintronics, photonics, photovoltaics, and optoelectronics applications (Xiang et al., 2006; Jain et al., 2012; Assefa et al., 2010; Kouvetakis and Chizmeshya, 2007).

The Interface Issue

Ge oxides exist in different stoichometry and atomic structures. Most are soluble in water and for this reason old Ge diodes were enclosed in a glass shell. An example is shown in Fig. 3. In addition to poor chemical stability, germanium oxide capping results in a

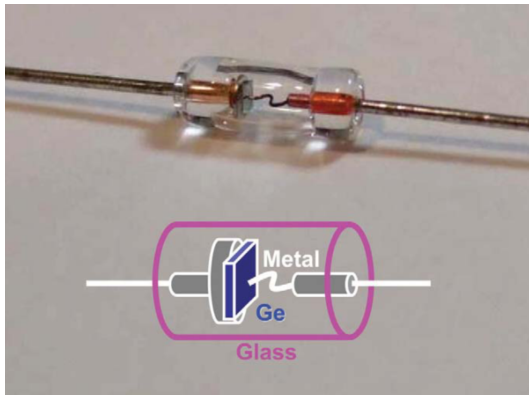

Figure 3: Point contact Ge diode (1S32, Toshiba), 1970s.

high density of electrically active centers at the interface. Carrier trapping and Coulomb scattering by these defects is particularly detrimental for mobility and the exceptional properties of electronic transport observed in bulk Ge are not retained at the surface. Interface traps in Si are effectively suppressed by hydrogen and the device fabrication process routinely includes a Forming Gas Anneal (FGA, a mixture of N_2 and H_2).
But, in Ge the FGA is not successful. Fortunately, the story is not over. Moore's law scaling pace already pushed for the replacement of SiO_2 as insulating material in the mainstream Si technology. Alternative oxides have been studied extensively in the recent years to ensure high electric insulation while shrinking the thickness of the insulator in the constant field scaling framework. The two contrasting requirements are met by employing materials with a high dielectric permittivity (indicated conventionally by κ) to ensure an efficient capacitive coupling between the channel and the gate electrode with comparatively large thickness t ($C \sim \kappa/t$). These high-κ materials can bring the stability and the robustness to the insulating layer in Ge devices, but the minimization of interface defects either by intrinsic interface quality or by post deposition passivation remains an open question. It is apparent that deeper investigations at a fundamental level

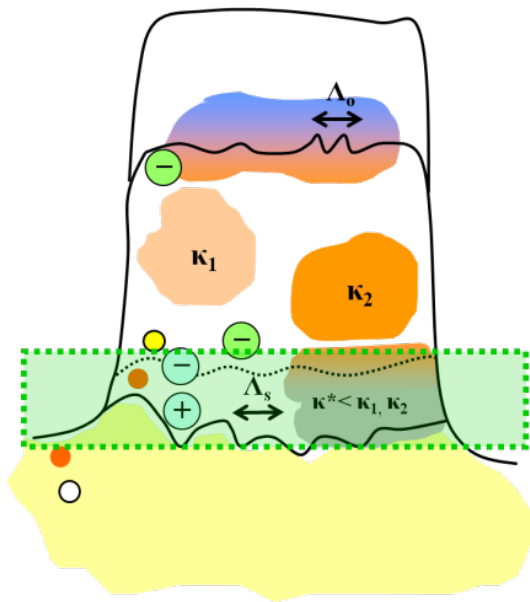

Figure 4: Pictorial representation of the issues in high-κ integration on high mobility substrates. From top: interface roughness, intermixing and fixed charges in the gate oxide stack, structural or chemical inhomogeneity within the oxide resulting in differences in dielectric constant, fixed charges in the interface layer, carrier trapping, roughness at the semiconductor interface. After Molle et al. (2010).

are required to improve the knowledge on the physical properties of the interface defects occurring at Ge interfaces.

Goal of the Thesis

Starting from the recent success in the identification of electrically active defects in several examples of germanium – oxides interfaces by Electrically Detected Magnetic Resonance (EDMR) spectroscopy (Baldovino et al., 2008, 2010), and supported by a long list of achievements obtained by this technique in the study of silicon – oxides interfaces (Fanciulli et al., 2005), the thesis aims at the investigation of the fundamental properties of the defects located at the interfaces between germanium and oxides of technological interest. It must be stressed that the main goal of the present work is not interface optimization (although many outcomes here reached can be exploited in this respect), but rather the gain of a deeper knowledge on the defect structure and the interaction of the electrically active traps with carriers and passivating agents.

In this respect, EDMR spectroscopy has unique advantages as it brings together the investigation of structural properties inherited from Electron Paramagnetic Resonance (EPR), and the sensitivity of electrical techniques. Still, EDMR lacks the ability to characterize the defect in terms of energetic positioning within the bandgap and the technique is complemented by admittance spectroscopy measurements on Metal Oxide Semiconductor capacitors.

Structure of the Thesis

Chapter 1 is a condensed presentation of the theory at the basis of the admittance spectroscopy and electron spin resonance, and the theoretical foundations of the interpretation of the experimental outcomes. Additional details on the experimental techniques and on

sample preparation are given in chapter 2. Chapter 3 briefly resumes the latest experimental evidences and the general knowledge on the interface defects occurring at the (001) oriented germanium – oxides interfaces, as it was at the beginning of the thesis. Then the new results of EDMR measurements on (111) oriented substrates and the first interpretation are discussed, in view of the subsequent investigations with purely electrical techniques. An extensive account of the experimental outcomes yielded by admittance spectroscopy on the different samples is given in chapter 4. Finally, a comprehensive discussion of the overall amount of experimental results is provided in chapter 5. Closing remarks and future perspective are outlined in chapter 6.

Bibliography

Solomon Assefa, Fengnian Xia, and Yurii A Vlasov. Reinventing germanium avalanche photodetector for nanophotonic on-chip optical interconnects. *Nature*, 464(7285):80–4, March 2010. ISSN 1476-4687. doi: 10.1038/nature08813. URL http://www.ncbi.nlm.nih.gov/pubmed/20203606.

Silvia Baldovino, Alessandro Molle, and Marco Fanciulli. Evidence of dangling bond electrical activity at the Ge/oxide interface. *Applied Physics Letters*, 93(24):242105, 2008. ISSN 00036951. doi: 10.1063/1.3050451. URL http://link.aip.org/link/APPLAB/v93/i24/p242105/s1&Agg=doi.

Silvia Baldovino, Alessandro Molle, and Marco Fanciulli. Influence of the oxidizing species on the Ge dangling bonds at the (100)Ge/GeO2 interface. *Applied Physics Letters*, 96 (22):222110, 2010. ISSN 00036951. doi: 10.1063/1.3446839. URL http://link.aip.org/link/APPLAB/v96/i22/p222110/s1&Agg=doi.

R.H. Dennard, F.H. Gaensslen, V.L. Rideout, E. Bassous, and A.R. LeBlanc. Design of ion-implanted MOSFET's with very small physical dimensions. *IEEE Journal of Solid-State Circuits*, 9(5):256–268, October 1974. ISSN 0018-9200. doi: 10.1109/JSSC.1974.1050511. URL http://ieeexplore.ieee.org/lpdocs/epic03/wrapper.htm?arnumber=1050511.

Marco Fanciulli, Omar Costa, Simone Cocco, Gabriele Seguini, Enrico Prati, and Giovanna Scarel. Defects in High-κ Gate Dielectric Stacks. In *NATO Advanced Studies Institute, Series II: Mathematics, Physics and Chemistry*, page 26. Plenum, New York, 2005.

ITRS. More than moore white paper by the irc, 2009. URL http://www.itrs.net/papers.html.

A. Jain, J.-C. Rojas-Sanchez, M. Cubukcu, J. Peiro, J. Le Breton, E. Prestat, C. Vergnaud, L. Louahadj, C. Portemont, C. Ducruet, V. Baltz, A. Barski, P. Bayle-Guillemaud, L. Vila, J.-P. Attané, E. Augendre, G. Desfonds, S. Gambarelli, H. Jaffrès, J.-M. George, and M. Jamet. Crossover from Spin Accumulation into Interface States to Spin Injection in the Germanium Conduction Band. *Physical Review Letters*, 109(10):106603, September 2012. ISSN 0031-9007. doi: 10.1103/PhysRevLett.109.106603. URL http://link.aps.org/doi/10.1103/PhysRevLett.109.106603.

John Kouvetakis and Andrew V. G. Chizmeshya. New classes of Si-based photonic materials and device architectures via designer molecular routes. *Journal of Materials Chemistry*, 17(17):1649, 2007. ISSN 0959-9428. doi: 10.1039/b618416b. URL http://xlink.rsc.org/?DOI=b618416b.

Alessandro Molle, Silvia Baldovino, Sabina Spiga, and Marco Fanciulli. High permittivity materials for oxide gate stack in Ge-based metal oxide semiconductor capacitors. *Thin Solid Films*, 518(6):S96–S103, January 2010. ISSN 00406090. doi: 10.1016/j.tsf.2009.10.065. URL http://www.sciencedirect.com/science/article/pii/S0040609009017088.

Gordon. E. Moore. Cramming more components onto integrated circuits. *Electronics*, 38: 8, 1965. Reproduced in Proc. IEEE, 86, 82 (1998).

Ravi Pillarisetty. Academic and Industry Research Progress in Germanium Nanodevices. *Nature*, 479(7373):324–8, November 2011. ISSN 1476-4687. doi: 10.1038/nature10678. URL http://www.ncbi.nlm.nih.gov/pubmed/22094692.

S Thompson and S Parthasarathy. Moore's law: the future of Si microelectronics. *Materials Today*, 9(6):20–25, June 2006. ISSN 13697021. doi: 10.1016/S1369-7021(06)71539-5. URL http://www.sciencedirect.com/science/article/pii/S1369702106715395.

Jie Xiang, Wei Lu, Yongjie Hu, Yue Wu, Hao Yan, and Charles M Lieber. Ge/Si nanowire heterostructures as high-performance field-effect transistors. *Nature*, 441(7092):489–93, May 2006. ISSN 1476-4687. doi: 10.1038/nature04796. URL http://www.ncbi.nlm.nih.gov/pubmed/16724062.

Table of Contents

Introduction i
Context . . . i
Goal of the Thesis . . . iv
Structure of the Thesis . . . iv
Bibliography . . . vi

Table of Contents viii

1 Foundations 1
1.1 Semiconductor Physics . . . 1
1.2 Metal-Oxide-Semiconductor Capacitor . . . 10
1.3 Electron Paramagnetic Resonance . . . 18
1.4 Spin Dependent Recombination . . . 27
1.5 Bibliography . . . 30

2 Experimental Methods 33
2.1 Sample Fabrication and Preliminary Characterization . . . 33
2.2 Electrically Detected Magnetic Resonance . . . 36
2.3 Interface Trap Characterization by Admittance Spectroscopy . . . 41
2.4 Bibliography . . . 49

3 Electron Spin Resonance Spectroscopy 51
3.1 (001)Ge/GeO_2 . . . 51
3.2 (111)Ge/GeO_2 . . . 56
3.3 Toward Electrical Characterization: Ge/GeO_2/Al_2O_3 . . . 59
3.4 Bibliography . . . 63

4 Admittance Spectroscopy 65
4.1 *p*-type (001)Ge/GeO_2/Al_2O_3 . . . 65
4.2 *p*-type (111)Ge/GeO_2 . . . 79
4.3 *n*-type (001)Ge/GeO_2 . . . 86
4.4 *n*-type (111)Ge/GeO_2 . . . 88
4.5 Comparative Analysis . . . 90
4.6 Bibliography . . . 91

5 Discussion on the Nature of the Ge Interface Centers 93

5.1 Defects at the Silicon Interface 93
5.2 Experimental Observations at the Germanium Interface 98
5.3 The Negative-$\mathcal{U}$ Model for Interface Defects 103
5.4 Bibliography 109

6 Conclusions and Outlook 116
6.1 Bibliography 119

Acknowledgments 121

1 Foundations

And God said

$$\nabla \cdot \mathbf{D} = \rho$$
$$\nabla \cdot \mathbf{B} = 0$$
$$\nabla \times \mathbf{E} = -\frac{\partial \mathbf{B}}{\partial t}$$
$$\nabla \times \mathbf{B} = \mu_0 \left(\mathbf{J} + \epsilon_0 \frac{\partial \mathbf{E}}{\partial t} \right)$$

and there was light

Brent Meeker

In this chapter the relevant semiconductor physics is introduced, in order to establish a common ground of definitions and conventions for the development of the thesis.

1.1 Semiconductor Physics

The most important concept to understand semiconductor materials and devices is the presence of electron energy levels grouped into bands separated by a forbidden energy region called *energy gap* (or bandgap). The two bands that play a role in electrical conduction are referred to as *valence band* (VB), mostly filled lower band, and *conduction band* (CB), almost empty higher lying band. A clever trick to simplify the mathematical treatment is to consider the VB as mostly empty of holes. These new entities represent the lack of electrons. Electronic transport properties depend on the free carrier concentration in the two bands. Temperature, doping, and illumination, all affect transport properties. The interface, which is of course unavoidable in real life, introduces a wealth of additional phenomena and interesting physics.

Energy bands

From the point of view of quantum mechanics electrons in a semiconductor can be regarded as travelling waves and the interaction with the ion cores of the lattice leads to constructive and destructive interference leading to the creation of an energy gap between the top of the VB and the bottom of the CB as anticipated above. The relationship between energy E and wave-vector k of the carriers is called *band structure*. In the specific case

of Germanium, shown in Fig. 1.1, the VB maximum E_V is at the Γ point (0,0,0) of the reciprocal space, while the CB minimum E_C occurs at the L point (1,1,1). Due to this peculiar configuration, Ge is a so-called indirect gap semiconductor. The VB maximum is formed by an upper four-fold degenerate level, and a lower two-fold degenerate level. Away from Γ, the upper band splits into two-fold degenerate bands, denominated *light-* and *heavy-holes* band. The lower band is called *split-off* band and it is separated from the upper bands by the spin-orbit interaction. With reference to the CB, the position of the minimum at the L point implies that there are four distinct wave-vectors[1] describing the states at energy E_C. Fig. 1.2 reveals that, in close proximity of the L points, the iso-energy surfaces in the band structure outline four regions, termed *valleys*.
Usually, electrons occupy the lower part of the CB and in the same way holes are found only close to the VB maximum. Near the band edges the band structure can be approximated by a quadratic equation (Sze and Ng, 2006; Schroder, 2006; Nicollian and Brews, 2003):

$$E(k_i) = \frac{\hbar^2 k_j^2}{2m_{i,j}^*} \qquad ; \qquad \frac{1}{m_{i,j}^*} \equiv \frac{1}{\hbar^2}\frac{\partial^2 E}{\partial k_i \partial k_j} \tag{1.1}$$

The quantity $m_{i,j}^*$ is termed *effective mass*.

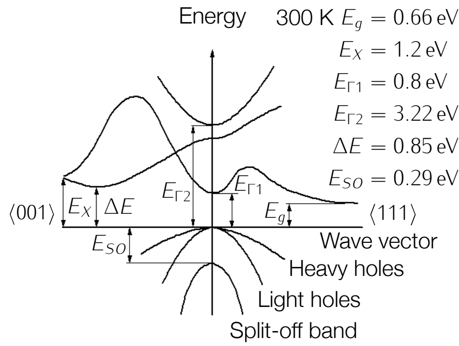

Figure 1.1: Band structure of Ge.

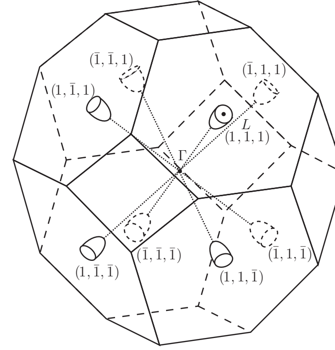

Figure 1.2: Valleys in Ge CB. Constant energy surfaces, approximated by ellipsoids, are shown about the CB minima.

Under these conditions the density of quantum states per unit volume per unit energy can be written as

$$M_C(E) = G_C \frac{\sqrt{2}}{\pi^2}\frac{m_{de}^{3/2}}{\hbar^3}(E - E_C)^{1/2} \tag{1.2}$$

considering a number G_C of equivalent minima in the CB, and

$$M_V(E) = \frac{\sqrt{2}}{\pi^2}\frac{m_{dh}^{3/2}}{\hbar^3}(E_V - E)^{1/2} \tag{1.3}$$

in the VB. m_{de} and m_{dh} are the appropriate density-of-state effective masses.

[1] as the minima occur exactly at the Brillouin zone boundary, they are shared by two Brillouin zones. In other words, in the reduced zone scheme the eight points of the reciprocal lattice $(1,1,1),(\bar{1},\bar{1},\bar{1})$; $(1,1,\bar{1}),(\bar{1},\bar{1},1)$; $(1,\bar{1},1),(\bar{1},1,\bar{1})$; $(\bar{1},1,1),(1,\bar{1},\bar{1})$ can be considered as pairs defining just four distinct points.

Ideally at 0 K the VB is completely full and the CB is empty, no carrier flow is possible even when an electric field is applied. However, at finite temperatures a number of electron-hole pairs are present due to thermal excitation. At the thermodynamical equilibrium, the distribution of the carriers among the bands is given by the Fermi-Dirac distribution (Born et al., 1989). This state is characterized by an invariance in time of the measurable macroscopic quantities that describe the isolated system, such as temperature, volume, potential, and charge. In thermodynamics, the equilibrium state minimizes the free energy of the system, or maximizes the randomness in the distribution of the particles in the language of statistical mechanics. Mathematically, the Fermi-Dirac distribution function f_n is the probability that an energy level E is occupied by an electron and can be written in the form

$$f_n(E-\mu) = \frac{1}{1+\exp\left(\frac{E-\mu}{k_B T}\right)} \tag{1.4}$$

where $k_B = 8.61733 \cdot 10^{-5}\,\text{eV/K}$ is the Boltzmann's constant and μ is the chemical potential, often referred to as the *quasi-Fermi level q.f.l.*. For $T = 0\,\text{K}$, the chemical potential coincides with the Fermi level E_F, the energy at which a state has a probability 1/2 of being occupied. When no electric field is applied, the thermodynamical equilibrium condition implies a constant μ throughout the sample volume.
The probability that a level E is vacant (or equivalently, that it is occupied by a hole), is $f_p = 1 - f_n$([2])

$$f_p(\mu-E) = \frac{1}{1+\exp\left(\frac{\mu-E}{k_B T}\right)} \tag{1.5}$$

When the chemical potential is many $k_B T$ far from either the band edges, the Fermi-Dirac distribution is adequately approximated by the Maxwell-Boltzmann distribution and the system is said to be *nondegenerate*.

The total density of electrons in the CB is given by

$$n = \int_{E_C}^{\infty} M_C(E) f_n(E-\mu)\mathrm{d}E \tag{1.6}$$

and similarly for holes in the VB

$$p = \int_{\infty}^{E_V} M_V(E) f_p(\mu-E)\mathrm{d}E \tag{1.7}$$

In the nondegenerate case and in the parabolic band approximation of Eq. 1.1, n and p read

$$n = M_C^* \exp\left(-\frac{E_C-\mu}{k_B T}\right) \qquad p = M_V^* \exp\left(-\frac{\mu-E_V}{k_B T}\right) \tag{1.8}$$

[2]the subscripts n and p are taken from the names of n- and p-type used to indicate the two types of doping of the semiconductors, with the first having electrons prevailing and holes the second. The names have been coined when it was observed that if a metal whisker was pressed against a p-type material, forming a Schottky barrier diode, a *positive* bias was required on the semiconductor to produce a noticeable current. Conversely a *negative* bias was required on an n-type material to produce a large current (Riordan and Hoddeson, 1997).

where $M_C^* = G_C 2/\hbar^3 (m_{de} k_B T/\pi)^{3/2}$ and $M_V^* = 2/\hbar^3 (m_{dh} k_B T/\pi)^{3/2}$. From a carrier density standpoint, the CB and VB can be regarded as two single levels of effective density M_C^* and M_V^* located at E_C and E_V, respectively. In the case of Ge, the effective density of states is $M_C^* = 1.98 \cdot 10^{15} T^{3/2}$ (cm^{-3}) in the CB and $M_V^* = 9.6 \cdot 10^{14} T^{3/2}$ (cm^{-3}) in the VB.

The position of the chemical potential can be calculated by requiring charge neutrality $n = p$ in intrinsic semiconductor:

$$\mu = \frac{E_C + E_V}{2} + \frac{k_B T}{2} \log \frac{M_V^*}{M_C^*} \equiv E_i \tag{1.9}$$

$E_i \approx E_g/2$ is often referred to as the intrinsic quasi-Fermi level. The intrinsic carrier concentration, $n_i = \sqrt{pn}$ in intrinsic material, can be written as

$$n_i = \sqrt{M_C^* M_V^*} \exp\left(-\frac{E_g}{2k_B T}\right) \tag{1.10}$$

The relation above shows that the so called *pn product* $pn = n_i^2$ is independent of μ and independent of individual values of p and n[3]. Eq. 1.10 allows to rewrite the carrier density in the bands as

$$n = n_i \exp\left(\frac{\mu - E_i}{k_B T}\right) \qquad p = n_i \exp\left(\frac{E_i - \mu}{k_B T}\right) \tag{1.11}$$

The energy gap E_g of semiconductors is a function of the temperature T and can be expressed by a universal function known as Varshni's law (Varshni, 1967):

$$E_g = E_0 - \frac{\alpha T^2}{T - \beta} \tag{1.12}$$

In the case of Ge best values of the parameters are $E_0 = 0.742$ eV, $\alpha = 4.8 \cdot 10^{-4}$ eV/K, and $\beta = 235$ K. The energy gap is also a function of the pressure.

When impurities are introduced inside a semiconductor, additional energy levels are introduced. These levels usually lie inside the gap and the impurities are termed *donors* if are neutral when the level is filled by an electron and positive if empty. Impurities are termed *acceptors* if are neutral when the level is empty and negative if filled by an electron. The position of the energy level determines the fraction of dopants being ionized. The energy separation from the band of the most common dopants in Ge are shown in Tab. 1.1. Since these ionization energies are small compared to thermal energy $k_B T$, shallow dopants can be considered completely ionized at room temperature.

The energy-distribution function in the case of doped semiconductors can be derived using the maximum probability method, following the elegant approach of Look (1981)[4]. Electrons in the band states or in atomic impurity states are considered as particles in separate "boxes" and, provided that electrons in different boxes interact only weakly with each other, the problem is reduced to finding the number of distinguishable ways that a

[3] the relation is of general validity, also in doped semiconductors, and it is an expression of the mass-action law.

[4] this method can also be used to derive the Fermi-Dirac distribution function for the carriers in the bands.

donor	As	P	Sb	Bi
E_D (eV)	0.014	0.013	0.010	0.013

acceptor	Al	B	Ga	In
E_A (eV)	0.011	0.011	0.011	0.012

Table 1.1: Ionization energies of shallow donors and acceptors in Ge. Energies are in eV

given number of particles can be distributed among a given number of boxes. According to the maximum probability principle, the particles will distribute themselves among the boxes so as to allow the maximum number of combinations, consistent with macroscopic requirements. In other words, the electrons will distribute among the possible energy levels in such a way that as much eigenstates as possible can be written for the whole system, consistent with a given total energy[5].

In the case of impurity atoms with levels in the energy gap, a box represents an s state which can hold both spin-up and spin-down electrons. The total number of distinguishable ways W that electrons can be arranged among N impurities per unit volume is given by

$$W = \frac{2^{n_1} N!}{n_0! n_1! n_2!} \tag{1.13}$$

where n_0, n_1, and n_2 is the density of impurities with 0, 1, and 2 electrons respectively. For single electron occupation of the level, there are two distinguishable states due to the spin degree of freedom giving the factor 2^{n_1}. The constraints imposed by the macroscopic requirements are

$$\begin{aligned} n_0 + n_1 + n_2 &= N && \text{total number of impurities per unit volume} \\ n_1 + 2n_2 + n &= n_t && \text{total number of electrons per unit volume} \\ E_1 n_1 + E_2 n_2 + E_C n &= E_t && \text{total energy} \end{aligned} \tag{1.14}$$

E_1 and E_2 are the energy levels of the singly occupied and doubly occupied state, respectively. The term *level* describes part of the energy difference between two states of the system comprising the "box" and the reservoir. The energy change in the transition is given by $E_l - \mu$, where μ is the energy per particle of the reservoir called *chemical potential*. Usually, $E_2 > 2E_1$ because of Coulomb repulsion[6]. E_0 is presumed to be degenerate with the VB and is taken as the zero point. In order to find the set of n_k

[5] by assuming only weak interactions among electrons in different boxes, the eigenstates for the whole system can be written as the properly symmetrized product of the individual eigenstates.

[6] the converse is true for *negative-$\mathcal{U}$ centers*

which maximizes W, the Lagrange multipliers method is employed, obtaining

$$\begin{aligned} n_0 =& \frac{N}{1 + 2\exp\left(\frac{-E_1+\mu}{k_B T}\right) + \exp\left(\frac{-E_2+2\mu}{k_B T}\right)} \\ n_1 =& \frac{N}{1 + \frac{1}{2}\exp\left(\frac{E_1-\mu}{k_B T}\right) + \frac{1}{2}\exp\left(\frac{E_1-E_2+2\mu}{k_B T}\right)} \\ n_2 =& \frac{N}{1 + \exp\left(\frac{E_2-2\mu}{k_B T}\right) + 2\exp\left(\frac{E_2-E_1-\mu}{k_B T}\right)} \end{aligned} \tag{1.15}$$

where the Lagrange multipliers have been identified with the chemical potential μ and the thermal energy $k_B T$. From the strong repulsive Coulomb interaction between two electrons on the same atom, $E_2 \gg E_1$ is expected, giving

$$n_1 \approx \frac{N}{1 + \frac{1}{2}\exp\left(\frac{E_1-\mu}{k_B T}\right)} \tag{1.16}$$

In the following, the number of electrons bound to donors n_1 will be denoted by n_D for consistency with the majority of the literature. In the same way, N will be replaced by N_D and E_1 by E_D:

$$n_D = \frac{N_D}{1 + \frac{1}{2}\exp\left(\frac{E_D-\mu}{k_B T}\right)} \tag{1.17}$$

Repeating the derivation in the case of acceptors, the density of holes bound to acceptors p_A is given by

$$p_A = \frac{N_A}{1 + 2\exp\left(\frac{\mu-E_A}{k_B T}\right)} \tag{1.18}$$

The position of the chemical potential can be found again from the condition of charge neutrality. Writing the density of negative charges on the left side and the density of positive charges on the right, results

$$n + N_A - p_A = p + p_A + N_D \tag{1.19}$$

Normally the dopant levels are shallow and in most applications, when $T > 30\,\mathrm{K}$ for Ge, they can be considered fully ionized so that $n_D = p_A = 0$. Recalling the equilibrium condition $pn = n_i^2$ it is possible to write

$$\begin{aligned} \mu =& E_i + k_B T \log\frac{N_D}{n_i} \qquad && n\text{-type} \\ \mu =& E_i - k_B T \log\frac{N_A}{n_i} \qquad && p\text{-type} \end{aligned} \tag{1.20}$$

assuming that $N_D \gg N_A$ in n-type and $N_A \gg N_D$ in p-type semiconductor. The trend of the chemical potential positioning in Ge, varying temperature and donor or acceptor concentration, is shown in Fig. 1.3.

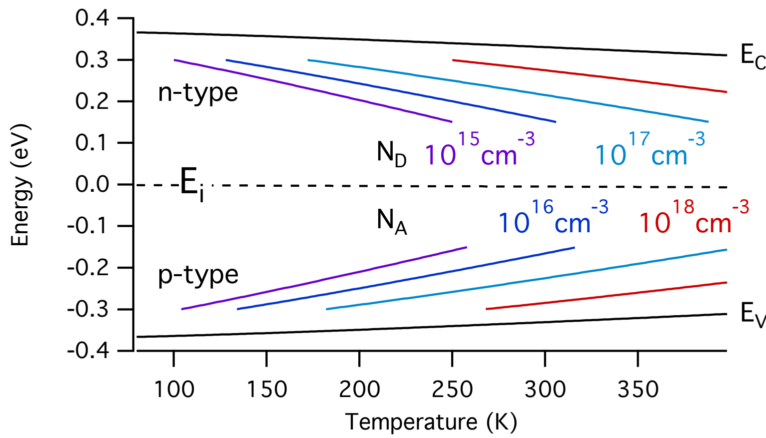

Figure 1.3: Chemical potential as a function of temperature with impurity concentration as parameter for germanium. Curves in color are calculated for selected doping concentration using Eq. 1.20. Intrinsic energy level E_i is calculated from Eq. 1.9. The variation of Ge bandgap with temperature, also included, is calculated from Eq. 1.12.

Electronic transport properties

An electron excited into the CB is free to move around the crystal under the influence of thermal agitation. In the same way, thanks to the deficiency created in the VB, electrons are free to rearrange and the positive charge left in the band – the hole – moves subjected to the same thermal agitation. The velocity associated with thermal motion, called *thermal velocity*, can be expressed by

$$\sqrt{\frac{3k_BT}{m^*}} \tag{1.21}$$

Carriers can thus alter their momentum interacting with the lattice, through different mechanisms (Gold and Dolgopolov, 1986) such as phonon scattering, Coulomb scattering (Stern and Howard, 1967), and surface roughness scattering (Matsumoto, 1974). If an electric field $\mathcal{E}$ is applied, then carriers are accelerated between collisions. Defining the momentum relaxation time τ_k as the effective time for a carrier to lose memory of the previous momentum state, the drift velocity v_d is given by

$$v_d = \frac{Q\tau_k}{m^*}\mathcal{E} \tag{1.22}$$

where m^* is the effective mass and Q is the charge of the particle, namely $Q = -q = -1.6022 \cdot 10^{-19}\,\mathrm{C}$ in the case of electrons and $Q = q$ in the case of holes. Electron mobilities μ_e and μ_h can be defined for electrons and holes respectively

$$\mu_{e,h} \equiv \frac{\pm q\tau_k}{m^*_{e,h}} \tag{1.23}$$

Eq. 1.22 can be rewritten in a simplified form as $v_{e,h} = \pm\mu_{e,h}\mathcal{E}$. Drift current densities $J^{\mathrm{drift}}_{e,h}$ are defined accordingly:

$$J^{\mathrm{drift}} = J^{\mathrm{drift}}_e + J^{\mathrm{drift}}_h = q(\mu_e n + \mu_h p)\mathcal{E} \tag{1.24}$$

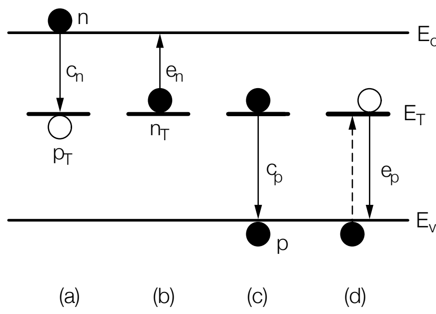

Figure 1.4: The basic processes involved in recombination by trapping: (a) electron capture, (b) electron emission, (c) hole capture, (d) hole emission. The energy level of the trap is indicated by E_T. Generation, recombination and trapping are described in the text.

By defining the conductivity $\sigma \equiv q(\mu_e n + \mu_h p)$ and the resistivity $\rho = \sigma^{-1}$, it is possible to write

$$J^{\text{drift}} = \sigma \mathcal{E} = \frac{\mathcal{E}}{\rho} \tag{1.25}$$

(Ohm's law).

Trapping centers

In the previous part of this chapter, shallow centers have been described. Being either donor or acceptors, the main effect on the semiconductor is to provide carriers, altering the position of the chemical potential, and promote conduction. Another class of centers is represented by *deep level impurities*, introducing stronger perturbation in the periodic crystal potential resulting in localized levels at lower depth inside the energy gap. In the bulk, metallic impurities or crystal imperfections such as dislocations, stacking faults, vacancies, interstitials, or precipitates are usually deep level centers. They mediate carrier recombination and generation, for this reason such defects are often called generation-recombination ($G-R$) centers or traps. The mathematical description of these processes has been put forward by Shockley, Read and Hall (Shockley and Jr, 1952; Hall, 1952).
Fig. 1.4 shows the steps involved in hole and electron recombination and generation at a center with energy level E_T inside the gap. The process shown in (a) is an electron capture event, characterized by the capture coefficient c_n. Rigorously speaking, $c_n(E)$ depends on the electron energy. For an electron possessing an energy in the range dE, with thermal velocity v_{th}, and a trap characterized by a capture cross section σ_n, the capture coefficient is the average of the product $v_{th} \times \sigma_n$ over the states of energy $[E, E + \mathrm{d}E]$:

$$c_n(E) = \langle \sigma_n v_{th} \rangle_E \tag{1.26}$$

After the electron capture, the center can either emit the electron back to the CB, as shown in (b), within an emission time e_n, or capture a hole from the VB, as shown in (d). The last event is characterized by the capture coefficient c_p. Similarly to Eq. 1.26, $c_p(E) = \left\langle \sigma_p v_{th} \right\rangle_E$ holds. Alternatively, when the center is occupied by a hole it can emit the hole back to the VB, as shown in (c), within a time constant e_p. A *generation* event is process (b) followed by process (d), while a *recombination* event is process (a) followed by process (c). When (a) is followed by (b) or (c) is followed by (d), the carrier is captured and subsequently emitted to the same band, and this event is called trapping (this is the reason that the centers are also called *traps*).

The physical effects accounted for in the model by Shockley, Read and Hall arise from the statistics of the events described in Fig. 1.4, with the rate of these processes assumed to be limited by the availability of electrons and holes for the capture. Other possible limiting factor are neglected, such as the time of readjustment of the electron in the trap after the capture (de-excitation).
The mathematical description of the statistics governing the processes is contained in Eq. 1.15. In the limit $E_2 \gg E_1$, which applies to many conventional deep traps, it is convenient to denote the density of singly occupied traps n_1 as n_T. Similarly, the density of unoccupied traps n_0 is denoted by p_T[7]. If the system is in thermal equilibrium, the chemical potential of the traps and the chemical potential of the carriers coincide. For this case the principle of detailed balance[8] requires that the rate of capture and emission must be equal and the coefficients of capture and emission involving an electronic level E satisfy the relation[9]

$$e_n = c_n \exp\left(\frac{E_T - E}{k_B T}\right) \qquad e_p = c_p \exp\left(\frac{E - E_T}{k_B T}\right) \tag{1.27}$$

In the case of nondegenerate semiconductors, it is possible to integrate on CB electron states (VB states for holes), to obtain an average value of $\langle c_n \rangle$ ($\langle c_p \rangle$) over the distribution $f_{p,n}$ (Eq. 1.4 and 1.5):

$$\langle c_n \rangle = \int_{E_C}^{\infty} f_n(E_C - E) c_n M_C^*(E) \mathrm{d}E \qquad \langle c_p \rangle = \int_{\infty}^{E_C} f_p(E - E_V) c_p M_V^*(E) \mathrm{d}E \tag{1.28}$$

To keep a clean notation, capture coefficients are referred simply as $c_{n,p}$ and the conduction or valence bands can be considered as individual levels of energy $E_{C,V}$.

The appropriate *rate equations* describing the dynamics of the traps can be written in terms of the fundamental processes depicted in Fig. 1.4:

$$\begin{aligned}
\frac{\mathrm{d}n}{\mathrm{d}t} &= e_n n_T - c_n n p_T && \text{electron rate of change} \\
\frac{\mathrm{d}p}{\mathrm{d}t} &= e_p p_T - c_p p n_T && \text{hole rate of change} \\
\frac{\mathrm{d}n_T}{\mathrm{d}t} &= \frac{\mathrm{d}p}{\mathrm{d}t} - \frac{\mathrm{d}n}{\mathrm{d}t} && \text{trap occupancy rate of change}
\end{aligned} \tag{1.29}$$

Under steady state, the time derivatives vanish yielding

$$e_n n_T = c_n n p_T \qquad e_p p_T = c_p p n_T \tag{1.30}$$

The emission time constant is defined as $\tau_{n,p} \equiv 1/e_{n,p}$ and combining Eq. 1.30, 1.11 gives[10]:

$$\tau_n = \frac{1}{\sigma_n v_{th} M_C^*} \exp\left(\frac{E_C - E_T}{k_B T}\right) \qquad \tau_p = \frac{1}{\sigma_n v_{th} M_V^*} \exp\left(\frac{E_T - E_V}{k_B T}\right) \tag{1.31}$$

[7] traps not occupied by an electron can be seen as occupied by a hole. Moreover, as Coulomb repulsion prevents double occupation, $n_2 = 0$ and $p_T = N - n_T$.

[8] the principle of detailed balance states that under equilibrium conditions each fundamental process and its inverse must balance, independently of any other process that may be occurring.

[9] rigorously, using Eq. 1.15 gives $e_n = 1/2 c_n \exp(E_T - E)/k_B T$, but the factor 1/2 can be incorporated into the coefficient c_n.

[10] see footnote 9.

1.2 Metal-Oxide-Semiconductor Capacitor

The previous section of this chapter introduced the main concepts and the essential mathematical description of bulk semiconductor physics. This section covers the interfaces between semiconductor and insulators that can be found in ideal and real devices. The study of interfaces opens a richer playground, as attested by the development of the very sensitive semiconductor characterization techniques it has enabled. In turn, elaborate theoretical models have evolved from the deepened insight allowing further improvement in the characterization, in a positive-feedback chain. The Metal-Oxide-Semiconductor (MOS) system is the simplest and most important test structure, since the emergence of integrate circuits based on MOS Field Effect Transistors (MOSFETs). It was originally proposed as a voltage-dependent varistor (a variable capacitor) in 1959, by Moll (1959) and by Pfann and Garrett (1959).
After the description of MOS structure and principles of operation, specific consideration is given to the role of interface defects on device characteristics.

Structure and operation

A simple form of MOS device is shown in Fig. 1.5 (a). It consists in a metal layer (also called gate) in contact with an insulator (typically an oxide) on top of a semiconductor. Voltage can be applied on the top gate and it is defined as positive when the metal plate

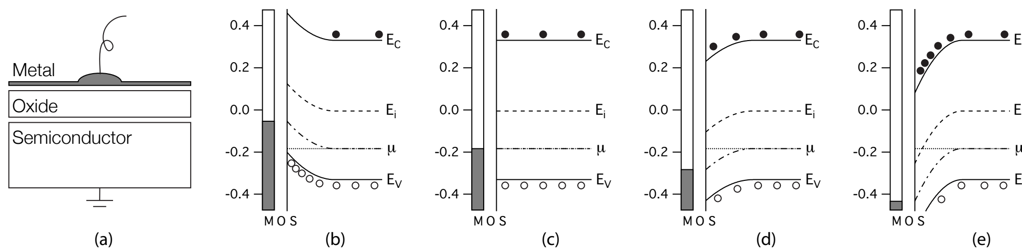

Figure 1.5: (a) MOS structure, in its simplest form. (b) Energy-band diagram of ideal p-type MOS at accumulation, (c) flatband, (d) depletion, and (e) inversion condition.

is positively biased with respect to the semiconductor body.
The equilibrium condition stated in the previous section (μ = const.) has to be restated for the MOS structure, where systems with different allowed energy levels are brought into contact. Besides requiring zero net transfer of particles, no energy should be gained by the transfer to satisfy energy balance. Dealing with charged particles, the electrons, transfer results in charging of the material, that acquire a potential ψ. The equilibrium condition when two materials are brought into contact can thus be written as

$$\mu_1 - q\psi_1 = \mu_2 - q\psi_2 \tag{1.32}$$

The quantity $\mu - q\psi$ is called *electrochemical potential*.

In an ideal MOS capacitor charges can exist only in the semiconductor and on the metal gate, with opposite sign and same magnitude. Additionally, the ideal insulator prevents carrier transport between gate and semiconductor. Thus, excluding short time

transients due to the charging and discharging of the capacitor, the bias induces only an electric field in the active region close to the insulator. A p-type semiconductor substrate is considered in the following. By placing a negative charge at the gate, holes in the semiconductor are attracted to the interface, as shown in Fig. 1.5 (b), and the MOS capacitor is said to be in *accumulation* regime. Removing the negative charges from the gate, holes flow away from the interface and at a gate bias denominated *flatband voltage* V_{FB}, Fig. 1.5 (c), the semiconductor is neutral everywhere. For gate bias positive with respect to flatband, holes are repelled from the interface and the positive charge at the gate is balanced by the negative acceptor ions left close to the surface. This is the *depletion* regime, shown in Fig. 1.5 (d). If the positive bias is increased further, an electron layer must form at the interface to keep the *pn* product constant. Fig. 1.5 (e) shows the MOS capacitor in *inversion* condition, when $n > p$ at the interface.

The mathematical description corresponding to the picture above is obtained considering Eq. 1.6, 1.7 and the Poisson equation

$$\nabla^2\psi = -\frac{\rho}{\epsilon} \tag{1.33}$$

where ρ is the net charge and ϵ is the dielectric constant. The absence of current flow legitimates the use of this limited set of equation, in place of complicated transport equations. The additional assumption that the density of states in CB and VB is not changed by the electric field, denominated *band-bending approximation*, implies that the only effect throughout the semiconductor is a shift of all the energy levels by a constant amount $q\psi(x)$. Eq. 1.6 and 1.7 can then be written in a more convenient form:

$$n(x) = N_D \exp\left(\frac{q\psi(x)}{k_B T}\right) \qquad p(x) = N_A \exp\left(-\frac{q\psi(x)}{k_B T}\right) \tag{1.34}$$

To simplify the notation in the following analysis, a second potential ϕ and the dimensionless quantities u and v are defined:

$$\begin{aligned} q\phi &= \mu - E_i \\ u &= \frac{q\phi}{k_B T} \\ v &= \frac{q\psi}{k_B T} \end{aligned} \tag{1.35}$$

ψ and ϕ are related by the equation $\psi(x) = \phi(x) - \phi_B$, where the subscript B indicate the bulk value. The various potential are indicated on the energy diagram in Fig. 1.6.

Restricting the treatment to the dimension perpendicular to the surface, Poisson equation reads:

$$\frac{d^2\phi}{dx^2} = -\frac{\rho(x)}{\epsilon_s} \tag{1.36}$$

where the dielectric constant of the semiconductor ϵ_s is indicated. The net charge ρ is obtained considering the free electron and hole density, together with ionized donors and acceptors:

$$\rho(x) = q[p(x) - n(x) + N_D - N_A] \tag{1.37}$$

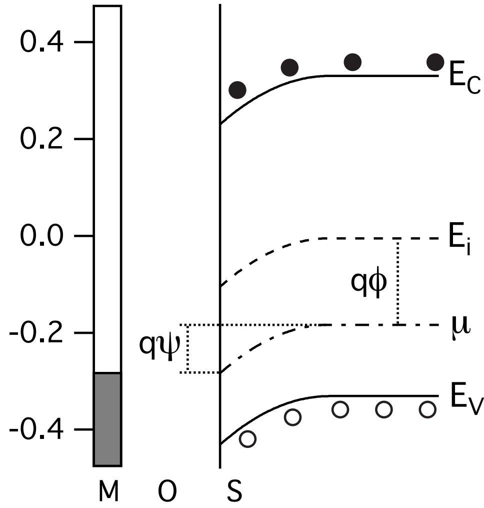

Figure 1.6: Energy diagram of a p-type MOS capacitor, showing the two potentials ψ and ϕ defined in the text.

Combining Eq. 1.34 - 1.36 it is possible to write a dimensionless Poisson equation, valid in the band-bending approximation (Macdonald, 1962)

$$\frac{\mathrm{d}^2 u}{\mathrm{d}x^2} = \frac{\sinh u(x) - \sinh u_B}{\lambda_i^2} \tag{1.38}$$

and the quantity

$$\lambda_i = \sqrt{\frac{\epsilon_s k_B T}{2q^2 n_i}} \tag{1.39}$$

is the intrinsic Debye length. In Ge at room temperature $\lambda_i \approx 0.8\,\mu$m. Eq. 1.38 can be integrated in an ideal MOS to obtain

- the electric field at the semiconductor interface:

$$\begin{aligned} \mathcal{E}_S =& \mathrm{Sgn}(u_B - u_S)\frac{k_B T}{q\lambda_i}\mathcal{F}(u_S, u_B)\,, \text{ where} \\ \mathcal{F}(u_S, u_B) =& \sqrt{2}\sqrt{(u_B - u_S)\sinh u_B - (\cosh u_B - \cosh u_S)}\,, \\ \mathrm{Sgn}(u) =& \frac{u}{|u|} \end{aligned} \tag{1.40}$$

- the surface charge density (from Gauss law):

$$Q_S = \epsilon_s \mathcal{E}_S = \mathrm{Sgn}(u_B - u_S)\frac{\epsilon_s}{\lambda_i}\frac{k_B T}{q}\mathcal{E}(u_S, u_B) \tag{1.41}$$

- the shape of the potential barrier, from the integration of

$$\frac{x}{\lambda_i} = \int_{u_S}^{u} \frac{\mathrm{d}u}{\mathcal{E}(u, u_B)} \tag{1.42}$$

Further simplification are introduced in the equations above by adopting the *depletion approximation*: the charge density in the transition between the space charge region and the neutral gap is approximated by a step function centered at $x = w$. The actual distribution is smoothed on a length scale $\approx \lambda_{n,p} = \lambda_i\sqrt{2n_i/N(w)}$, called extrinsic Debye length. At room temperature, in moderately doped Ge ($N \approx 10^{16}$) $\lambda_{n,p} \approx 50\,\text{nm}$. For comparison, the maximum depletion width in strong inversion calculated with the Lindner criterion (Lindner, 1962) is $w_{\text{max}} \approx \sqrt{2}\lambda_{n,p}\sqrt{2.10u_B + 2.08}$, or $w_{\text{max}} \approx 0.26\,\mu\text{m}$, making the depletion approximation generally acceptable. The shape of the potential barrier, for uniform doping concentration N in depletion approximation, is parabolic in x:

$$\begin{aligned}\psi =&\psi_S\left(1-\frac{x}{w}\right)^2\\ \psi_S =&\frac{1}{2}\frac{q}{\epsilon_s}Nw^2\end{aligned} \tag{1.43}$$

Having drawn the main equations describing charges and potential inside the MOS, it is possible to derive the quantities of interest to the standard electrical characterization: the capacitance C and the conductance G. The static capacitance is defined as $C_{\text{static}} \equiv Q/V_g$, while the *differential capacitance* is defined as $C \equiv \mathrm{d}Q/\mathrm{d}V_g$. Of the two, the differential capacitance assumed more importance because the most sensitive measurements involve small-signal methods. Small-signal conductance is defined as $G = \mathrm{d}Q/\mathrm{d}t \times 1/V$[11]. Capacitance and conductance can be considered the components of a complex quantity called *admittance* $Y = G + \jmath\omega C$. In the following, capacitance and conductance are expressed per unit area.
The capacitance of the MOS structure can be expressed as the series combination of the oxide capacitance C_{ox} and the semiconductor capacitance C_s:

$$C^{-1} = C_{ox}^{-1} + C_s^{-1} \tag{1.44}$$

The surface potential and gate voltage are related to each other by

$$V_g = -V_{ox} - \psi_S = -\frac{Q_s}{C_{ox}} - \psi_S \tag{1.45}$$

An important experimental parameter affecting the MOS response is the frequency of the small signal modulation. In the simplest case, the modulation is sufficiently slow to let the charges (both minority and majority carriers in the semiconductor) follow the potential. Starting from the definition of differential capacitance, Eq. 1.41, and making use of 1.45, it is possible to write[12]

$$\begin{aligned}C_s^{LF} &= -\mathrm{Sgn}(u_B - u_S)\frac{\epsilon_s}{\lambda_i}\frac{\mathrm{d}}{\mathrm{d}u_S}\left[\mathcal{F}(u_S, u_B)\right]\\ &= -\mathrm{Sgn}(u_B - u_S)\frac{\epsilon_s}{\lambda_i}\frac{\sinh u_S - \sinh u_B}{\mathcal{F}(u_S, u_B)}\end{aligned} \tag{1.46}$$

[11] G can be regarded as a complex quantity including the mutual phase between charge variation and voltage stimulus.

[12] provided that ac changes are so slow that equilibrium is maintained, the ac variation $\delta/\delta u_S$ can be found by differentiation.

valid in the *low frequency (LF) regime*. Eq. 1.46, together with Eq. 1.41, 1.44, and 1.45 are a comprehensive description of the ideal MOS capacitor characteristics in the low frequency limit.

In accumulation and depletion, C_s is given by majority carriers rushing in and out from the depletion layer, following the ac variation of the surface potential. The time constant of the majority carriers is of the order of $\epsilon_s/q\mu n$, or $\approx 10^{-9}$ s in the depletion region and $\approx 10^{-12}$ s at the depletion edge. Conventional capacitance measurements rarely exceed MHz frequencies and the response of the majority carriers can be considered instantaneous.
On the other side, minority carriers are responsible for C_s in inversion. The mechanisms for minority response to the surface potential modulation involve generation of carriers at the back contact, diffusion through the semiconductor and drift through the space charge region; generation and recombination in the depletion layer; supply from nearby sources (such as $p-n$ junctions). These processes are considerably slower than majority response. Considering *generation recombination* (GR) on a trap located at midgap, response time is given by

$$\tau_{\text{min}} = \frac{\tau}{\sqrt{2}} \left(\frac{N_A}{n_i} \right) \sqrt{1 - \frac{v_T}{u_B}} \tag{1.47}$$

In Ge at room temperature $\tau_{\text{min}} \approx 10^{-2}$ s, where τ has been estimated $\approx 7 \cdot 10^{-4}$ according to Eq. 1.31 and $v_T = 0$.
The description of inversion capacitance in the *intermediate frequency regime*, when the surface potential variation occurs on the same time scale of minority response, is a difficult task due to the interplay of different mechanisms and the dependency on the detailed sample characteristics, such as the response of bulk traps in the bandgap. On the other hand, a description of MOS capacitance has been developed in the *high frequency (HF) regime*, with a broad range of applicability (Brews, 1974). Even though minority carriers do not respond to high frequency modulation, their dynamics must be taken into account in the calculation of C_s^{HF}. The total number of minority carriers at the semiconductor interface is determined by the average bias level, as in the low frequency regime, but carriers undergo a rearrangement in the inversion layer during the each cycle of the ac potential modulation. When the inversion layer narrows in the positive part of the cycle, electrons must fill states in the CB at the surface at a higher level than the equilibrium level. The converse happens during the negative part of the cycle. Such a variation implies that the chemical potential is formed by an ac and a dc part, with the former possessing in-phase and out-of-phase components. The derivation proposed by Brews (1974) gives a semiconductor capacitance in the high frequency regime C_s^{HF}, for a p-type substrate, of the form

$$\begin{aligned} C_s^{HF} = & \frac{\epsilon_s}{\lambda_p} \left\{ 1 - \mathrm{e}^{-v_S} + \left(\frac{n_i}{N_A} \right)^2 \left[(\mathrm{e}^{v_S} - 1) \frac{\Delta}{1+\Delta} + \frac{v_S}{1+\Delta} \right] \right\} \times \\ & F^{-1}(v_S + u_B, u_B) \end{aligned} \tag{1.48}$$

where Δ is approximated[13] by

$$\Delta \approx \frac{\mathcal{F}(v_S + u_B, u_B)}{\mathrm{e}^{v_S} - 1} \left[\int_0^{v_S} \frac{\mathrm{e}^{v} - \mathrm{e}^{-v} - 2v}{\mathcal{F}^3(v + u_B, u_B)} \mathrm{d}v - 1 \right] \tag{1.49}$$

[13] see Appendix V of Nicollian and Brews (2003) for additional details.

Oxide and interface charges

The previous discussion regarded the ideal MOS capacitor, where the only active charges are the majority and minority carriers and the fixed dopant ions. Bulk traps have been considered, but only as sources of minority carriers and, for the purpose of the discussion, could have been located far from the active region. Real devices, however, do have interface and oxide defects and charges. The aim of this section is to give an account of the effects of the non-idealities on the MOS characteristics.
Charges associated with the oxide/semiconductor system have been classified under four categories: *interface trapped charges*, *oxide trapped charges*, *mobile oxide charges*, and *fixed oxide charges*. **Interface trapped charges** Q_{it} are positive or negative charges due to structural defects, oxidation-induced defects, or metal impurities. These charges are detrimental for electrical performance of devices because they are in electrical communication with the underlying substrate. On the other hand, this gives the opportunity to characterize the centers responsible for the trapping by electrical methods: interface traps can be charged or discharged according to the position of the surface potential. **Oxide trapped charges** Q_{ot} are positive or negative charges resulting by trapping of electrons or holes into the oxide following avalanche injection, Fowler-Nordheim tunneling, or ionizing radiation. **Mobile oxide charges** Q_m are caused by ionic impurities that can diffuse at suitable temperatures or drift due to an electric field. **Fixed oxide charges** Q_f are usually positive charges related to the oxidation ambient and temperature, cooling condition or substrate surface orientation. Fixed charges are not in electrical communication with the underlying semiconductor substrate. Though, they can be in close proximity to the interface and interfere with carriers by Coulomb interaction.

Interface traps are discussed in depth in the remainder of this section.
From an energetic point of view, interface traps form a continuous distribution of energy levels through the bandgap. The corresponding density is denoted by D_{it}, and it is commonly expressed per unit area per electron volt. Levels below the chemical potential will be occupied by electrons. Depending on the nature of the center, the occupied trap can be either negative or neutral. In analogy with dopants, states that are negatively charged when occupied by an electron are considered *acceptors* and states that are neutral when occupied by an electron are considered *donors*. The interface trap charge density at the equilibrium is given by

$$\begin{aligned} Q_{it}(\psi_S) = & -q \int_{E_V}^{E_C} \mathrm{d}E \Big\{ f(E - q\psi_S - q\phi_B) D_{it}^{a}(E) + \\ & - \left[1 - f(E - q\psi_S - q\phi_B)\right] D_{it}^{d}(E) \Big\} \end{aligned} \tag{1.50}$$

where f is the occupation function and the superscripts a and d denote acceptor and donor state densities, respectively. Interface traps are charged and discharged following the ac modulation of the surface potential, provided that the frequency is sufficiently low for the traps to maintain equilibrium, giving an additional contribution to the capacitance $C_{it} = \mathrm{d}Q_{it}/\mathrm{d}V$. Due to the characteristic of the occupation function, δf is sharply peaked at $E = \mu = q\psi_S + q\phi_B + E_i$. Therefore, if D_{it} is a slow varying function of energy on a

scale of a few $k_B T$, C_{it} is given by a simplified expression[14]

$$C_{it}(\psi_S) \approx q^2 \left[D_{it}^a(q\phi_S) + D_{it}^d(q\phi_S) \right] \equiv q^2 D_{it}(q\phi_S) \tag{1.51}$$

written directly as a function of the surface potential ψ_S.

A complete description of the admittance of the interface trap distribution, in terms of capacitance and conductance, for general ac modulation frequency is a difficult task. The main ingredients have already been introduced in the previous part: trap occupation statistics, capture/emission time constant, trap characteristics (such as energy levels and capture cross section) and the role of the position of the surface potential. Unlike the case of single level traps, the description of a distribution of levels often involves integral equations whose solution requires numerical methods.
According to Lehovec and Slobodskoy (1964) and later works reported in Nicollian and Brews (2003), it is possible to define the conductance of a distribution of interface traps G_{it} as

$$G_{it} = q^2 k_B T \int_{E_V}^{E_C} \frac{D_{it} \tau_n^{-1} \tau_p^{-1} f(1-f)}{\jmath\omega f(1-f) + f\tau_p^{-1} + (1-f)\tau_n^{-1}} \mathrm{d}E \tag{1.52}$$

When D_{it} does not vary rapidly over a few $k_B T$, D_{it} can be taken outside of the integral and

$$G_{it} = q^2 D_{it}(q\phi_S) \tau_n^{-1}(\phi_S) \tau_p^{-1}(\phi_S) \mathcal{H}_G \tag{1.53}$$

where

$$\mathcal{H}_G \equiv - \int_0^1 \frac{\mathrm{d}f}{\jmath\omega f(1-f) + f\tau_p^{-1} + (1-f)\tau_n^{-1}} \tag{1.54}$$

Two effective trap capacitances $C_{it,p}$ and $C_{it,n}$ can be defined to describe separately the interaction with holes and electrons, respectively:

$$C_{it,p} = q^2 D_{it}(q\phi_S) \tau_p^{-1}(\phi_S) \mathcal{H}_{Cp} \qquad C_{it,n} = q^2 D_{it}(q\phi_S) \tau_n^{-1}(\phi_S) \mathcal{H}_{Cn} \tag{1.55}$$

where

$$\begin{aligned} \mathcal{H}_{Cp} &\equiv - \int_0^1 \frac{f}{\jmath\omega f(1-f) + f\tau_p^{-1} + (1-f)\tau_n^{-1}} \mathrm{d}f \\ \mathcal{H}_G &\equiv - \int_0^1 \frac{1-f}{\jmath\omega f(1-f) + f\tau_p^{-1} + (1-f)\tau_n^{-1}} \mathrm{d}f \end{aligned} \tag{1.56}$$

To visualize the role of interface traps in the different regimes of operation of the MOS, it is useful to make use of a pictorial representation in terms of equivalent circuits, shown in Fig. 1.7. The MOS capacitor can be seen as a network of different elements: (a) in accumulation, there is no space charge region, minority carriers are negligible at the interface and the high density of the majority carriers dominate the capacitance, screening the interface states. (c), (d) in inversion minority carriers dominate the capacitance, if

[14] many textbooks quote $C_{it} = qD_{it}$ instead, but from dimensional analysis this is not correct. However D_{it} is often expressed in cm^{-2} eV^{-1} and in that units energy is given by $E(\text{eV}) = qV$, where $q = 1$. Hence $C_{it} = q^2 D_{it} = 1 \times 1.6 \cdot 10^{-19} D_{it}$. If D_{it} is given in cm^{-2} J^{-1}, then $C_{it} = (1.6 \cdot 10^{-19})^2 D_{it}$. This can be found in Ng (2002), p.183.

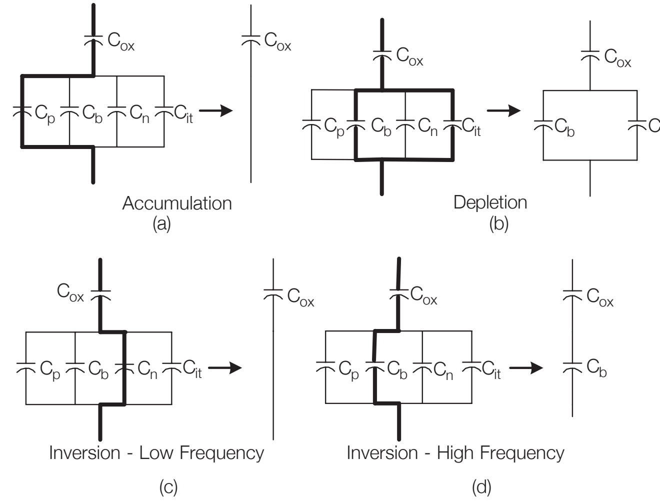

Figure 1.7: Capacitance of a p–type MOS capacitor for various bias conditions. The response of the majority carriers, the charges in the bulk space charge region, the minority carriers, and the interface traps is given in terms of C_p, C_b, C_n, and C_{it} capacitance, respectively.

the frequency is sufficiently low, while space charge region capacitance dominates at higher frequencies, respectively. (b) only in depletion the interface traps can contribute effectively to the device capacitance, making this regime the most interesting for interface characterization.
In depletion, for p-type, $\tau_p^{-1} \gg \tau_n^{-1}$ the interface trap admittance Y_{it} can be written in terms of an equivalent parallel capacitance C_P and an equivalent parallel conductance G_P: $Y_{it} = \jmath\omega C_P + G_P$, where

$$C_P \equiv \frac{C_{it}}{\omega\tau_p \tan(\omega\tau_p)}$$
$$\frac{G_P}{\omega} \equiv \frac{\log\left[1 + (\omega\tau_p)^2\right]}{2\omega\tau_p} \tag{1.57}$$

and C_{it} is the interface traps capacitance in the limit of low frequency given by Eq. 1.51

For comparison, in a MOS capacitor biased in depletion, the single level trap described in section 1.1 will give an equivalent parallel conductance

$$\frac{\langle G_P \rangle}{\omega} = C_T \frac{\omega\tau}{1 + (\omega\tau)^2} \tag{1.58}$$

where

$$C_T = k_B T N_T f(1 - f) \tag{1.59}$$

and N_T = number of traps per unit area.

Oxide trapped charges, and interface trapped charge themselves, create local fluctuations of the electric field at the interface resulting in a local fluctuation of the surface potential ψ_S. The probability distribution of these fluctuations can be assumed gaussian and written for the dimensionless surface band-bending v_S in this form

$$\mathcal{P}(v_S) = \frac{1}{\sqrt{2\pi\sigma_S^2}} \exp\left[-\frac{(v_S - \langle v_S \rangle)^2}{2\sigma_S^2}\right] \tag{1.60}$$

Under this assumption the macroscopic equivalent parallel conductance is averaged over the local fluctuations and is given by

$$\frac{\langle G_P \rangle}{\omega} = \frac{q^2}{2} \int_{-\infty}^{\infty} \frac{D_{it}}{\omega \tau_p} \log(1 + \omega^2 \tau_p^2) P(v_S) \mathrm{d}v_S \tag{1.61}$$

valid in depletion. The time constant entering the Eq. 1.61 corresponds to the mean value of the band bending potential and, in analogy with Eq. 1.31, is given by

$$\tau_p \approx \frac{\mathrm{e}^{\langle v_S \rangle}}{\sigma_p v_{th} N_A} \tag{1.62}$$

for holes, in p-type substrates. In the case of n-type substrates, the time constant for electrons is given by

$$\tau_n \approx \frac{\mathrm{e}^{-\langle v_S \rangle}}{\sigma_n v_{th} N_D} \tag{1.63}$$

By defining the auxiliary dimensionless quantities

$$\xi \equiv \omega \tau_p \approx \omega \frac{\mathrm{e}^{\langle v_S \rangle}}{\sigma_p v_{th} N_A} \quad \text{and} \quad \eta \equiv v_S - \langle v_S \rangle = \frac{q}{k_B T}(\psi - \langle \psi_S \rangle) \tag{1.64}$$

Eq. 1.61 can be written in its final form

$$\frac{\langle G_P \rangle}{\omega} = \frac{q^2 D_{it}}{2\xi\sqrt{2\pi\sigma_S^2}} \int_{-\infty}^{\infty} \exp\left(-\frac{\chi^2}{2\sigma_S^2}\right) \exp(-\chi) \log(1 + \xi^2 \exp 2\chi) \mathrm{d}\chi \tag{1.65}$$

1.3 Electron Paramagnetic Resonance

In the first part of the chapter, the electronic structure and transport properties of germanium were discussed, together with the characteristics of electrically active centers that may have levels in the bandgap. Electrical properties of semiconductors are very sensitive to small variations in material composition: tiny amount of impurities can be revealed and the corresponding energy level in the bandgap can be measured. The same is true for traps at the interface. In this respect, electrical techniques have proven to be invaluable tools in semiconductor material science and characterization. However, purely electrical techniques lack the possibility to investigate the microstructure of such centers in a direct way. Fundamental processes, like carrier emission and trapping, are scarcely affected by the direction of the external electric field and the local symmetry remains hidden. In order to gain a deeper insight into the atomic configuration, different processes

have to be exploited. Electron Paramagnetic Resonance[15] (Электронный Парамагнитный Резонанс, ЭПР – EPR, also called Electron Spin Resonance – ESR) is a physical phenomenon observed for the first time by the soviet physicist Евгений Константинович Завойский[16] (Yevgeny Konstantinovich Zavoisky) at the Казанский государственный университет (Kazan' State University) (Zavoisky, 1945) and later independently by Brebis Bleaney at the University of Oxford. EPR consists in a direct transition between electronic spin levels split by a magnetic field (Zeeman levels). The Zeeman energy splitting may depend on the orientation of the magnetic field with respect to the axis of symmetry of the center involved in the transition. This interdependency opens the possibility to characterize the microstructure, by studying the modification of the resonance condition upon change in magnetic field. Needless to say, the most important limitation is that a nonzero Zeeman energy splitting is essential and only centers with unpaired spins (paramagnetic centers) can be studied. Fortunately, impurities and defects in crystals are very often paramagnetic and this technique can provide unique information on the electronic wavefunction and the configuration of the surrounding nuclei (Spaeth and Overhof, 2003). Since the early times of EPR spectroscopy, it has been applied to the study of semiconductors and among the copious contributions to the field it is worthwhile to mention the proof of the location of the conductance band minimum in silicon along the X direction at $k = 0.85/a$ by Feher (1959). Among the spectroscopic techniques, EPR stands in the microwave region of the electromagnetic spectrum, with frequencies in the range $\approx 1 - 300\,\mathrm{GHz}$ and magnetic fields up to $14\,\mathrm{T}$[17].

The physical principle behind EPR is the Zeeman splitting of the electronic levels due to the interaction of a magnetic moment μ with a magnetic field $\mathbf{B}_0$. The corresponding energy is given by

$$U = -\mu \cdot \mathbf{B}_0 \tag{1.66}$$

From quantum mechanics (Sakurai, 2006), the magnetic moment is related to the dimensionless orbital angular momentum operator $\mathbf{L}$ and the spin angular momentum operator $\mathbf{S}$ by

$$\mu = -\mu_B \left(\mathbf{L} + g_e \mathbf{S}\right) \tag{1.67}$$

where

$$\mu_B = \frac{q\hbar}{2m_e} \approx 9.27 \cdot 10^{-24}\,\mathrm{J/T} \tag{1.68}$$

is called *Bohr's magneton*[18] and the dimensionless quantity g_e, or free electron *g-factor*, is one of the physical quantities that has been determined with the highest precision

---

[15] the name electron paramagnetic resonance was introduced for the first time by H. E. Weaver, from Varian Associates.

[16] On the basis of this phenomenon was developed a spectroscopic technique that has been registered in the Государственный реестр открытий СССР (State Register of scientific discoveries of the USSR) on July 12, 1944 (from `http://ross-nauka.narod.ru/`). At the close of World War II, microwave and electronic technology had advanced to the point where spectrometers could be constructed with the required sensitivity and resolution.

[17] specialized high magnetic field laboratories in Europe, in the USA and in Japan have been attracted by EPR spectroscopy, too. Magnetic field above $20\,\mathrm{T}$ allowed to operate EPR spectrometer up to $600\,\mathrm{GHz}$ (Herlach and Perenboom, 1995).

[18] magnetic nuclei also have an angular momentum $\mathbf{I}$ due to the nuclear spin and a magnetic moment can be defined as $\mu_I = g_n \mu_n \mathbf{I}$. g_n is the *nuclear gyromagnetic* factor and μ_n is the nuclear magneton: $\mu_n = q\hbar/2m_p = m_e/m_p \mu_B \approx \mu_B/1836.27$.

(Odom et al., 2006)

$$g_e/2 = 1.001\,159\,652\,180\,85(76) \quad (1.69)$$

The small deviation from $g = 2$, the value predicted by the Dirac equation, is due to the anomalous magnetic moment of the electron (Schwinger, 1948), a quantum electrodynamic effect explained in terms of electron interaction with the fluctuating vacuum.

The minus sign in Eq. 1.67 arises from the electronic charge and indicates that the angular and the magnetic momenta are antiparallel. The equation can be written in a more convenient form: an effective g-factor is introduced in order to express the magnetic moment as a function of the spin $\mathbf{S}$ alone:

$$\mu = -g\mu_B\mathbf{S} \quad (1.70)$$

The g-factor can be expressed by the approximate Landé formula (Poole, 1996)

$$g \approx \frac{3}{2} + \frac{S(S+1) - L(L+1)}{2J(J+1)} \quad (1.71)$$

where $\mathbf{J} = \mathbf{L} + \mathbf{S}$ is the total angular momentum operator and J, S, L are the eigenvalues for the operators $\mathbf{J}, \mathbf{S}, \mathbf{L}$. In the case of isolated spins, $\mathbf{L} = 0$ and g equals the free electron value g_e. For isolated paramagnetic atoms, both spin and angular momenta contribute to the magnetic momentum and which dominates depends on the quantum numbers of the orbital of the unpaired electron. Moving to the solid state, the crystal potential can effectively *quench* the angular momentum by decoupling the spin and the orbital motion. The more effective is the quenching, the closer is the g-factor to g_e. Also, all s-state paramagnetic electrons behave almost like free electrons due to the lack of spin-orbit interaction. However, small spin-orbit first order effects may come in, either by overlap effects between the s-electron and the electron shells of the neighbor atoms or higher order effects (see next section for more details). For lower symmetry centers, the g-factor can vary upon rotation of the field with respect to the crystal axis, revealing the underlying symmetry. Moreover, the surrounding magnetic environment may induce additional splitting of the energy levels.

The energy difference between subsequent orientation quantum numbers is, according to Eq. 1.66,

$$\Delta E = g\mu_B B_0 \quad (1.72)$$

where the magnetic field has been taken conventionally along the z-axis. The resonant transition, therefore, requires a quantum energy satisfying the condition

$$\hbar\omega = \Delta E \quad (1.73)$$

When $g \approx 2.0$, microwave photons at the conventional frequency of 10 GHz (X-band) meet the resonance condition for $B_0 \approx 0.35\,\mathrm{T}$.

The energies of paramagnetic species can be described effectively in terms of *spin* coordinates only, by considering the spatial degrees of freedom of the wave function as constant of motion. Indeed, the energy available for inducing magnetic dipole interactions are of the order of few tens μeV, while the energy difference necessary for the electronic transitions is three order of magnitude bigger, usually greatly exceeding the thermal energy. Therefore, the ground state with electron spin S and m nuclear spins is described

by a *spin* Hamiltonian of the form (Spaeth and Overhof, 2003)

$$\mathcal{H}_0 = \mathcal{H}_{Z,e} + \mathcal{H}_{hf} + \mathcal{H}_{Z,n} + \mathcal{H}_{FS} + \mathcal{H}_Q \tag{1.74}$$

$$\mathcal{H}_{Z,e} = \mu_B \mathbf{S} \cdot \tilde{g} \cdot \mathbf{B}_0 \quad \text{electron Zeeman interaction} \tag{1.75}$$

$$\mathcal{H}_{hf} = \sum_{i=1}^{m} \mathbf{I_i} \cdot \tilde{A}_i \cdot \mathbf{S} \quad \text{hyperfine interaction} \tag{1.76}$$

$$\mathcal{H}_{Z,n} = \sum_{i=1}^{m} g_{n,i}\mu_n \mathbf{I_i} \cdot \mathbf{B}_0 \quad \text{nuclear Zeeman interaction} \tag{1.77}$$

$$\mathcal{H}_{FS} = \mathbf{S} \cdot \tilde{D} \cdot \mathbf{S} \quad \text{fine-structure interaction} \tag{1.78}$$

$$\mathcal{H}_Q = \sum_{i,j=1}^{m} \mathbf{I_i} \cdot \tilde{Q_{i,j}} \cdot \mathbf{I_j} \quad \text{nuclear quadrupole interaction} \tag{1.79}$$

where the spatial degrees of freedom have been incorporated into the matrices $\tilde{g}$, $\tilde{A}$, $\tilde{D}$, $\tilde{Q}$[19].

For all the cases of interest in this thesis, the leading term in $\mathcal{H}_0$ is the **electron Zeeman interaction** (Eq. 1.75). In the previous discussion, the spin-orbit interaction contribution $\mathcal{H}_{so} = \lambda \mathbf{L} \cdot \mathbf{S}$ has been neglected, assuming complete quenching of the orbital momentum by the crystal potential. However, applying second order perturbation theory expansion in the spin-orbit coupling constant λ, the contribution of the spin-orbit term can be nonzero due to the admixture of excited states to the ground state. In this formalism, the g-factor can be related to the electronic wave functions as follows

$$\tilde{g} = g_e \tilde{1} + \lambda \sum_{n \neq 0} \frac{\langle \Psi_0 | L_i | \Psi_n \rangle \langle \Psi_n | L_j | \Psi_0 \rangle + \text{compl. conj.}}{E_n - E_0} \tag{1.80}$$

where $\langle \Psi_0 |$, $\langle \Psi_n |$ are the ground state and the nth excited state wave functions, respectively The larger the spin-orbit coupling and the closer the excited state to the ground state, the larger the g shift $\delta g = g - g_e$. Typically, δg is in the range $10^{-4} - 10^{-2}$, for weak spin-orbit coupling $\lambda \approx 10^2 - 10^3\,\text{cm}^{-1}$. Governing the largest term in the spin Hamiltonian, the g-factor can be used as the fingerprint to identify the paramagnetic center.

In anisotropic system the g-factor can be represented as a matrix. For a given set of axis (x', y', z') it is possible to write

$$\tilde{g} = \begin{bmatrix} g'_{x'x'} & g'_{x'y'} & g'_{x'z'} \\ g'_{y'x'} & g'_{y'y'} & g'_{y'z'} \\ g'_{z'x'} & g'_{z'y'} & g'_{z'z'} \end{bmatrix} \tag{1.81}$$

The g-matrix is symmetric and it is always possible to find a basis (x, y, z) that diagonalizes g

$$\boldsymbol{g} = \begin{bmatrix} g_x & 0 & 0 \\ 0 & g_y & 0 \\ 0 & 0 & g_z \end{bmatrix} \tag{1.82}$$

[19]these quantities are often called tensors, although they do not transform as tensors under rotation (Abragam and Bleaney, 2012).

and the electronic Zeeman contribution in the spin Hamiltonian takes on the form

$$\mathcal{H}_{Z,e} = \mu_B \left(g_x S_x B_x + g_y S_y B_y + g_z S_z B_z \right) \tag{1.83}$$

In the case of axial symmetry, the following equalities hold

$$g_{//} = g_z \tag{1.84}$$
$$g_{\perp} = g_x = g_y \tag{1.85}$$

and z is called *principal axis*. By defining θ as the angle between the magnetic field and the principal axis, g could be written as

$$g^2 = g_{\perp}^2 \sin^2\theta + g_{//}^2 \cos^2\theta \tag{1.86}$$

The presence of magnetic nuclei within the span of the electronic wave function results in the magnetic interaction between the magnetic momentum of the unpaired electron and the magnetic momenta of the nuclei described by the **hyperfine interaction** (*hf*) term (Eq. 1.76). The *hf* interaction is the sum of an isotropic term $\mathcal{H}_F$ given by the *Fermi contact interaction* and the electron-nuclear dipole-dipole coupling $\mathcal{H}_{dd}$:

$$\mathcal{H}_F = -\frac{2}{3}\mu_0 g \mu_B g_n \mu_n |\Psi(\mathbf{r}=0)|^2 = A_0 \mathbf{I}\cdot\mathbf{S} \tag{1.87}$$
$$\mathcal{H}_{dd} = \frac{g\mu_B g_n \mu_n}{r^3}\left[\frac{3(\mathbf{I}\cdot\mathbf{r})(\mathbf{S}\cdot\mathbf{r})}{r^2} - \mathbf{I}\cdot\mathbf{S}\right] \tag{1.88}$$
$$\tag{1.89}$$

where $\mathbf{r}$ is the distance between the electron and the nucleus. The anisotropic part of the *hf* interaction can be understood as originating from the classical dipole-dipole interaction, written in the quantum mechanics formalism as an operator by means of the correspondence principle. On the other hand, the Fermi contact interaction is a purely relativistic quantum mechanical effect[20]. The interaction is often called *superhyperfine* (*shf*) when the nuclei of the lattice surrounding the paramagnetic center are involved. In crystals, due to the large number of nuclei in special symmetry arrangement, the *shf* splitting of the spectra are often the most powerful source of information on the structure of the center. The isotropic part is actually a local probe of the magnitude of the electron wave function at the particular lattice sites. In many practical cases, however, the number of such nuclei is also a limitation, resulting in too many *shf* lines superimposed with rather similar *shf* splitting. Indeed, each nucleus has its own *shf* matrix with its own principal axis and the magnitude of the *shf* interaction depends on the relative orientation with $\mathbf{B}_0$. In many cases, the *shf* structure can be resolved by double resonance experiments (Feher, 1959), giving one of the most important clues for the identification of the structure of a paramagnetic center.

The **nuclear Zeeman interaction**, the nuclear counterpart of the electron Zeeman interaction, is usually negligible in the spin Hamiltonian. The nuclear magneton, indeed, is much smaller than Bohr's magneton due to the ratio between electron and proton mass:

[20] although a classical analogue can be found in the limit of a point magnetic dipole as shown, for instance, by Jackson (1999), p. 184.

$\mu_n/\mu_B = m_e/m_p \approx 1/1836$.

Magnetic dipole-dipole interactions between the unpaired electrons are described by the **fine-structure interaction** term in the spin Hamiltonian. Together with the electrical field felt through the spin-orbit interaction, this term leads to a splitting of the levels in zero magnetic field, and is commonly called *zero-field splitting*. It vanishes for $S = 1/2$ and it will be neglected in the following.

When $I > 1/2$, the non-spherical charge distribution in the nucleus is described by the nuclear electric quadrupole momentum. This charge distribution can couple to electric field gradients through the **nuclear quadrupole interaction**. Electric field gradients are generated by the electrons and other nuclei in its close vicinity. Nuclear quadrupole interaction manifests itself as a shift of the resonance and the appearance of forbidden transitions, but, being second-order effects, they are difficult to observe.

Eq. 1.74 accurately describes the spin system in *static* condition. In quantum mechanics the description of the temporal change of a quantum observable is given by the Poisson bracket with the Hamiltonian. For instance, when only the $\mathcal{H}_{Z,e}$ interaction is considered, the temporal evolution of the electronic spin operator can be written as

$$\dot{\mathbf{S}} = \frac{J}{\hbar}[\mathcal{H}, \mathbf{S}] = \frac{\mu_B}{\hbar}\mathbf{g} \cdot (\mathbf{B}_0 \times \mathbf{S}) \tag{1.90}$$

The link with macroscopic accessible quantities is represented by the expectation values of the magnetic dipole momentum $\langle \mu_\mathbf{S} \rangle$: the electronic magnetization vector

$$\mathbf{M}_S = \langle \mu_\mathbf{S} \rangle = -\mu_B \mathbf{g} \cdot \langle S \rangle \tag{1.91}$$

Working out the derivative in Eq. 1.90, the equations of motion for the corresponding classical momenta are obtained[21]

$$\frac{\mathrm{d}\mathbf{M}_S}{\mathrm{d}t} = -\frac{\mu_B}{\hbar}\mathbf{g} \cdot (\mathbf{M}_S \times \mathbf{B}_0) \tag{1.92}$$

describing the motion of the magnetization in a static magnetic field, identical to the classical equations of motion for the Larmor precession. The precession frequency for electrons is given by

$$\omega_L = \frac{\mu_B g B_0}{\hbar} \tag{1.93}$$

In a resonance experiment, the transition between Zeeman energy levels characterized by the magnetic quantum number m_S is induced by the interaction of the magnetic dipole momenta and an oscillating magnetic field of frequency ω perpendicular to the static B_0, indicated conventionally by the amplitude B_1. When B_1 oscillates at microwave frequency of about 10 GHz, which is a typical experimental situation, the static magnetic field necessary to match ω with the Larmor frequency is of the order of 330 mT.[22] The total magnetic field at the sample is the sum of the static and the oscillating terms and the time dependent spin Hamiltonian can be written in the form

$$\mathcal{H}(t) = \mathcal{H}_0 + \mathcal{H}_W \cos(\omega t) \tag{1.94}$$

[21] this is a manifestation of the Ehrenfest's teorem

[22] notice the correspondence with the simple quantum description of Eq. 1.74

In a two level system, the transition probability from a state $|m_S = -1/2\rangle$ (or $|-\rangle$) to $|m_S + 1 = +1/2\rangle$ (or$|+\rangle$) can be calculated by time dependent perturbation theory (as long as $B_1 \ll B_0$, which is usually the case) through the Fermi's Golden Rule (Sakurai, 2006)

$$W(- \rightarrow +) = \qquad \text{stimulated absorption} \tag{1.95}$$

$$= W(- \rightarrow +) = \qquad \text{stimulated emission} \tag{1.96}$$

$$= \frac{1}{4}\hbar^2 |\langle -|\mathcal{H}_W|+\rangle|^2 \hat{g}(\omega) \tag{1.97}$$

where $\hat{g}(\omega)$ is a form function of the transition, used to describe the fact that neither the static magnetic field experienced by the electron during the transition is invariably constant, nor the energy levels, or the microwave frequency assume infinitesimally sharp values. $\hat{g}$ is normalized to unity so that

$$\int_0^\infty \hat{g}(\omega) \mathrm{d}\omega = 1 \tag{1.98}$$

By considering $\mathcal{H}_W = \mu_B \mathbf{S} \cdot \tilde{g} \cdot \mathcal{B}$, the transition probability is given by

$$W = \frac{1}{4} \frac{g^2 \mu_B^2}{\hbar^2} B_1^2 \hat{g}(\omega) \tag{1.99}$$

The population of the two levels $|-\rangle$ and $|+\rangle$, indicated by N_- and N_+, respectively, can be described by rate equations, similarly to the case of the occupation levels in electronic transitions. The appropriate rate for the magnetic dipole stimulated transition from the lower to the upper state and vice-versa are $W_\uparrow$ and $W_\downarrow$, respectively. Additionally, two spontaneous relaxation transitions are defined as $R_\uparrow$ and $R_\downarrow$, accordingly. Given the constraint $N = N_- + N_+$, it holds

$$\frac{\mathrm{d}N-}{\mathrm{d}t} = -(W_\uparrow + R_\uparrow)N_- + (W_\downarrow + R_\downarrow)N_+ \tag{1.100}$$

$$\frac{\mathrm{d}N+}{\mathrm{d}t} = (W_\uparrow + R_\uparrow)N_- - (W_\downarrow + R_\downarrow)N_+ \tag{1.101}$$

$$\tag{1.102}$$

In the case of strong irradiation, when $R \ll W$ and $W_\uparrow \equiv W_{\mathrm{EPR}} \equiv W_\downarrow$, the time evolution of the net polarization $\Delta N \equiv N_- - N_+$ is given by

$$\frac{\mathrm{d}\Delta N}{\mathrm{d}t} = -2W_{\mathrm{EPR}} \Delta N \tag{1.103}$$

A characteristic time can be defined as $\tau_{\mathrm{EPR}} = 2W$ to describe the exponential decay of the polarization

$$\Delta N \sim \exp\left(\frac{t}{\tau_{\mathrm{EPR}}}\right) \tag{1.104}$$

Eq. 1.104 predicts $\Delta N \rightarrow 0$ for $t \rightarrow \infty$, therefore in the limit of very strong microwave irradiation no net microwave absorption is observed. The transition is said to be *saturated*. In the opposite case of zero incident radiation (out of resonance), $W_\uparrow = W_\downarrow = 0$ and the time derivatives vanish in thermal equilibrium. Therefore the detailed balance principle holds yielding

$$R_\uparrow N_- = R_\downarrow N_+ \tag{1.105}$$

and the occupation ratio N_+/N_- is given by the Boltzmann statistics[23]

$$\frac{N_+}{N_-} = \mathrm{e}^{-\Delta E/k_B T} \tag{1.106}$$

The occupation difference at the equilibrium ΔN_0 is then given by

$$\Delta N_0 = N \tanh \frac{\Delta E}{2k_B T} \approx N \frac{\Delta E}{2k_B T} \tag{1.107}$$

It can be noticed that system polarization is very small, $\Delta N_0 \approx 10^{-3}$ at room temperature and $B_0 \approx 330\,\mathrm{mT}$. The observation of microwave transition requires very high spectrometer sensitivity, that has been achieved only after the development of the microwave technology for radar applications during the second World War.
The paramagnetic susceptibility χ is calculated as

$$\chi = \frac{M}{B_0} \approx \frac{N\mu_B^2}{k_B T}\frac{g}{2} \tag{1.108}$$

and the Curie law of paramagnetism is recovered when $g = 2$. Now, quite a good deal of equations have been set up to illustrate the simple rate equation two level model, however one more is necessary to consider the description complete: the stationary occupation resulting from simultaneous irradiation and relaxation transitions between levels 1 and 2. The return to the equilibrium from a non-equilibrium state after the sudden removal of the irradiation ($W_{\mathrm{EPR}} = 0$) can be written as

$$\Delta N(t) = A\mathrm{e}^{-t/T_1} + \Delta N_0 \tag{1.109}$$

where

$$T_1 = \frac{1}{1 + \mathrm{e}^{-\Delta E/k_B T}} = \frac{1}{R_\uparrow + R_\downarrow} \approx \frac{1}{2R} \quad \text{when } \Delta E \ll k_B T \tag{1.110}$$

T_1 represents the characteristic time of the return to equilibrium from a off-equilibrium state and is usually called *longitudinal* relaxation time. Finally, it is possible to write:

$$\Delta N = \frac{\Delta N_0}{1+s} \quad \text{where } s = \frac{g^2\mu_B^2}{2\hbar^2} B_1^2 T_1 \hat{g}(\omega) \tag{1.111}$$

The microwave power P which can be absorbed at resonance is given by the product of the transition rate, times the number of centers times the energy per absorbed photon:

$$P = \frac{g^2\mu_B^2}{4\hbar^2} B_1^2 \frac{\Delta N_0}{1+s}\hbar\omega\hat{g}(\omega) \tag{1.112}$$

$$= \frac{N(\hbar\omega)^2 g^2\mu_B^2/\hbar^2 B_1^2 \hat{g}(\omega)}{8k_B T\left[1 + 1/2 g^2\mu_B^2/\hbar^2 B_1^2 T_1 \hat{g}(\omega)\right]} \tag{1.113}$$

As long as $s \ll 1$, P increases as B_1^2.

[23] in the vast majority of the systems $\Delta E \ll k_B T$ in all experimental conditions, therefore the use of the classical statistics in place of the Fermi-Dirac distribution is justified.

By taking full advantage of the Ehrenfest's teorem, it is possible to recognize in the quantum description of the oscillating spin Hamiltonian the dynamics of a classical macroscopic paramagnetic magnetization $\mathbf{M}$ in a time dependent magnetic field $\mathbf{B} = \mathbf{B_0} + \mathbf{B_1}(t)$ described by the Bloch equations

$$\frac{\mathrm{d}\mathbf{M}}{\mathrm{d}t} = \gamma(\mathbf{M} \times \mathbf{B}) \tag{1.114}$$

where γ corresponds to $g\mu_B/\hbar$. The oscillating B_1 introduces an effective relaxation for the transverse components of the magnetization $\mathbf{M}_\perp$ (the components perpendicular to $\mathbf{B}_0$), which are not related to the energy of the system. This relaxation is described by a characteristic time T_2, also called *transverse relaxation time*, governing the decay of $\mathbf{M}_\perp$. By solving Eq. 1.114 [24], it is possible to write the complex magnetic susceptibility $\chi = \chi' - \jmath\chi''$ as

$$\chi' = \frac{g\mu_B(\omega-\omega_0)T_2^2 M_0}{2\hbar\left[1+(\omega-\omega_0)^2T_2^2\right]} \qquad \text{dispersive part} \tag{1.115}$$

$$\chi'' = \frac{g\mu_B T_2 M_0}{2\hbar\left[1+(\omega-\omega_0)^2T_2^2\right]} \qquad \text{absorptive part} \tag{1.116}$$

$$M_0 = M_z \tag{1.117}$$

where $\omega_0 = g\mu_B/\hbar B_0$, and it was assumed $\mathbf{B}_0//z$, $B_1 \ll B_0$ for simplicity.
χ'' follows a Lorentzian line shape with half width

$$\Delta\omega_{1/2} = \frac{2}{T_2} \tag{1.118}$$

and maximum

$$\chi''_{\text{max}} = \frac{g\mu_B}{2\hbar}T_2M_0 \equiv \frac{\chi_0\omega_0}{\Delta\omega_{1/2}} \tag{1.119}$$

defining $\chi_0 = M_0/B_0$. It can be noticed that T_2 determines the line width of the Lorentzian line and that, at thermal equilibrium, χ''_{max} can be interpreted as the susceptibility of the system multiplied by the quality factor of the resonance $\omega_0/\Delta\omega_{1/2}$. Additionally, the area under the EPR line is independent on the values of T_1 and T_2:

$$\int_{-\infty}^{\infty}\chi''\mathrm{d}\omega = \frac{1}{4}\omega_0\chi_0 \tag{1.120}$$

and since χ_0 is proportional to the number of spins, by calibrating the area one can determine the total number of paramagnetic centers[25].

By removing the constraint $B_1 \ll B_0$ a more general relationship is obtained:

$$\chi' = \frac{1}{2}\frac{g\mu_B M_0 T_2}{\hbar\sqrt{1+s}}\frac{T_2(\omega_0-\omega)/\sqrt{1+s}}{1+\left[T_2(\omega_0-\omega)/\sqrt{1+s}\right]^2} \tag{1.121}$$

$$\chi'' = \frac{1}{2}\frac{g\mu_B M_0 T_2}{\hbar(1+s)}\frac{1}{1+\left[T_2(\omega_0-\omega)/\sqrt{1+s}\right]^2} \tag{1.122}$$

[24] technically, the solution is much simplified by a coordinate transformation, the so-called *rotating frame* in which $\mathbf{B}_1$ is constant.

[25] provided the measurement is done without saturating the signal. Additionally many factors affect the sensitivity of the instrument and in practice it is possible to obtain reliable quantitative estimations only in carefully controlled conditions, better with the aid of an internal standard.

where s is the saturation factor already encountered in the two level system. This is an indication of a close link between the Bloch equation and the rate equation descriptions. Within the description of the Bloch equation, the absorbed power is given by

$$P = 2\omega B_1^2 \chi'' \tag{1.123}$$

yielding

$$P = B_0 M_0 \frac{g\mu_B/\hbar B_1^2 T_2}{1 + (\omega - \omega_0)^2 T_2^2 + g^2\mu_B^2/\hbar^2 B_1^2 T_1 T_2} \tag{1.124}$$

The comparison between Eq. 1.112 and Eq. 1.124 allows to identify

$$\hat{g}(\omega) = \frac{2T_2}{1 + (\omega - \omega_0)^2 T_2^2} \tag{1.125}$$

Recalling that $\hat{g}$ is the form factor of the quantum mechanical transition as given by the Fermi's Golden Rule, it follows that the T_2 process determines the line broadening, rather than the T_1 process, limiting the coherence time of the quantum mechanical state.

In the previous discussion, it has been considered only the electronic Zeeman term of the spin Hamiltonian. In the case that $\mathcal{H}_{Z,e}$ is the only relevant term, the line width is determined uniquely by the transverse relaxation time T_2[26]. When other terms of the Hamiltonian are present, but they are not sufficiently strong to split the resonance line in two or more resolved components, an "artificial" broadening is observed. This behavior is called *inhomogeneous* broadening and it is the result of the superposition of different lines whose resonance is within the respective "natural", undisturbed, *homogeneous* line width given by T_2 relaxation. An example of inhomogeneous broadening is typically caused by the superhyperfine interaction, which consists in a great number of unresolved interactions. The superposition of a great number of homogeneous lines with Lorentzian shape results in a Gaussian line shape. In the intermediate case of a partial superposition of closely distributed lines, the resonance signal can be accurately represented by a Voigtian line shape, obtained as the convolution of a Lorentzian line with a Gaussian distribution.
A seminal paper was written by Feher (1959), where he elegantly demonstrates the role of superhyperfine interactions in the resonance of substitutional phosphorous donor in silicon by the use of the Electron-Nuclear DOuble Resonance.

1.4 Spin Dependent Recombination

Carrier transport under the effect of an externally applied electric field $\mathcal{E}$ is described by Eq. 1.24. The current J is proportional to carrier concentration and mobility: p, n and μ_e, μ_p, respectively. When bulk traps dominate generation and recombination, the carrier concentration is described by the rate equation given in Eq. 1.29. To include the contribution of carrier generation by above bandgap light, the equations can be generalized by considering an additional positive term G_L contributing to $\mathrm{d}p/\mathrm{d}t$ and $\mathrm{d}n/\mathrm{d}t$. The higher carrier concentration induced by illumination leads to an increase in recombination rate R, which at equilibrium equals G_L. Carrier density is ultimately limited by the efficiency of the recombination and, as an example, for minority carriers in

[26] one notably example where this is not true is represented by conductive systems, where the electron sea can effectively screen the microwave oscillating field and induce additional relaxation time (Dyson, 1955).

p-type semiconductor it is possible to write the steady state out of equilibrium electron density n in terms of the equilibrium density n_0 as

$$n = n_0 + \tau_p G_L = n_0 + \frac{G_L}{R} \tag{1.126}$$

all the details of the recombination process are included in the characteristic time τ_p, or equivalently in the effective rate R.
Recalling Eq. 1.25, it follows that the conductivity of the semiconductor depends on G_L and R through their effect on carrier density. The influence of the mutual spin orientation of carriers and defects has been observed experimentally in specific recombination processes and tentatively described by a variety of models (Lepine, 1972; Kaplan et al., 1978; Poindexter et al., 1981; Vlasenko et al., 1995; Fanciulli et al., 2005). When the population of the spin states is altered, such as in a resonance experiment, the net recombination rate is affected. As a consequence, carrier density changes according to Eq. 1.126 and, ultimately, there is a net difference in conductivity when the resonance is excited.

$$\text{Signal intensity} \sim \Delta\sigma \sim \Delta n \sim n\frac{\Delta R}{R} \tag{1.127}$$

This change in conductivity between the on-resonance and off-resonance states can be exploited to increase effectively the sensitivity of electron spin resonance techniques. Indeed, electrical measurements are well suited to determine even very small variations of the conductivity especially when small volumes need to be investigated. In this respect Electrically Detected Magnetic Resonance (EDMR) techniques are advantageous in the study of the interfaces and reduced dimensionality systems. On the contrary, the conventional EPR signal depends on the total number of paramagnetic centers, which is proportional to the active volume.

Various models have been proposed to explain the physical mechanisms behind the Spin Dependent Recombination (SDR). The model elaborated by Lepine (1972) invokes the role of singlet-triplet level splitting of the electron and the defect levels (see Fig. 1.8a). In presence of an external magnetic field, photogenerated carriers and paramagnetic defects are mildly polarized (see Eq. 1.107). Recombination from triplet states is forbidden by Pauli exclusion principle, but inducing a resonant transition of either the defect or the free carrier spin, the polarization degree is reduced and recombination is promoted. Following Eq. 1.127, σ is reduced. The model can explain, at least qualitatively, some of the trends observed in EDMR experiments, such as the signal dependence on microwave power P

$$\text{Signal intensity} \sim \frac{P}{1 + \text{const} \times P} \tag{1.128}$$

and the behavior as a function of modulation frequency

$$\text{Signal intensity} \sim \frac{1}{1 + \omega_{\text{mod}}^2 \tau_{\text{Lepine}}^2} \tag{1.129}$$

Nevertheless, due to the reduced polarization degree of free carriers and defect spin population, the model predicts a very small conductivity change ($\Delta\sigma/\sigma \approx 10^{-6}$ on resonance), at least two order of magnitude smaller than the experimental observations.

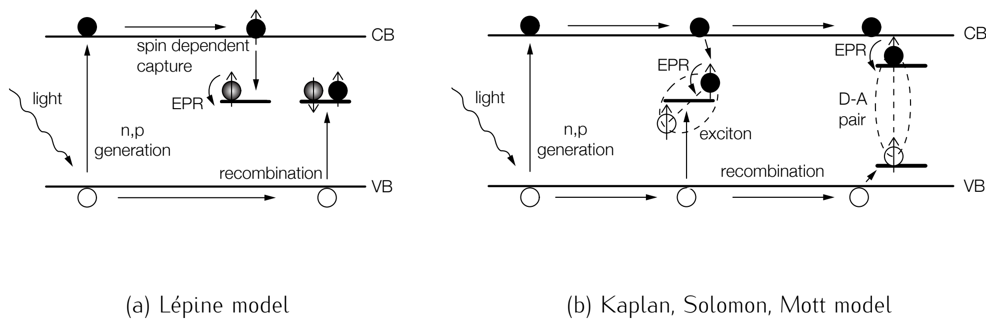

(a) Lépine model

(b) Kaplan, Solomon, Mott model

Figure 1.8: Spin Dependent Recombination mechanisms after Lepine (1972) and Kaplan, Solomon, and Mott (Kaplan et al., 1978).

A refined model has been elaborated by Kaplan, Solomon and Mott to solve the issue (Kaplan et al., 1978). The electrons and holes are assumed to be captured by recombination centers independently of their spin orientation. In a subsequent step, they are thought to form electron-hole pairs localized at one defect, which would lead to an exciton recombination. Or, alternatively, donor-acceptor pair recombination is considered. The main feature is the efficient reduction of singlet state population due to the enhanced recombination, as compared to the triplet state (see Fig. 1.8b). This mechanism markedly enhances the spin polarization degree and, as a consequence, a greater change in conductivity results when the spin resonance is induced and the populations of the two spin levels are equalized. The theoretical estimates predict $\Delta\sigma/\sigma \approx 10^{-2} - 10^{-4}$, in line with experimental observations.

1.5 Bibliography

A. Abragam and B. Bleaney. *Electron Paramagnetic Resonance of Transition Ions*. International series of monographs on physics. OUP Oxford, 2012. ISBN 9780199651528. URL http://books.google.it/books?id=SSD7AAAAQBAJ.

M. Born, R.J. Blin-Stoyle, and J.M. Radcliffe. *Atomic Physics*, chapter IX,11. Dover books on physics and chemistry. Dover Publications, 1989. ISBN 9780486659848. URL http://books.google.it/books?id=NmM-KujxMtoC.

J. R. Brews. An improved high-frequency MOS capacitance formula. *Journal of Applied Physics*, 45(3):1276, 1974. ISSN 00218979. doi: 10.1063/1.1663401. URL http://link.aip.org/link/JAPIAU/v45/i3/p1276/s1&Agg=doi.

FJ Dyson. Electron spin resonance absorption in metals. II. Theory of Electron diffusion and the skin effect. *Physical Review*, 98(2), 1955. URL http://prola.aps.org/abstract/PR/v98/i2/p349_1.

Marco Fanciulli, Omar Costa, Simone Cocco, Gabriele Seguini, Enrico Prati, and Giovanna Scarel. Defects in High-κ Gate Dielectric Stacks. In *NATO Advanced Studies Institute, Series II: Mathematics, Physics and Chemistry*, page 26. Plenum, New York, 2005.

G. Feher. Electron Spin Resonance Experiments on Donors in Silicon. I. Electronic Structure of Donors by the Electron Nuclear Double Resonance Technique. *Physical Review*, 114(5):1219–1244, June 1959. ISSN 0031-899X. doi: 10.1103/PhysRev.114.1219. URL http://prola.aps.org/abstract/PR/v114/i5/p1219_1http://link.aps.org/doi/10.1103/PhysRev.114.1219.

A. Gold and V. Dolgopolov. Temperature dependence of the conductivity for the two-dimensional electron gas: Analytical results for low temperatures. *Physical Review B*, 33(2):1076–1084, January 1986. ISSN 0163-1829. doi: 10.1103/PhysRevB.33.1076. URL http://link.aps.org/doi/10.1103/PhysRevB.33.1076.

R. Hall. Electron-Hole Recombination in Germanium. *Physical Review*, 87(2):387–387, July 1952. ISSN 0031-899X. doi: 10.1103/PhysRev.87.387. URL http://link.aps.org/doi/10.1103/PhysRev.87.387.

Fritz Herlach and Jos A.A.J. Perenboom. Magnet laboratory facilities worldwide-An update. *Physica B: Condensed Matter*, 211(1-4):1–16, May 1995. ISSN 09214526. doi: 10.1016/0921-4526(94)00929-P. URL http://www.sciencedirect.com/science/article/pii/092145269400929P.

J.D. Jackson. *Classical Electrodynamics*. Wiley, 1999. ISBN 9780471309321. URL http://books.google.it/books?id=GuYNngEACAAJ.

D. Kaplan, I. Solomon, and N.F. Mott. Explanation of the large spin-dependent recombination effect in semiconductors. *Journal de Physique Lettres*, 39(4):51–54, February 1978. ISSN 0302-072X. doi: 10.1051/jphyslet:0197800390405100. URL http://dx.doi.org/10.1051/jphyslet:0197800390405100.

K Lehovec and A Slobodskoy. Impedance of semiconductor-insulator-metal capacitors. *Solid-State Electronics*, 7:59–79, 1964. URL http://www.sciencedirect.com/science/article/pii/0038110164901224.

Daniel J. Lepine. Spin-Dependent Recombination on Silicon Surface. *Physical Review B*, 6(2):436–441, 1972.

R. Lindner. Semiconductor Surface Varactor. *Bell System Technical Journal*, 41(3):803–831, May 1962. ISSN 00058580. doi: 10.1002/j.1538-7305.1962.tb00477.x. URL http://ieeexplore.ieee.org/lpdocs/epic03/wrapper.htm?arnumber=6769600.

DC Look. Statistics of multicharge centers in semiconductors: Applications. *Physical Review B*, 24(10):5852, 1981. URL http://prb.aps.org/abstract/PRB/v24/i10/p5852_1.

J.Ross Macdonald. Accurate solution of an idealized one-carrier metal-semiconductor junction problem. *Solid-State Electronics*, 5(1):11–37, January 1962. ISSN 00381101. doi: 10.1016/0038-1101(62)90013-8. URL http://www.sciencedirect.com/science/article/pii/0038110162900138.

Y. Matsumoto. Scattering mechanism and low temperature mobility of mos inversion layers. *Jpn. J. Appl. Phys. Suppl.*, 2:367–370, 1974. URL http://ci.nii.ac.jp/naid/80013133270/en/.

John L Moll. Variable capacitance with large capacity change. In *IRE Wescon Convention Record, Part 3*, pages 32–36, 1959.

K.K. Ng. *Complete Guide to Semiconductor Devices*. A Wiley-interscience publication. Wiley, 2002. ISBN 9780471202400. URL http://books.google.it/books?id=AKeHQgAACAAJ.

E.H. Nicollian and J.R. Brews. *MOS (Metal Oxide Semiconductor) Physics and Technology*. A Wiley-Interscience publication. Wiley, 2003. ISBN 9780471430797. URL http://books.google.it/books?id=HaRwngEACAAJ.

B. Odom, D. Hanneke, B. D'Urso, and G. Gabrielse. New Measurement of the Electron Magnetic Moment Using a One-Electron Quantum Cyclotron. *Physical Review Letters*, 97(3):030801, July 2006. ISSN 0031-9007. doi: 10.1103/PhysRevLett.97.030801. URL http://link.aps.org/doi/10.1103/PhysRevLett.97.030801.

WG Pfann and CGB Garrett. Semiconductor varactors using surface space-charge layers, 1959.

Edward H. Poindexter, Philip J. Caplan, Bruce E. Deal, and Reda R. Razouk. Interface states and electron spin resonance centers in thermally oxidized (111) and (100) silicon wafers. *Journal of Applied Physics*, 52(2):879–884, 1981.

C.P. Poole. *Electron Spin Resonance: A Comprehensive Treatise on Experimental Techniques*. Dover books on physics. Dover Publications, 1996. ISBN 9780486694443. URL http://books.google.it/books?id=P-4PIoi7Z7IC.

M. Riordan and L. Hoddeson. The origins of the pn junction. *IEEE Spectrum*, 34(6):46–51, June 1997. ISSN 00189235. doi: 10.1109/6.591664. URL http://ieeexplore.ieee.org/lpdocs/epic03/wrapper.htm?arnumber=591664.

J.J Sakurai. *Modern Quantum Mechanics*. Pearson Education, 2006. ISBN 9788177585483. URL http://books.google.it/books?id=JCS-S1tLx7MC.

D.K. Schroder. *Semiconductor Material and Device Characterization*. Wiley, 2006. ISBN 9780471749080. URL http://books.google.it/books?id=OX2cHKJWCKgC.

Julian Schwinger. On Quantum-Electrodynamics and the Magnetic Moment of the Electron. *Physical Review*, 73(4):416–417, February 1948. ISSN 0031-899X. doi: 10.1103/PhysRev.73.416. URL http://link.aps.org/doi/10.1103/PhysRev.73.416.

W Shockley and WT Read Jr. Statistics of Recombinations of Holes and Electrons. *Physical Review*, 87:835, 1952. URL http://prola.aps.org/abstract/PR/v87/i5/p835_1.

J.M. Spaeth and H. Overhof. *Point Defects in Semiconductors and Insulators: Determination of Atomic and Electronic Structure from Paramagnetic Hyperfine Interactions*. Physics and Astronomy Online Library. Springer Berlin Heidelberg, 2003. ISBN 9783540426950. URL http://books.google.it/books?id=Ll0oEkkJ5FcC.

Frank Stern and W. Howard. Properties of Semiconductor Surface Inversion Layers in the Electric Quantum Limit. *Physical Review*, 163(3):816–835, November 1967. ISSN 0031-899X. doi: 10.1103/PhysRev.163.816. URL http://link.aps.org/doi/10.1103/PhysRev.163.816.

S.M. Sze and K.K. Ng. *Physics of Semiconductor Devices*. Wiley, 2006. ISBN 9780470068304. URL http://books.google.it/books?id=o4unkmHBHb8C.

Y.P. Varshni. Temperature dependence of the energy gap in semiconductors. *Physica*, 34(1):149–154, January 1967. ISSN 00318914. doi: 10.1016/0031-8914(67)90062-6. URL http://www.sciencedirect.com/science/article/pii/0031891467900626.

L. S. Vlasenko, Yu. V. Martynov, T. Gregorkiewicz, and C. A. J. Ammerlaan. Electron paramagnetic resonance versus spin-dependent recombination: Excited triplet states of structural defects in irradiated silicon. *Physical Review B*, 52(2):1144–1151, 1995.

E Zavoisky. Paramagnetic relaxation of liquid solutions for perpendicular fields. *J. Phys. USSR*, 9:211–245, 1945.

Experimental Methods 2

Allright, I pulled the lever
and pushed the button.
So what's the big secret
to getting this to work?

Piled Higher and Deeper
"Special calibration routine"
Jorge Cham

In this chapter are detailed the characteristics of the samples that have been investigated and the details of the experimental techniques that have been employed to study the properties of the germanium – oxides interfaces. The procedure involved in the data analysis is described in detail.

2.1 Sample Fabrication and Preliminary Characterization

Six different kinds of Ge substrates have been used, of either (001) and (111) surface orientation. Electrical characterization requires doped samples and both *p*- and *n*- type have been employed to investigate the lower half and the upper half region of the bandgap, respectively. Resistive samples are best suited for EDMR characterization in order to reduce dielectric loss in the microwave cavity and undoped substrates have been employed for this reason.
The properties of three different interfaces have been investigated: Ge/GeO_2, Ge/Al_2O_3, and sulfur passivated Ge(S)/Al_2O_3. The electrical characterization of the Ge/GeO_2 interface necessitated an additional capping with Al_2O_3 in order to reduce gate leakage in MOS capacitors.
Sample characteristics and labeling is displayed in Table 2.1 and a pictorial resume is given in Fig. 2.1.

High quality GeO_2 was grown on top of the samples belonging to *H* and *G* series. After dipping the substrate in a buffered HF solution to remove the native oxide, the surface has been oxidized by rapid thermal annealing (RTA) in ultrapure O_2 environment, at a temperature of 400° C, for 20 minutes. The oxide thickness was measured by Spectroscopic Ellipsometry. The recipe is optimized to yield a predominant GeO_2 composition. In order to check the oxide and interface composition, the Ge 3d core level photoemission line has been probed by making use of a X-ray photoelectron spectroscopy (XPS) apparatus

Name	Interface	Surface orientation	Substrate doping	Dopant concentration (cm^{-3})	Oxide thickness (nm)
A0p	Ge/Al_2O_3	(001)	*p*	$4 \cdot 10^{16}$	11.2
A0n	Ge/Al_2O_3	(001)	*n*	$2 \cdot 10^{16}$	11.1
A1p	Ge/Al_2O_3	(111)	*p*	$3.5 \cdot 10^{17}$	10.7
A1n	Ge/Al_2O_3	(111)	*n*	$2.5 \cdot 10^{16}$	10.8
A1u	Ge/Al_2O_3	(111)	undoped	$< 10^{14}$	11.5
G0p	$Ge/GeO_2/Al_2O_3$	(001)	*p*	$4 \cdot 10^{16}$	3.3 / 10.1
G0n	$Ge/GeO_2/Al_2O_3$	(001)	*n*	$2 \cdot 10^{16}$	3.3 / 10.1
G1p	$Ge/GeO_2/Al_2O_3$	(111)	*p*	$3.5 \cdot 10^{17}$	4.3 / 8.8
G1n	$Ge/GeO_2/Al_2O_3$	(111)	*n*	$2.5 \cdot 10^{16}$	4.4 / 8.8
G1u	$Ge/GeO_2/Al_2O_3$	(111)	undoped	$< 10^{14}$	4.3 / 8.8
H1u	Ge/GeO_2	(111)	undoped	$< 10^{14}$	4.3
S0p	$Ge(S)/Al_2O_3$	(001)	*p*	$4 \cdot 10^{16}$	11.3
S0n	$Ge(S)/Al_2O_3$	(001)	*n*	$2 \cdot 10^{16}$	11.1
S1p	$Ge(S)/Al_2O_3$	(111)	*p*	$3.5 \cdot 10^{17}$	10.8
S1n	$Ge(S)/Al_2O_3$	(111)	*n*	$2.5 \cdot 10^{16}$	10.8
S1u	$Ge(S)/Al_2O_3$	(111)	undoped	$< 10^{14}$	12.1

Table 2.1: Sample characteristics and naming scheme. The dopant concentration is the nominal value provided by the supplier and is typically affected by a relative error about 50 %. Oxide thickness has been measured by spectroscopic ellipsometry.

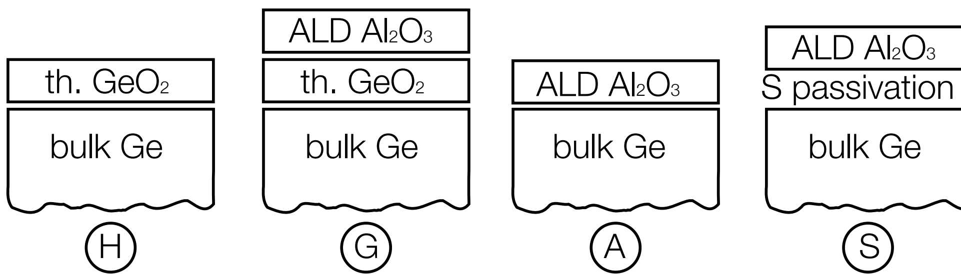

Figure 2.1: Schematic representation of the three interfaces investigated in this thesis, comprising **th**ermal grown germanium oxide, **A**tomic **L**ayer **D**eposition grown alumina, ammonium **s**ulfide **passivated** Ge/Al_2O_3.

equipped with a Mg K_α radiation source (1253.6 eV). The Ge 3d line is reported for comparable O_2 oxidation of Ge(111). The double peak fashion shown in Fig. 2.2 is related to a bulk contribution and an oxide contribution at lower and higher binding energy, respectively. The chemical shift between the two contributions amounts to 3.4 eV which is indicative of a prevailing Ge^{4+} valence state, namely a major GeO_2 stoichiometry, as similarly observed in the case of the O_2 oxidation of the Ge(001) surface (Molle et al., 2008; Baldovino et al., 2008). No impact on the chemical composition is expected from the exposure to ambient condition, as previously investigated by (Molle et al., 2008).

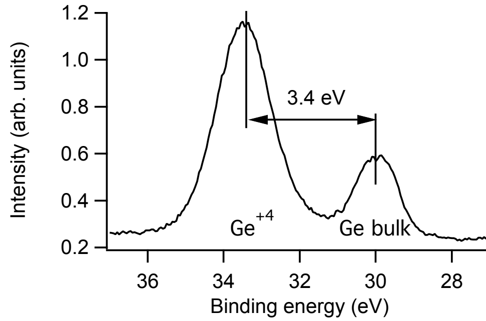

Figure 2.2: XPS spectra of the Ge 3d core level photoemission line. The chemical shift between the bulk and the oxide contributions amounts to 3.4 eV, which is indicative of a dominant Ge^{+4} valence state, confirming the prevalent GeO_2 stoichometry.

After the initial surface cleaning and native oxide removal in buffered HF solution, the samples belonging to *S* series were dipped in a solution of ammonium sulfide $(NH_4)_2S$ 20% for 3 minutes at room temperature (Xie and Zhu, 2007). Then, samples were rinsed in deionized water.

The Al_2O_3 thin film was grown on top of samples belonging to *G, A,* and *S* series by Atomic Layer Deposition (ALD). ALD is a modification of the Chemical Vapor Deposition process in which gaseous precursors are sequentially placed in contact with the substrate surface and the reactor is purged with an inert gas between reagent pulses. The chemical reactions occur exclusively on the substrate below the thermal decomposition temperature of the precursor. At each cycle, the precursor reaches a saturated adsorption level on the substrate surface; the inert gas purge removes from the chamber any excess reagent molecule and volatile by-products. At each cycle the growth is self limited and accurate control on the thickness of the thin film is achieved by adjusting the number of cycles. Al_2O_3 was grown alternating pulses of trimethylaluminum (TMA) and H_2O at 300° C, using N_2 as purging gas, as shown in Fig. 2.3. At each cycle approximately 0.11 nm of Al_2O_3 are grown. 110 cycles were completed, for a target layer thickness of 10−11 nm. No effect in the Ge/GeO_2 interface integrity, where present, is expected from ALD processing as the Al_2O_3 deposition temperature is well within the GeO_2 stability range (Molle et al., 2006).

The quality of the interfaces and the yield of the sulfur passivation was preliminarily investigated by Time-of-Flight Secondary Ion Mass Spectrometry (ToF-SIMS) measurements. By focusing an ion beam of controlled kinetic energy, secondary atoms and molecules are emitted from the bombarded surface and collected via an electrostatic analyzer. Employing ion pulses of the order of nanoseconds, the secondary species travel in short packets with the same energy but different speed, due to the different masses. By measuring the ion current at the analyzer as a function of the ToF it is possible to identify the composition of the packet. By proceeding with a step by step erosion, the composition profile of the sample is reconstructed. 0.5 keV Cs^+ ions were employed for sputtering and 25 keV Ga^+ ions for analysis in an ION-TOF IV instrument, in the same

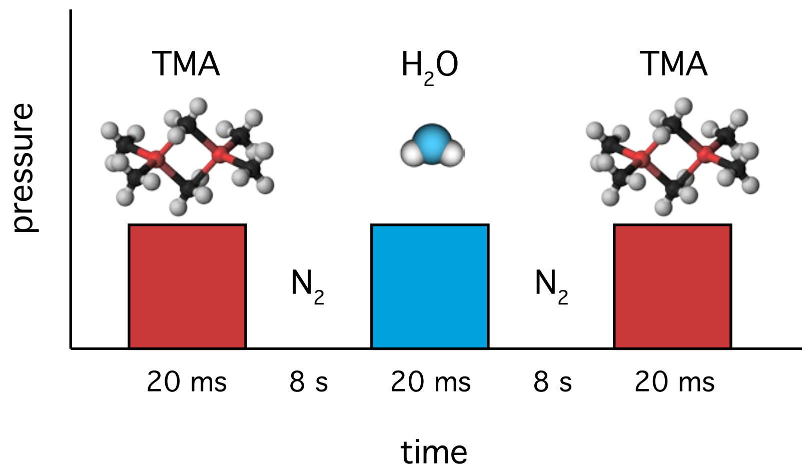

Figure 2.3: Schematics of ALD growth of Al_2O_3 with TMA and H_2O precursors. Each cycle comprises a 20 ms pulse of TMA followed by 8 s purging with N_2, then 20 ms pulse of water, followed by purging. Substrate is held at 300 K, while reagents are introduced at room temperature.

acquisition mode as reported in Lamperti et al. (2011). Secondary ions were collected in negative polarity and intensity normalized to Ge_2 intensity in bulk Ge. Fig. 2.4 compares the depth profiles in series *A* and *S*, confirming that sulfur is still present after the Al_2O_3 growth by ALD. Additionally, ToF-SIMS evidenced the presence of a germanium oxide interlayer, formed during the Al_2O_3 growth that is not influenced by the treatment with ammonium sulfide (Paleari et al., 2014).

Metal gates are deposited on top of the oxide to realize the MOS capacitors for the electrical characterization of the interface. By means of an electron beam evaporator $\approx$ 70 nm of aluminum are deposited through a shadow mask to define circular gates with diameters ranging from 50 μm to 300 μm. Then the proces is repeated to obtain the metalization of the whole back of the sample to ensure a good ohmic contact with the substrate.

2.2 Electrically Detected Magnetic Resonance

EDMR spectroscopy is performed in a conventional EPR spectrometer. A specially designed microwave cavity allows the electrical detection of the electron spin resonance as detailed below.

The Instrument

An EPR spectrometer is an elaborated instrument, reflecting the interplay of the different physical phenomena and technological pieces of art that concur in making possible to irradiate a sample with a intense microwave beam and detect the tiny response of the

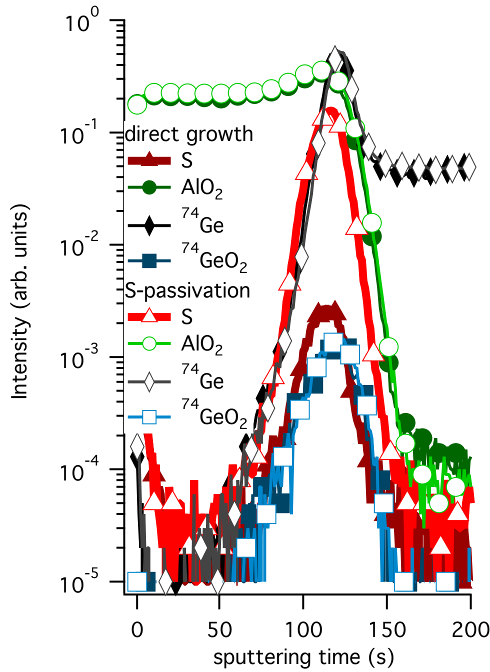

Figure 2.4: Comparison of ToF-SIMS depth profiles in series *A* and *S*, confirming the presence of sulfur at the germanium – oxide interface in fully processed samples. Additionally, ToF-SIMS evidenced the formation of a germanium oxide interlayer during the ALD process, not affected by the ammonium sulfide treatment.

sample. Fig. 2.5 shows a schematic representation of the building blocks that compose the spectrometer. The apparent complexity can be tamed by classifying the functionalities as follows:

- magnetic field control
- microwave generation and detection
- signal conditioning and extraction
- cryogenics

The **magnet** is the core of the spectroscopic power of the technique. A key factor in the very high resolution achieved in g-factor determination (up to $10^{-5} - 10^{-6}$) is the precise regulation of the magnetic field. By means of a smooth and controlled sweep, the Zeeman energy of spin levels is adjusted in order to *resonate* with the energy of the incoming microwave radiation.

Microwave frequency, indeed, is kept constant because for optimal efficiency in generating intense oscillating magnetic field a single mode resonant cavity is employed. Magnetic and electric field distributions are shown in Fig. 2.6. When the correct microwave frequency is sent to the cavity, all the energy of the incoming radiation is stored into the oscillating fields (and is eventually dissipated) minimizing back reflections. By plotting the reflected intensity as a function of the frequency, the so-called pattern mode is obtained (see Fig. 2.7). The resonant cavity is characterized by the quality factor Q defined as

$$Q = 2\pi \frac{\text{energy stored}}{\text{energy dissipated}} \quad \text{per cycle} \tag{2.1}$$

or equivalently $Q = \nu_{res}/\Delta\nu$, for a direct visualization on the pattern mode. When paramagnetic species are present inside the cavity, there is a net effect on the pattern

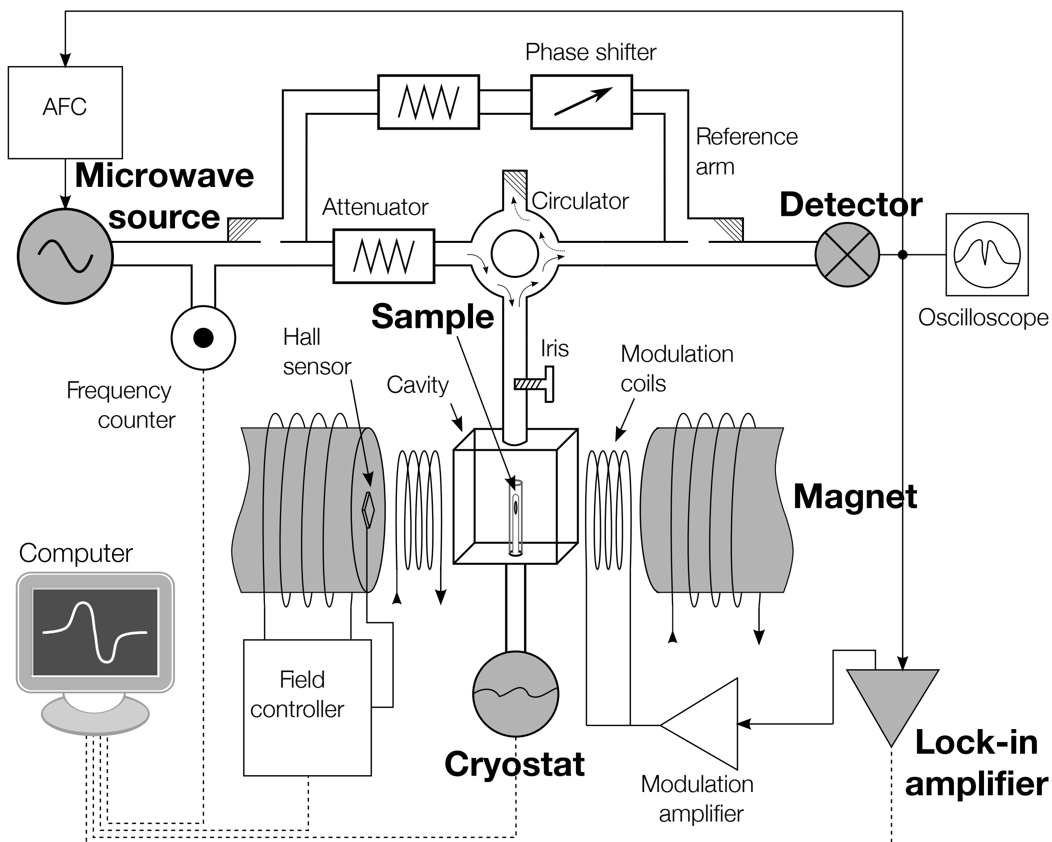

Figure 2.5: Functional scheme of an EPR spectrometer

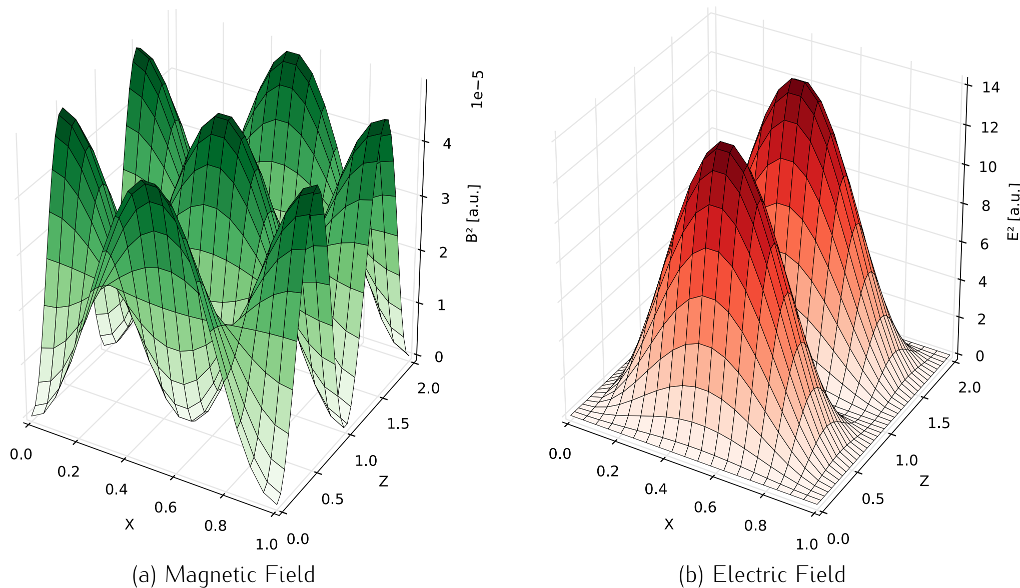

(a) Magnetic Field

(b) Electric Field

Figure 2.6: Magnetic and electric field intensity distribution in a TE_{102} microwave cavity.

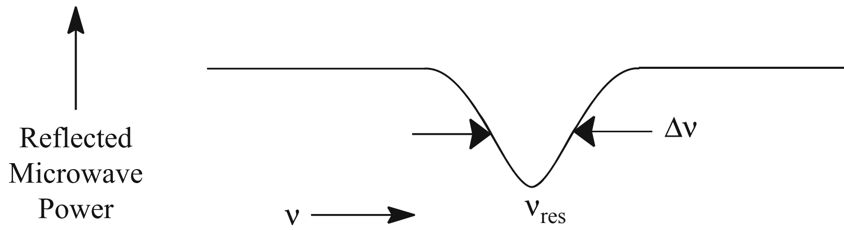

Figure 2.7: Pattern mode.

mode due to the absorptive and dispersive components of the susceptibility χ (see Eq. 1.121), as indicated by Fig. 2.8. Upon resonance there is a change in the pattern mode

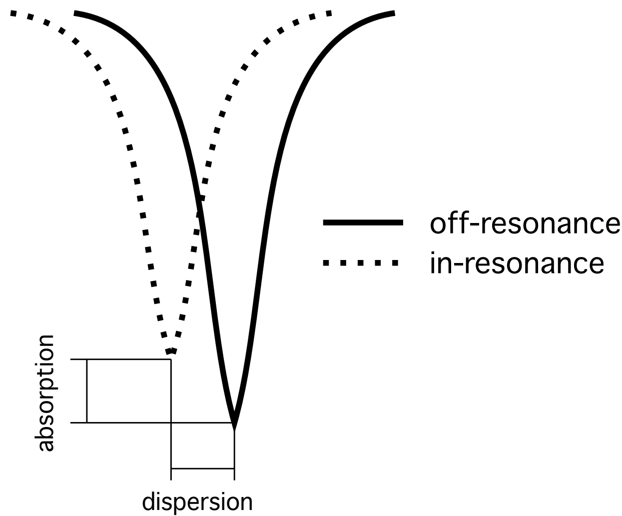

Figure 2.8: Effect of absorptive and dispersive components of χ upon resonance. The effect is highly exaggerated.

resulting in microwave "leakage" to the detector.
The detection of the tiny difference in cavity Q–factor would be a tough challenge without proper **signal conditioning** by means of a lock-in detection technique. Typically, a small magnetic field modulation at frequencies ranging from 1 kHz to 100 kHz is added to the static field to encode the signal at high frequency[1] where it can be extracted from the background noise using a phase sensitive detector. The lock-in detection with magnetic field modulation results in the first derivative of the original absorption signal. When the magnetic field has a sweeping and a oscillating component $B = B_0 + B_m \cos(\omega t)$, the absorption signal $f_L(B)$ can be expanded in B as a Taylor series:

$$f_L(B) = \sum_{n=0}^{\infty} \frac{1}{n!} \frac{\mathrm{d}^n f_L}{\mathrm{d}B^n}\bigg|_{B=B_0} (B - B_0)^n \tag{2.2}$$

$$= \sum_{n=0}^{\infty} \frac{1}{n!} \frac{\mathrm{d}^n f_L}{\mathrm{d}B^n}\bigg|_{B=B_0} B_m^n \cos(\omega t)^n \tag{2.3}$$

The lock-in amplifier filters out all the components except the term $n = 1$ returning $\mathrm{d}f_L/\mathrm{d}B$. Besides the increased signal-to-noise ratio provided by the lock-in detection, the

[1]where the detector has a nicer noise figure. Typically microwave detector are characterized by a $1/\nu$ noise level.

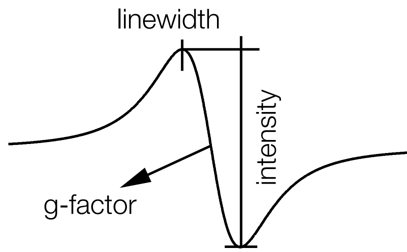

Figure 2.9: Derivative line shape as observed in EPR spectroscopy using magnetic field modulation.

visualization of the derivative of the absorption line facilitates the individuation of closely spaced lines, the evaluation of the line center and width. For this reason the majority of the EPR spectra are displayed as first derivatives, as shown in Fig. 2.9.

Low temperature measurements are performed using an Oxford ESR900 flow cryostat for operation down to liquid helium temperature. According to Curie's law, Eq. 1.108, signal intensity increases as $1/T$, making advantageous to measure at low temperature. Additionally, residual dopants in the bulk can be frozen out, reducing sample conductivity and improving the resonant cavity Q factor.
In this experimental setup, the sample is placed at the center of the cavity by use of a high purity quartz rod, with the possibility to rotate about the $(1\bar{1}0)$ axis, as shown in Fig. 2.10.

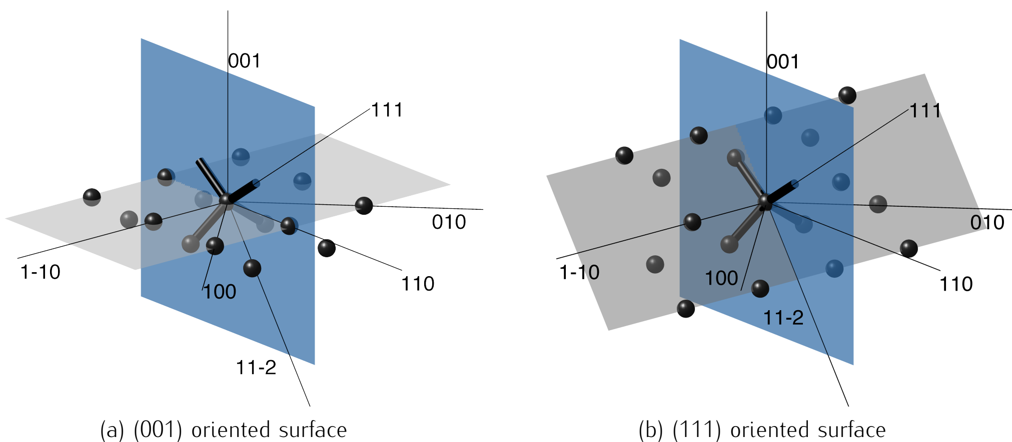

(a) (001) oriented surface (b) (111) oriented surface

Figure 2.10: Orientation of the magnetic field with respect to crystal axes and surface plane (gray) in spin resonance experiments. The magnetic field lies within the $(1\bar{1}0)$ plane (blue) and it is allowed to rotate to intersecate the main low-index directions: (001), (111), (110). The directions of the bonds in a diamod lattice belong to the $\langle 111 \rangle$ family.

Contactless Electrical Detection

EDMR spectroscopy exploits the phenomenon of the Spin Dependent Recombination (SDR) to identify the onset of the magnetic resonance through a change in the conduction properties of the sample. Significantly higher sensitivity can be achieved over conventional spin resonance spectroscopy. In contactless operation mode, a special designed cavity is

employed (electric field cavity ER4109EF by Bruker). Light with $\lambda = 450$ nm emitted by a Light Emitting Diode is shined on the sample through the optical access of the cavity. The sample is placed in a region of both microwave magnetic *and* electric field. As a consequence, spin dependent changes of the photocurrent induce a detectable change in the cavity Q factor, allowing the detection of the signal by the microwave receiver, as in conventional EPR. Experimentally, the detection of the signal in EPR and in contactless EDMR takes place in the same way, being a microwave leakage at the detector induced by change in the Q factor of the cavity in both cases. Still, the origin of the signal is intrinsically different: for conventional EPR the change in the Q factor is due to microwave absorption, while for contactless EDMR it is due to a change in energy dissipation. The instrument employed to perform EDMR experiments is a customized Varian EPR spectrometer.

2.3 Interface Trap Characterization by Admittance Spectroscopy

Chapter 1.2 described the correlation between interface trap properties and admittance in a MOS capacitor. The device response has been modeled as a distribution of isolated traps, taking into account band-bending fluctuations due to the interface charge random distribution. By fitting experimental results to the model, it is possible to extract accurate values of the density of interface traps, D_{it}, the characteristic time constant for majority carriers, τ_p or τ_n, and the variance of band-bending fluctuations, σ_S. The model provides also an order-of-magnitude estimate of the capture cross section $\sigma_{p,n}$ and indication on the donor or acceptor nature of the interface states.

The complete characterization of the traps, viz. D_{it}, τ, and σ_S as function of the energy level, necessitates admittance measurements varying both gate bias V_g and ac angular frequency ω. Information on the traps can be extracted unambiguously when the MOS is biased in depletion. However, in order to extract the interface trap properties, full scan from accumulation to inversion is required to obtain auxiliary information such as oxide capacitance, substrate doping level, and series resistance. Typically, frequency ranges from 20 Hz to 1 MHz, limiting the portion of the bandgap accessible to the admittance spectroscopy (see Eq. 1.31 in chapter 1.2 for the relation between response time and energy depth). To overcome this limitation and extend the span in energy, measurements can be repeated at different temperatures. By this mean, it is possible to exploit the strong dependence on the temperature of the characteristic time to move it into the experimentally accessible time window. Another beneficial effect comes from measuring at different temperatures. Depletion starts from flatband voltage, the condition when surface potential equals bulk potential. By lowering the temperature, the bulk potential shifts towards the majority band, extending the range of the surface potential where the MOS is operated in depletion.

Experimental setup

An Agilent E4980 LCR meter was employed in admittance measurements, placing the sample in a Lake Shore probe station designed for cryogenic operation, down to liquid helium temperature. The samples are fixed on the chuck by means of silver conductive paste, for optimal electrical and thermal contact. Temperature is regulated by an electrical

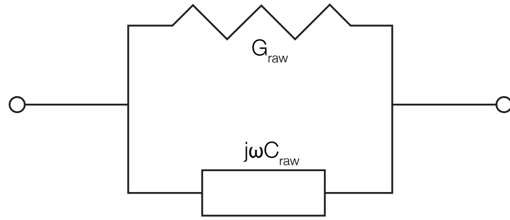

Figure 2.11: Equivalent circuit assumed by the LCR meter for the device under test, modeled in terms of capacitance C_{raw} and conductance G_{raw}.

heater operated by a Lake Shore ITC in a feedback loop with a thermocouple located in the vicinity of the sample. Probe wires are connected to the LCR meter through triaxial cables to reduce leakage currents and parasitic capacitance.

Admittance Analysis Workflow

The LCR meter measures impedance and calculates the equivalent parallel capacitance and conductance according to the equivalent circuit shown in Fig. 2.11, indicated in the following as C_{raw} and G_{raw}, respectively, to stress that pre-processing is required. In fact, the parasitic effects generated by series resistance R_s need to be corrected before proceeding with the analysis. Series resistance is an additional source of small-signal energy loss in the MOS capacitor, resulting in a smooth background affecting the conductance curve at high frequency. Especially in case of low D_{it}, the peak in the conductance *vs.* gate bias curve, $G_P(V_g)$, can be overshadowed or distorted by this background.

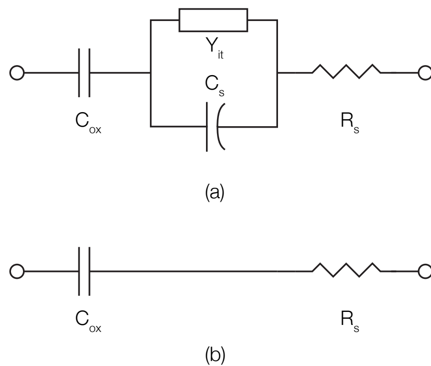

Figure 2.12: (a) MOS equivalent circuit, including parasitic series resistance R_s. Oxide capacitance C_{ox}, semiconductor capacitance C_s, and trap admittance Y_{it} are shown. The interface trap equivalent parallel conductance G_P is the real part of Y_{it}. (b) When biasing the MOS capacitor in strong accumulation, both C_s and Y_{it} are effectively short-circuited. This simplified circuit can be used to estimate C_{ox} and R_s from the admittance measured in strong accumulation.

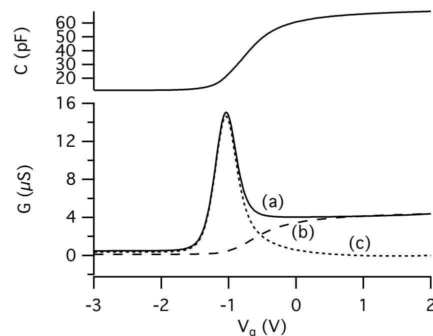

Figure 2.13: Bottom: conductance G as a function of gate bias V_g. The solid line (a) is the raw conductance, comprising the series resistance background – represented by the dashed line (b) – and the trap conductance – represented by the dotted line (c). Top: series resistance contribution to capacitance is negligible. Sample: *G1n*, T = 300 K, R_s = 23.7 Ω.

To estimate R_s it is convenient to bias the capacitor in strong accumulation, where semiconductor capacitance and trap admittance are negligible in the series circuit (see Fig. 2.12). R_s is the real part of the impedance $Z = 1/Y$ and is given by

$$R_s = \left. \frac{G_{\text{raw}}}{G_{\text{raw}}^2 + \omega^2 C_{\text{raw}}^2} \right|_{\text{accumulation}} \tag{2.4}$$

Next, C_{raw} and G_{raw} can be corrected to obtain C and G according to:

$$C = \frac{(G_{\text{raw}}^2 + \omega C_{\text{raw}}^2) C_{\text{raw}}}{\alpha^2 + \omega^2 C_{\text{raw}}^2} \tag{2.5}$$

$$G = \frac{(G_{\text{raw}}^2 + \omega C_{\text{raw}}^2) \alpha}{\alpha^2 + \omega^2 C_{\text{raw}}^2} \tag{2.6}$$

$$\text{where} \qquad \alpha = G_{\text{raw}} - (G_{\text{raw}}^2 + \omega^2 C_{\text{raw}}^2) Rs$$

Typically, R_s does not influence the measured capacitance as appreciably as it affects conductance. Care is taken to reduce R_s as much as possible by depositing a thin metal layer on sample's back surface.

Data can be rationalized better making use of the standard representation in terms of: $C - V$ plot, showing capacitance as a function of V_g; $G_P - V$ plot, showing equivalent parallel conductance as a function of V_g; $G_P/\omega - \omega$ showing equivalent parallel conductance, divided by the angular frequency, as a function of frequency. Additionally, two-dimensional maps are useful to convey the distinct behavior of G_P/ω as a function of both V_g and ω. In the following, C and G denote conductance and capacitance per unit area, obtained by dividing the capacity and the conductivity by the actual gate area. Gate areas are estimated from images taken with a camera mounted on an optical microscope with calibrated magnification.

Of paramount importance is the comparison of experimental data to ideal MOS characteristics. For this reason, Eq. 1.46 together with Eq. 1.41, 1.44, 1.45, and 1.48, describing ideal $C - V$ curves in the low high frequency limits, have been implemented in a simulation routine. According to the model, $C_{s,\text{ideal}}^{HF}$, $C_{s,\text{ideal}}^{LF}$, C_{ideal}^{HF}, C_{ideal}^{LF}, $\mathcal{E}_S$, and Q_S, are available as functions of either ψ_S and V_g. Only two parameters are required to calculate ideal curves, namely, oxide capacitance C_{ox} and bulk potential ϕ_B. Care is taken in order to obtain the best estimate of these quantities from experimental data.

A first glance to $C - V$ curves already gives indication on the magnitude of C_{ox}. In accumulation $C = (1/C_s + 1/C_{ox})^{-1} \approx C_{ox}$ when $C_s \gg C_{ox}$. Yet, this is not always the case and complications can arise when thin oxides are employed, requiring Fermi-Dirac statistics in place of Maxwell-Boltzmann statistics and quantization of carriers in the interface layer under strong accumulation. A more elaborated method to estimate C_{ox} has been developed by Kar (2003). He calculated the correction term to the high frequency capacitance C_{acc}^{HF} for a MOS in accumulation and obtained the expression

$$\frac{1}{C_{\text{acc}}^{HF}} = \frac{1}{C_{ox}} + \sqrt{\frac{1}{2\beta} \left| \frac{\mathrm{d}(1/C_{\text{acc}}^{HF})^2}{\mathrm{d}V} \right|} \tag{2.7}$$

where β is a constant. The plot of $1/C_{\text{acc}}^{HF}$ *vs* $\sqrt{\mathrm{d}/\mathrm{d}V(1/C_{\text{acc}}^{HF})^2}$ is a straight line and the intercept on the $1/C_{\text{acc}}^{HF}$ axis yields $1/C_{ox}$.

The second parameter entering in the calculation of ideal MOS curves is ϕ_B. This quantity is not experimentally accessible in a direct way. Though, when dopants can be considered fully ionized, ϕ_B is obtained from Eq. 1.34 provided doping level N_A or N_D is known. Accurate figures are very difficult to assess, and the nominal doping concentration issued from wafer manufacturer is far from being error-free. However $C-V$ curves themselves can provide an estimate of $N_{A,D}$. Doping density can be obtained from the slope $\mathrm{d}(1/C^2)\mathrm{d}V$ of the high frequency $C-V$ curve in the region around depletion and weak inversion, according to the relation (Schroder, 2006)

$$N_{A,D} = \frac{2}{q\epsilon_s}\left(\frac{\mathrm{d}}{\mathrm{d}V_g}\frac{1}{C^2}\right)^{-1} \tag{2.8}$$

Unfortunately artifacts such as $C-V$ stretch-out due to high D_{it} or due to weak fermi level pinning can introduce additional errors. Another method avoids the pitfall of $C-V$ curve distortion by resorting to a single value of capacitance measured in strong inversion. The so-called *max-min capacitance method* (Schroder, 2006) consists in calculating the strong inversion limit of the ideal high frequency MOS capacitance, for a range of substrate doping. Then, the experimental $C_{\text{strong inv}}^{HF}$ is matched on the $C_{\text{ideal}}^{HF}(N_{A,D})$ curve, yielding the estimate $N_{A,D}$. This method is very effective provided strong inversion is attained. However it must be mentioned that, in case of large $C-V$ stretch-out, strong inversion may require electric fields across the oxide beyond breakdown threshold, and can not be attained experimentally.

With the help of the ideal curves, it is possible to calculate the position of the surface potential and the band-bending as function of the gate bias applied in the experiment. First, $C_{\text{ideal}}^{HF}(\psi_S)$ is calculated. In the high frequency limit capacitance is a function of the surface potential alone because, according to Eq. 1.55, traps do not follow the ac modulation making C_{it} negligible. Therefore, it is possible to match each point of the experimental $C_{\text{exp}}^{HF}(Vg)$ curve with the corresponding point on the $C_{\text{ideal}}^{HF}(\psi_S)$ curve to obtain the $\psi_S(V_g)$ relation:

$$\psi_S(V_g) = \psi_{S,\text{ideal}}(C_{\text{ideal}}^{Hf} = C_{\text{exp}}^{HF}(V_g)) \tag{2.9}$$

The next step is to calculate the conductive component of trap admittance Y_{it} from C and G. By examining the equivalent circuit in Fig. 2.12, where $Y_{it} = \jmath\omega C_{it} + G_P$, the interface trap equivalent parallel conductance can be written as

$$\frac{\langle G_P \rangle}{\omega} = \frac{\omega C_{ox}^2 G}{G^2 + \omega^2(C_{ox} - C)^2} \tag{2.10}$$

The equivalent parallel conductance observed in the experiments can be fitted with different line shapes depending on the model assumed to describe the center responsible for the signal.

For a single level trap, G_P is given by Eq. 1.58:

$$\frac{\langle G_P \rangle}{\omega} = C_T \frac{\omega\tau}{1 + (\omega\tau)^2}$$

A distribution of single level traps is characterized by G_P of the form of Eq. 1.57:

$$\frac{G_P}{\omega} = \frac{\log\left[1 + (\omega\tau_p)^2\right]}{2\omega\tau_p}$$

Finally, when band-bending fluctuations are taken into account, the shape of the conductance peak is given by Eq. 1.65, here recalled:

$$\frac{\langle G_P \rangle}{\omega} = \frac{q^2 D_{it}}{2\xi\sqrt{2\pi\sigma_S^2}} \int_{-\infty}^{\infty} \exp\left(-\frac{\chi^2}{2\sigma_S^2}\right) \exp(-\chi) \log(1 + \xi^2 \exp 2\chi) \mathrm{d}\chi$$

where the integration variable χ represents the dimensionless fluctuation of band-bending $q/(k_B T)\,(\psi_s - \langle\psi_s\rangle)$ assumed having gaussian distribution centered about the mean band-bending $\langle\psi_s\rangle$ with FWHM $= \sigma_S$, and the dimensionless parameter ξ is a normalized frequency defined by $\xi = \omega\tau$. The position of the peak in the equivalent parallel conductance can be found using the condition $\frac{\mathrm{d}}{\mathrm{d}\xi}\left(\frac{\langle G_P\rangle}{\omega}\right) = 0$, resulting in the following implicit equation for ξ_p (Goetzberger et al., 1976)

$$\int_{-\infty}^{\infty} \exp\left(-\frac{\chi^2}{2\sigma_S^2}\right) \exp(-\chi) \left[\frac{2\xi_p^2 \exp 2\chi}{1 + \xi_p^2 \exp 2\chi} - \log(1 + \xi_p \exp 2\chi)\right] \mathrm{d}\chi = 0 \tag{2.11}$$

ξ_p for different values of σ_S is obtained by solving Eq. 2.11 numerically, the result is plotted in Fig. 2.14. The height of the equivalent parallel conductance peak is related to

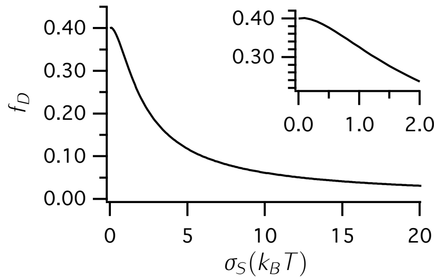

Figure 2.14: Plot of ξ_p *vs* σ_S, calculated by solving Eq. 2.11 numerically. The inset is a close up at the lower σ_S.

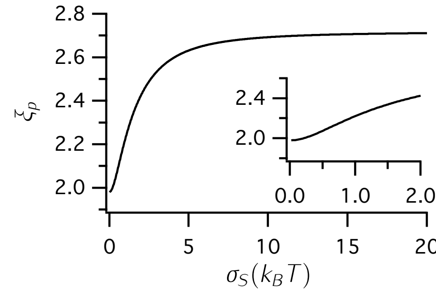

Figure 2.15: Plot of f_D *vs* σ_S, calculated by solving Eq. 2.13 numerically. The inset is a close up at the lower σ_S.

the D_{it} through

$$D_{it} = \left.\frac{\langle G_P\rangle}{\omega}\right|_{\text{peak}} \frac{1}{f_D(\sigma_S) q^2} \tag{2.12}$$

where

$$f_D(\sigma_S) = \frac{1}{2\xi_p\sqrt{2\pi\sigma_S^2}} \int_{-\infty}^{\infty} \exp\left(-\frac{\chi^2}{2\sigma_S^2}\right) \exp(-\chi) \log(1 + \xi_p^2 \exp 2\chi) \mathrm{d}\chi \tag{2.13}$$

f_D as a function of σ_S can be obtained by numerical integration of Eq. 2.13 and the result is shown in Fig. 2.15.

In order to estimate the contribution of band-bending fluctuations on the line shape, the experimental peaks have to be fitted to the model of Eq. 1.65, but the evaluation of the integral is computationally demanding. Several calls of the model function comprising the integral are performed during the fit. Then, the fitting routine is run for each value of V_g (up to $200-300$ points per experiment), for each measurement, for each sample. The execution time grows soon unacceptably. The suggestion of Nicollian et al. (1969) indicates a possible way to overcome this limitation. For a given ξ_p, the line shape of the conductance peak can be written in dimensionless units as a function of the ratio $r = \xi/\xi_p$

$$\frac{\left.\frac{\langle G_P\rangle}{\omega}\right|_{\xi=r\xi_p}}{\left.\frac{\langle G_P\rangle}{\omega}\right|_{\xi=\xi_p}} = \frac{1}{r}\frac{\int_{-\infty}^{\infty}\exp\left(-\frac{\chi^2}{2\sigma_S^2}\right)\exp(-\chi)\log(1+r^2\xi_p^2(\sigma_S)\exp 2\chi)\mathrm{d}\chi}{\int_{-\infty}^{\infty}\exp\left(-\frac{\chi^2}{2\sigma_S^2}\right)\exp(-\chi)\log(1+\xi_p^2(\sigma_S)\exp 2\chi)\mathrm{d}\chi} \tag{2.14}$$

with σ_S as the only parameter. In this formulation, the right side of Eq. 2.14 is made completely general, not related to any experimental conditions, such as temperature, absolute frequency, surface potential. The function takes only r as independent variable and σ_S as a parameter. The curve can be plotted back as a function of frequency through the relation $\omega = r\xi_p/\tau$. Following this consideration, the right side of Eq. 2.14 has been calculated numerically, once and for all, in the range $r \in \{10^{-6} - 10^{6}\}$; $\sigma_S \in \{0.2 - 20\}$ on a 1200×100 grid as shown in Fig. 2.16. This grid has been used as the basis in the fitting procedure, with a remarkable speed up of the fitting routine.

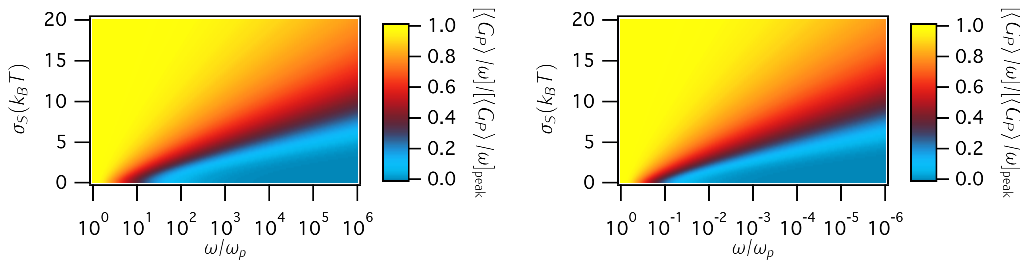

Figure 2.16: Plot of $[\langle G_P\rangle/\omega]/[\langle G_P\rangle/\omega]_{\text{peak}}$ *vs* frequency-to-peak-frequency ratio r and standard deviation of band-bending σ_S. The right plot shows frequencies higher than peak frequency ($r > 1$), while the left plot shows frequencies lower than peak frequency ($r < 1$). These plots effectively represent the line shape of the peak in equivalent parallel conductance when band-bending fluctuations are taken into account. A remarkable speed up over the standard integration of Eq. 1.65 is gained in the peak fitting procedure by using these completely general curves.

The characteristic time τ can be obtained from the peak angular frequency ω_p through the relation

$$\xi_p = \omega_p\tau \qquad \longrightarrow \qquad \tau = \xi_p/\omega_p \tag{2.15}$$

It is worth noticing that, in the limit of small band-bending fluctuations, the line shape falls back on the previous case of no fluctuations as expected. In this limit Eq. 2.12 and Eq. 2.15 still hold, with $f_D = 2.5$ and $\xi_p = 1.98$.

The peak line shape according to the three different models described above is shown in Fig. 2.17. The curves expected for a single level trap and for a continuum distribution

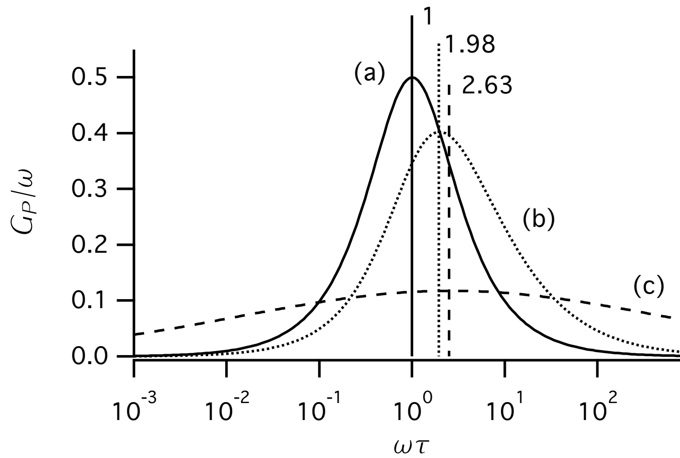

Figure 2.17: Plot of theoretical G_P/ω *vs* $\omega\tau$ curves. (a) Single level trap model, (b) continuous distribution of single level traps, and (c) continuous distribution of single traps considering band-bending fluctuations. The position of the peak is evidenced for the three curves. From line (a) to line (b) and to line (c), the peak shifts to high frequency and the height decreases. The curves have been drawn for unit trap capacitance. In curve (c) $\sigma_S = 5$.

of single level traps are qualitatively very similar, however in the first case the peak angular frequency is $\omega_p = 1/\tau$, while in the second case $\omega_p = 1.98/\tau$. The effect of band-bending fluctuations is to broaden the line, as expected, and also to shift the peak to higher frequency, according to Eq. 2.15 and Fig. 2.14: $\sigma_S = 5$ implies $\omega_p \approx 2.63/\tau$.

The density of interface states D_{it} is thus estimated by fitting the equivalent parallel conductance $G_P/\omega(\omega)$ at different values of the gate bias V_g applied to the MOS capacitor. Best results are obtained assuming a continuous distribution of single level traps, allowing for band-bending fluctuation to broaden the peak. Peak angular frequency, ω_p, peak equivalent parallel conductance, $\langle G_P \rangle /\omega|_{\omega=\omega_p}$, and band-bending fluctuation variance, σ_S, are estimated at any given V_g with least square optimization. The physical quantities of interest, D_{it} and τ, are obtained by using Eq. 2.12 and Eq. 2.15, respectively.

As pointed out in chapter 1.2, due to the properties of the occupation function f, traps respond when $E \approx \mu = q\psi_S + q\phi_B + E_i$. Therefore, by recalling the $\psi_S - V_g$ relation of Eq. 2.9, the density of interface states $D_{it}(V_g)$ is expressed as function of the energy inside the bandgap.

Moreover, provided the position of the surface potential is known with sufficient accuracy, it is possible to estimate the capture cross section of the interface traps from $\tau(V_g)$ by rewriting Eq. 1.62 and Eq. 1.63

$$\sigma_p = \frac{1}{\tau_p v^{th} N_V} \exp\left(\frac{q\phi_S - E_V}{k_B T}\right) \qquad \text{for} \quad \text{p-type}$$

$$\sigma_n = \frac{1}{\tau_n v^{th} N_C} \exp\left(\frac{E_C - q\phi_S}{k_B T}\right) \qquad \text{for} \quad \text{n-type} \tag{2.16}$$

(2.17)

Rigorously, this analysis is valid for the MOS capacitor biased in depletion and care must be taken when discussing measurements in accumulation or inversion. Moreover, even when the MOS is in depletion, it is necessary to carefully check that the equivalent parallel conductance peak is within the experimental frequency range to avoid fitting only the shoulder of the line. Otherwise the resulting extrapolated peak height would be affected by large uncertainty, reducing the accuracy of the estimated D_{it}. In addition, peaks that are largely broadened due to band-bending fluctuation will lead to large errors in τ.

The distribution of interface traps inside the bandgap obtained by the conductance method can be validated by falling back to the $C-V$ curves. When minority carrier inversion charge *and* interface traps are able to follow the ac modulation the MOS capacitance is given by

$$C^{LF} = \left(\frac{1}{C_{ox}} + \frac{1}{C_s + C_{it}} \right)^{-1} \tag{2.18}$$

By comparing the experimental $C-V$ to the ideal curve, D_{it} can be written as a function of energy, recalling Eq. 1.51

$$D_{it}(E = q\psi_S + q\phi_B + E_i) = \frac{1}{q^2} \left(\frac{C_{ox} C^{LF}(\psi_S)}{C_{ox} - C^{LF}(\psi_S)} - C^{LF}_{\text{ideal},s}(\psi_S) \right) \tag{2.19}$$

where the dependency on ψ_S is made explicit and Eq. 2.9 is used to rewrite $C(V_g)$ as $C(\psi_S)$. Eq. 2.19 is commonly referred to as the *low frequency method* or LF method (Berglund, 1966). Despite the sensitivity is not as high as in the conductance method, LF method can be applied to determine the interface trap density over the entire bandgap, provided that low enough frequency is available[2]. For this reason it is of practical use only at room temperature.

The use of the theoretical C_s can be avoided by using the experimental high frequency curve. Assuming that the interface traps do not respond to the high frequency, it is possible to write

$$C_s = \frac{C_{ox} C^{HF}}{C_{ox} - C^{HF}} \tag{2.20}$$

and substituting into Eq. 2.19 yields

$$D_{it} = \frac{C_{ox}}{q^2} \left(\frac{C^{LF}/C_{ox}}{1 - C^{LF}/C_{ox}} - \frac{C^{HF}/C_{ox}}{1 - C^{HF}/C_{ox}} \right) \tag{2.21}$$

Eq. 2.19 is commonly referred to as the *high frequency / low frequency method* or HF/LF method (Castagné and Vapaille, 1971). HF/LF method is accurate only in depletion and in weak inversion regime.

[2] or *quasi-static* $C-V$ are measured with a sufficiently slow bias sweep and gate leakage is negligible.

2.4 Bibliography

Silvia Baldovino, Alessandro Molle, and Marco Fanciulli. Evidence of dangling bond electrical activity at the Ge/oxide interface. *Applied Physics Letters*, 93(24):242105, 2008. ISSN 00036951. doi: 10.1063/1.3050451. URL http://link.aip.org/link/APPLAB/v93/i24/p242105/s1&Agg=doi.

C.N. Berglund. Surface states at steam-grown silicon-silicon dioxide interfaces. *IEEE Transactions on Electron Devices*, 13(10):701–705, October 1966. ISSN 0018-9383. doi: 10.1109/T-ED.1966.15827. URL http://ieeexplore.ieee.org/lpdocs/epic03/wrapper.htm?arnumber=1474417.

R. Castagné and A. Vapaille. Description of the SiO2-Si interface properties by means of very low frequency MOS capacitance measurements. *Surface Science*, 28(1):157–193, November 1971. ISSN 00396028. doi: 10.1016/0039-6028(71)90092-6. URL http://www.sciencedirect.com/science/article/pii/0039602871900926.

A. Goetzberger, E. Klausmann, and M. J. Schulz. Interface states on semiconductor/insulator surfaces. *C R C Critical Reviews in Solid State Sciences*, 6(1):1–43, 1976. doi: 10.1080/10408437608243548. URL http://www.tandfonline.com/doi/abs/10.1080/10408437608243548.

S. Kar. Extraction of the capacitance of ultrathin high-K gate dielectrics. *IEEE Transactions on Electron Devices*, 50(10):2112–2119, October 2003. ISSN 0018-9383. doi: 10.1109/TED.2003.817271. URL http://ieeexplore.ieee.org/lpdocs/epic03/wrapper.htm?arnumber=1232931.

Alessio Lamperti, Silvia Baldovino, Alessandro Molle, and Marco Fanciulli. Chemical Nature of the Passivation Layer Depending on the Oxidizing Agent in Gd2O3/GeO2/Ge Stacks Grown by Molecular Beam Deposition. *Microelectronic Engineering*, 88(4):403–406, April 2011. ISSN 01679317. doi: 10.1016/j.mee.2010.10.029. URL http://linkinghub.elsevier.com/retrieve/pii/S0167931710004016.

Alessandro Molle, Md. Nurul Kabir Bhuiyan, Grazia Tallarida, and Marco Fanciulli. Formation and Stability of Germanium Oxide Induced by Atomic Oxygen Exposure. *Materials Science in Semiconductor Processing*, 9(4-5):673–678, August 2006. ISSN 13698001. doi: 10.1016/j.mssp.2006.09.002. URL http://linkinghub.elsevier.com/retrieve/pii/S1369800106002125.

Alessandro Molle, Sabina Spiga, and Marco Fanciulli. Stability and interface quality of GeO2 films grown on Ge by atomic oxygen assisted deposition., July 2008. ISSN 1089-7690. URL http://www.ncbi.nlm.nih.gov/pubmed/18624462.

EH Nicollian, A Goetzberger, and AD Lopez. Expedient method of obtaining interface state properties from MIS conductance measurements. *Solid-State Electronics*, 12:937–944, 1969. URL http://www.sciencedirect.com/science/article/pii/0038110169900148.

Stefano Paleari, A. Molle, F. Accetta, A. Lamperti, E. Cianci, and M. Fanciulli. Electrically detected magnetic resonance study of the Ge dangling bonds at the Ge(111)/GeO2

interface after capping with Al2O3 layer. *Applied Surface Science*, 291:3–5, February 2014. ISSN 01694332. doi: 10.1016/j.apsusc.2013.09.121. URL http://www.sciencedirect.com/science/article/pii/S0169433213017625.

D.K. Schroder. *Semiconductor Material and Device Characterization*. Wiley, 2006. ISBN 9780471749080. URL http://books.google.it/books?id=OX2cHKJWCKgC.

Ruilong Xie and Chunxiang Zhu. Effects of Sulfur Passivation on Germanium MOS Capacitors With HfON Gate Dielectric. *IEEE Electron Device Letters*, 28(11):976–979, November 2007. ISSN 0741-3106. doi: 10.1109/LED.2007.907415. URL http://ieeexplore.ieee.org/lpdocs/epic03/wrapper.htm?arnumber=4367577.

Electron Spin Resonance Spectroscopy 3

Following the description of the physical principles governing the electron spin resonance phenomena, illustrated in chapter 1.3, and the setup employed to perform electron spin resonance experiments, detailed in chapter 2.2, the outcomes of the investigation of different germanium interfaces with oxides are shown below. To introduce to the subject, the case of the (001)Ge/GeO_2 interface is briefly reviewed starting from the literature. Afterward, the original results obtained in the study of the (111)Ge/GeO_2 interface are presented. Then, the measurements on the Ge/GeO_2/Al_2O_3 stack are discussed due to the relevance to the subsequent admittance spectroscopy characterization, which will be the topic of the next chapter.

3.1 (001)Ge/GeO_2

The first evidence of paramagnetic centers showing electron trapping activity at the germanium-oxide interface revealed by contactless EDMR spectroscopy has been found in (001) oriented Ge/GeO_2 samples (Baldovino et al., 2008). At first, three signals have been identified, as the minimum number of component required to have a satisfactory fit to the data shown in Fig 3.1. A common behavior is recognized upon variation of temperature (see Fig 3.2), magnetic field modulation frequency, and light intensity. The three components of the signal scale in intensity as a whole and the overall shape of the spectrum remains unchanged, establishing a strong argument in support of the attribution of the signal to a common origin.

By rotating the static magnetic field in a $(1\bar{1}0)$ plane, the g-factor revealed an anisotropy, shown in Fig. 3.1, that can not be consistent with a paramagnetic center located into the bulk amorphous oxide. Indeed, the spatial order is typically lost in amorphous materials where all orientations are equivalent. It can be noticed that no clear indication of the underlying symmetry of the center can be determined from the angular map and, even at high symmetry directions, the three lines do not coincide in position. Therefore, it needs to be supposed a symmetry lower than trigonal, either triclinic or monoclinic.

The same signal is observed also when the oxidizing agent is changed. Fig. 3.4 compares the EDMR spectra when atomic oxygen (AO), molecular oxygen (O_2), and ozone (O_3) are used. Native oxide, also, shows the same spectral features (not shown) (Baldovino et al., 2008). The g-factor of the three components is slightly influenced by the oxidizing agent,

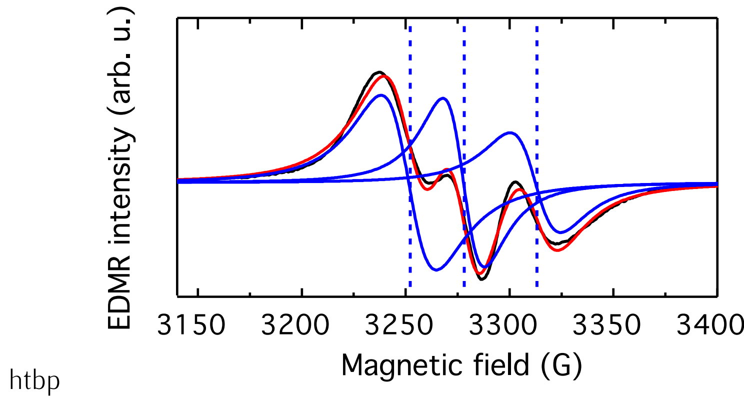

htbp

Figure 3.1: EDMR spectrum observed at the Ge/GeO_2 interface. The fitted curve (red) reproduce convincingly the experimental spectrum (black). The three components assumed for the fit are shown separately (blue). The signals are attributed to the Ge DB, after Baldovino et al. (2010). Experimental condition: microwave frequency 9.2 GHz, temperature 7 K, static magnetic field along [110].

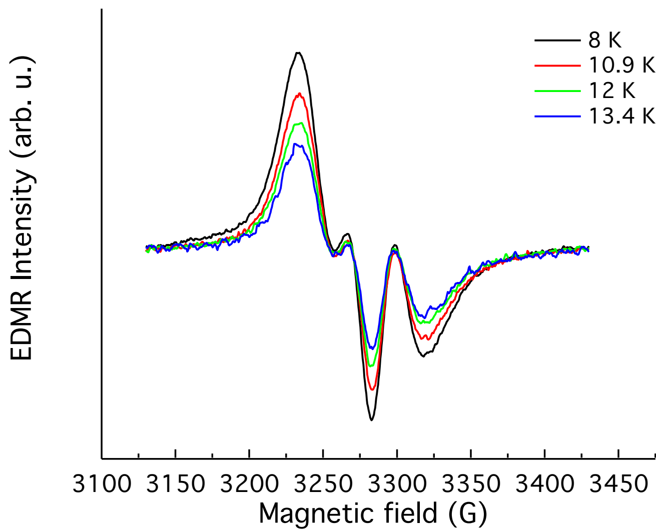

Figure 3.2: EDMR spectrum observed at the Ge/GeO_2 interface at different temperatures. The shape of the spectra does not change with temperature, only intensity scales as $1/T$. This evidence supports the attribution of the three lines shown in Fig. 3.1 to the same center. Experimental condition: microwave frequency 9.2 GHz, static magnetic field along [110].

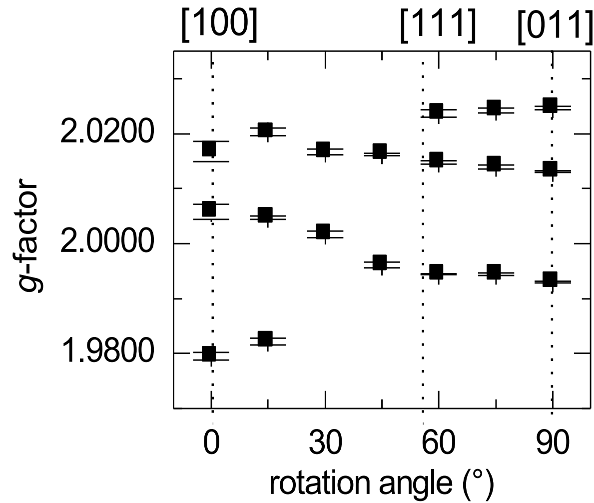

Figure 3.3: Angular dependence of the signals observed at the Ge/GeO_2 interface, as a function of magnetic field orientation with respect to sample normal. High symmetry crystal direction are indicated. The anisotropy of the g-factor excludes the origin of the signal from the amorphous oxide layer, after Baldovino et al. (2008). Experimental condition: microwave frequency 9.2 GHz, temperature 7 K, static magnetic field rotated in the $(1\bar{1}0)$ plane.

demonstrating a sensitivity to the oxide layer that would be impossible for a center located in the bulk of the semiconductor. Therefore, ruled out the location within the oxide by the anisotropy, the origin of the signal must be at the interface.
The clue for signal identification stems from the analogy with a well established system: the silicon-silicon dioxide interface. Following the early work by Lebib et al. (1997) on porous SiGe/$SiGeO_2$ interface, the resonance features of the EDMR signal observed in Ge/GeO_2 are compared to the characteristic of the EPR spectrum of the silicon dangling bond (DB), that is the prominent paramagnetic defect found at the Si-oxide interface. An extended discussion of the properties and the spectroscopy of the Si DB is demanded to chapter 5.1. In detail, the amount of the extremal g shift from the free electron value (indicated as δg) is connected to the spin-orbit constant λ (see Eq. 1.80). The reasonable agreement between the two ratios $\delta g(\mathrm{Ge/GeO_2})/\delta g(\mathrm{Si/SiO_2})$ and $\lambda_{\mathrm{Ge}}/\lambda_{\mathrm{Si}} = 940\,\mathrm{cm}^{-1}/142\,\mathrm{cm}^{-1}$ hints at the role of Ge DB in the EDMR signal (Lebib et al., 1997; Stesmans and Afanas'ev, 1998; Stesmans et al., 2009). Other defects are excluded on the basis of the observed g-factors. Thermal donors (TDs), paramagnetic impurities (phosphorus, arsenic, antimony and bismuth), band tail states and conduction electrons have been considered and the corresponding g-factors are shown in Tab. 3.1. The values and the rotational symmetry of the signals observed at the Ge/GeO_2 interface are not consistent with any of the characteristics in the table. Then, the attribution to the DB of the three component signal observed at the (001)Ge/GeO_2 interface is solid and confirmed by several works. It is scarcely affected by thermal treatment as low temperature post-deposition-anneal as reported by Molle et al. (2011). Additional capping of the ger-

interface	g_{min}	g_{max}	Ref.
(001)Si/SiO_2	2.0022	2.00735	(Stesmans and Afanas'ev, 1998)
(001)Ge/GeO_2	1.992	2.024	(Baldovino et al., 2008)

Table 3.1: Extremal g-factors measured by electron spin resonance spectroscopies at Si/SiO_2 and Ge/GeO_2 interfaces. In the case of high temperature oxidized (001)Si/SiO_2, are indicated the principal values g_2, g_3 of the P_{b1} center (see chapter 5.1 and reference therein for additional details). In the case of Ge/GeO_2, only upper and lower bounds for the principal values can be given, as the underlying symmetry is not identifiable.

	$g_{//}$	$g_{\perp}$	symmetry	Ref.
TDs	0.849	1.917	orthorombic-I	(Callens et al., 1989)
P (donor)	1.563	1.563	isotropic	(Wilson, 1964)
As (donor)	1.570	1.570	isotropic	(Wilson, 1964)
Bi (donor)	1.567	1.567	isotropic	(Wilson, 1964)
band tail state electrons	2.01	2.01	isotropic	(Marques et al., 1999)
band tail state holes	2.03	2.03	isotropic	(Marques et al., 1999)
conduction electrons	0.83	1.917	trigonal	(Hale et al., 1975)

Table 3.2: g-factor and symmetry of known paramagnetic centers in Ge.

manium oxide with insulator layers does not alter the structure of the defect (Baldovino et al., 2012). The oxidizing agent, as anticipated, influences the spectrum only marginally. The slight variation is attributed to the different stress at the interface resulting from the different oxidation process (Baldovino et al., 2008; Molle et al., 2008).

The AO oxidation results in a additional signal, which, however, displays a different behavior and therefore a different nature. In particular, the line is narrower than the DB and a different angular dependence is observed, as shown in Fig. 3.5. This defect is almost isotropic and it is therefore natural to locate it in the oxide side of the interface and call it *oxide related defect* (OD). The intensity of the signal indicates a higher density of these defects, with respect to the dangling bonds. A purely isotropic line attributed to the same OD is observed using standard EPR technique. Indeed, EPR is less sensitive than EDMR but it probes the whole volume of the sample. Being not specifically sensitive to the illuminated semiconductor interface, EPR then reflects an average over all the possible location of the OD, with a prevailing contribution from the amorphous bulk oxide.
Additionally the dependence on light intensity shows that the intensity of the new signal grows steadily for increasing light flux (in the 10^{15} photons/s range) while the first three signals show saturation (see Fig. 3.6). A connection has been established with GeO_x content (sub-stoichiometric germanium oxide) and the OD signal (Baldovino et al., 2008, 2010; Lamperti et al., 2011; Baldovino et al., 2012), observed also when different oxides are grown on the Ge surface (Molle et al., 2011).
Since a EDMR signal is observed, the location of the OD signal in close proximity of the semiconductor necessarily results in defect levels in the bandgap. Admittance spectroscopy evidenced a correlation between the OD signal and increased D_{it} at midgap (Baldovino et al., 2010).

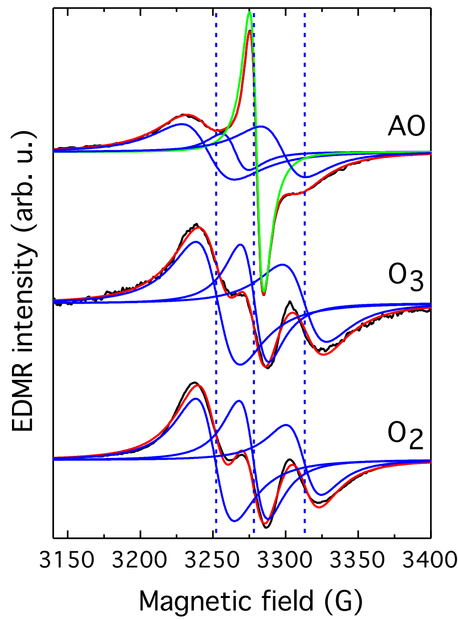

Figure 3.4: EDMR spectra observed at the Ge/GeO_2 interface exposed to atomic oxygen (AO), molecular oxygen (O_2), and ozone (O_3) oxidation, respectively. The three signals of the Ge DB (blue) are always present, while AO shows an additional component. The g-factor of the three components is influenced by the oxidizing agent, even though to a limited extent not appreciable in the graph. Ruled out the location within the oxide by the anisotropy, the origin of the signal must be at the interface. After Baldovino et al. (2010). Experimental condition: microwave frequency 9.2 GHz, temperature 7 K, static magnetic field along [110].

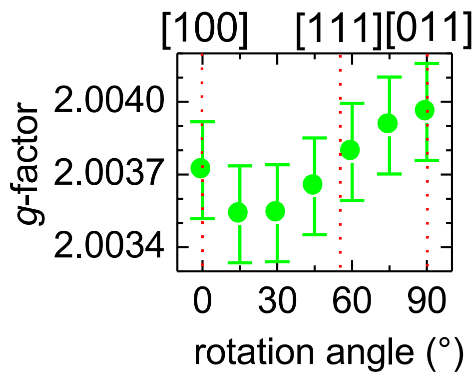

Figure 3.5: Angular dependence of the OD line as a function of magnetic field orientation with respect to sample normal (see Fig. 3.5, green line). High symmetry crystal direction are indicated. The almost isotropic behavior reflects a location of the center more within the amorphous oxide. After Baldovino et al. (2008). Experimental condition: microwave frequency 9.2 GHz, temperature 7 K, static magnetic field along [110].

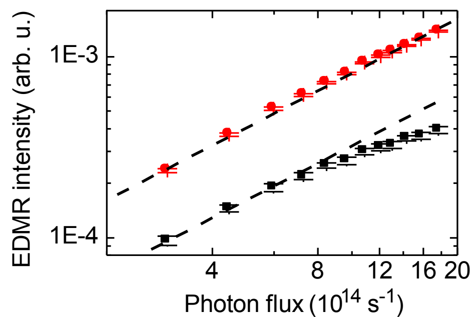

Figure 3.6: Intensity of the OD line (red) and the Ge DB lines (black) as a function of light intensity. The different behavior reflects the distinct origin of the signals. After Baldovino et al. (2008). Experimental condition: microwave frequency 9.2 GHz, temperature 7 K, static magnetic field along [110].

3.2 (111)Ge/GeO_2

Following the identification of the Ge DB at the (001) Ge interface, it was natural to direct EDMR spectroscopy to the study of the (111) counterpart, which has even more importance for the implementation of novel electronic devices, possessing the highest mobility (Kuzum et al., 2009). The proceeding of this section reports on the published paper (Paleari et al., 2013) about the investigation of the (111)Ge/GeO_2 interface.

The first measurements started from the *H1u* sample, at the temperature of 5 K, with a microwave frequency of about 9.2 GHz, and a 7 kHz magnetic field modulation of sufficiently low amplitude to avoid signal distortion. Blue light illumination is used to photo-generate carriers. By observing the EDMR spectrum recorded with the external magnetic field **B** oriented along the $[11\bar{2}]$ direction, two signals are identified clearly (see Fig. 3.7). By studying the behavior of the signal as a function of the experimental

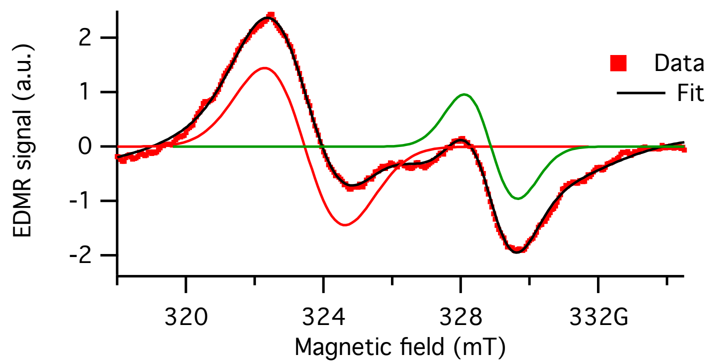

Figure 3.7: Derivative EDMR spectrum of sample *H1u*. Data are fitted with two Voigt lines. The black line is the sum of the two components and a 2nd order polynomial background.

parameters, such as modulation frequency and microwave power, it is observed a strong correlation of the two signals (see Fig. 3.8).

Fig. 3.9 (a) shows a collection of the spectra recorded at different magnetic field orientations with respect to the sample crystal axis. Best fits of representative spectra are shown in (b) and (c). As the **B** field was rotated in the $(1\bar{1}0)$ plane a distinct pattern was observed. Each spectrum was fitted with the minimal number of Voigt lines, from which the resonant field and the linewidth of the single components were extracted.

Figure 3.10 shows the g-matrix roadmap, as extracted from the deconvolution of the EDMR spectra of Fig. 3.9. A well defined pattern is present, allowing the identification

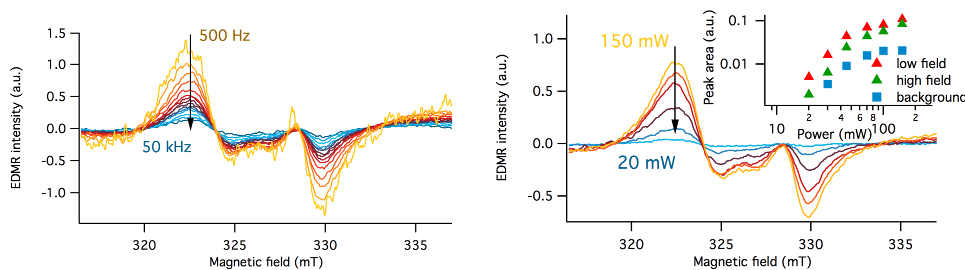

Figure 3.8: Derivative EDMR signal as a function of modulation frequency (left) and microwave power (right). The intensity of the two signals is strongly correlated, indicating a common nature.

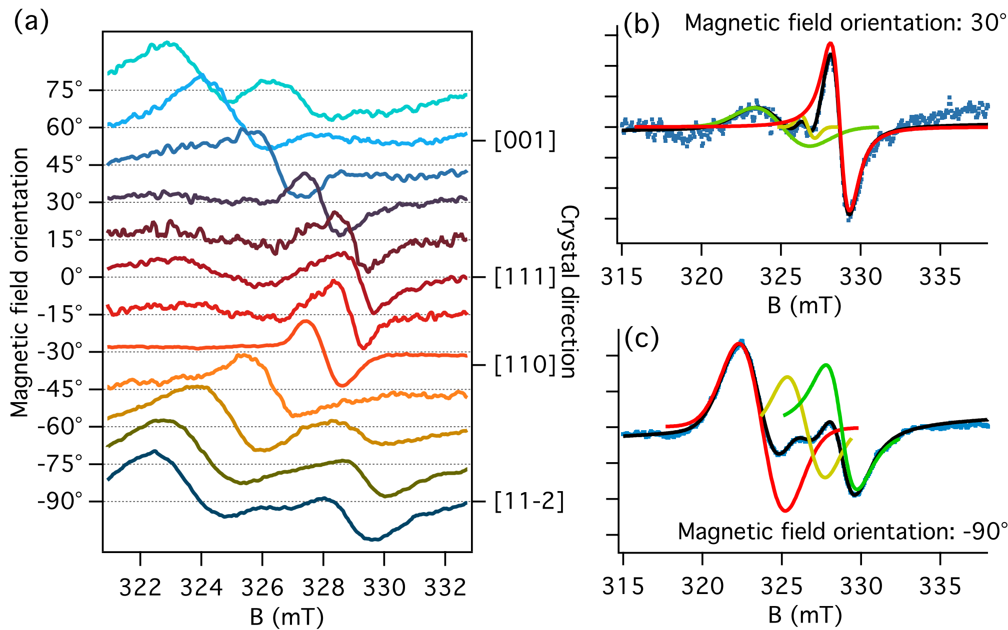

Figure 3.9: (a) Angular dependence of derivative EDMR spectra of the (111)Ge/GeO_2 sample. The vector **B** lies in the $(1\bar{1}0)$ plane and the angle is referred to the surface normal (see Fig. 2.10b). After a second-order polynomial background subtraction, the various spectra have been rescaled in the abscissa to account for the small differences in microwave frequency and normalized in intensity, for a better visual comparison. (b) and (c) Best fit of representative spectra, with an angle between the magnetic field and the surface normal of 30° and 90°, respectively. The experimental points are the blue dots and the fitted spectra are the black lines. The deconvolution of the different branches, namely the surface normal [111] (red line) and the other $\langle 111 \rangle$ branches (yellow and green lines), is evidenced.

of the main directions and principal g-values. Considering the degeneracy expected for an axial center oriented along the $\langle 111 \rangle$ direction within the Ge lattice, the most intense branch of the g pattern is associated with those centers having the symmetry axis parallel to the Ge surface normal [111], depicted in red in Fig. 3.10. This finding is in line with EPR data of defects at the Si(111)/SiO_2 interface Stesmans (1986) and it is consistent with defects located at the Ge(111)/oxide interface. Each branch can be fitted by Eq. 1.86, $g = \sqrt{g_{//}^2 \cos^2\theta + g_\perp^2 \sin^2\theta}$, where θ is the angle between **B** and the paramagnetic center axis. The experimental data reported in Fig. 3.10 are consistent with a C_{3v} point symmetry, and $g_{//} = 1.9890 \pm 0.0004$, $g_\perp = 2.0230 \pm 0.0004$ with the principal axis oriented along the $\langle 111 \rangle$ direction.

Following the same argument that helped the identification of the DB at the (001) interface, it is found that also in this case the g-factor principal values strongly support the assignment to an interfacial Ge DB (Stesmans, 1986; Lebib et al., 1997; Stesmans and Afanas'ev, 1998; Stesmans et al., 2009). Starting from a comparison with the well known P_b center at the Si(111)/SiO_2 interface, where simple first order spin-orbit (SO) theory predicts $g_\perp - g_e \propto \lambda$ (g_e is the free electron value and λ is the SO coupling constant,

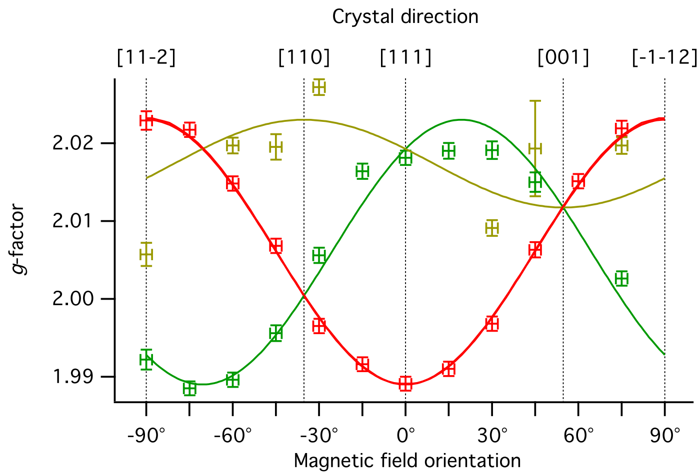

Figure 3.10: Angular g map of GeO_2/Ge(111) DB observed by contactless EDMR technique at 9.2 GHz and 5 K for **B** rotating in the $(1\bar{1}0)$ plane. The solid curves represent the best fitting of each branch to a trigonal symmetry in center in a Ge (diamond) crystal, yielding the principal g values $g_{//} = 1.9890 \pm 0.0004$, $g_{\perp} = 2.0230 \pm 0.0004$. The branches are color coded as in Fig. 3.9.

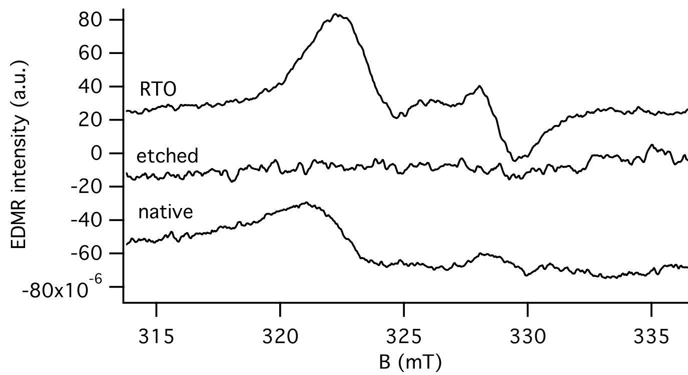

Figure 3.11: Derivative EDMR spectra of as grown thermal GeO_2 (top), after deionized water etched surface (middle), and after native oxide regrowth (bottom). Sample *H1u*, **B**$[11\bar{2}]$.

see Eq. 1.80), it can be noticed that

$$\frac{[g_{\perp} - g_e]^{\text{Ge DB}}}{[g_{\perp} - g_e]^{\text{Si } P_{b0}}} \approx \frac{\lambda^{\text{Ge}}}{\lambda^{\text{Si}}} = \frac{940\,\text{cm}^{-1}}{142\,\text{cm}^{-1}} \tag{3.1}$$

The interfacial nature of the observed DB is further evidenced by the complete suppression of the signal upon etching of the GeO_2 layer in deionized water. Following the etching procedure, for short exposure to air, when the native oxide had not enough time to grow, the signal is absent while it is recovered for longer exposures to air (see Fig. 3.11). As the strong anisotropy rules out the location inside the amorphous oxide matrix, the center must be placed at the interface.

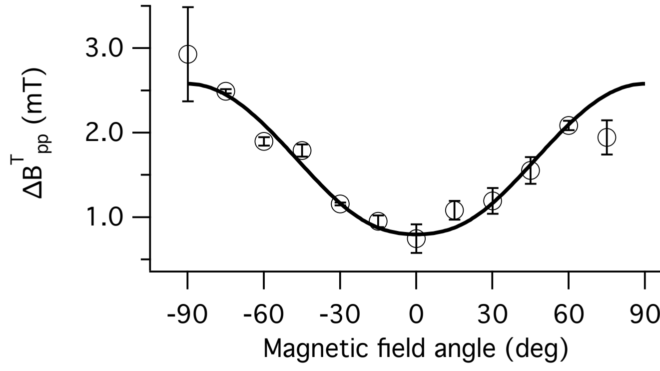

Figure 3.12: EDMR peak-to-peak line width ΔB^T_{pp} of the [111] DB as function of the angle between **B** and the paramagnetic center principal axis. The solid line represents a fit based on Eq. 3.3, from which the value $\sigma_{g_\perp} = 0.0066 \pm 0.0002$ is deduced.

An additional observation in support of the interfacial DB assignment is the inhomogeneous line broadening shown in Fig. 3.12, resulting from a strain induced spread $\sigma g(\theta)$, observed mainly in $g_\perp$, as for the case of the Si/oxide interface. The standard deviation of σg can be characterized by extracting the width $\Delta B^G_{pp}(\theta)$ of the Gaussian line broadening from the total width $\Delta B^T_{pp}(\theta)$ of a Voigt function Stesmans and Afanas'ev (1998):

$$\Delta B^T_{pp}(\theta) = 1/2\Delta B^L_{pp} + \sqrt{[\Delta B^G_{pp}(\theta)]^2 + 1/4(\Delta B^L_{pp})^2} \tag{3.2}$$

where $\Delta B^T_{pp}(\theta = 0)$ is taken as the homogeneous Lorentzian width ΔB^L_{pp}, assumed to be independent of θ. σg can then be obtained fitting $\Delta B^G_{pp}(\theta)$ using the formula:

$$\Delta B^G_{pp}(\theta) = (2h\nu/g^3\mu_B)(g_{//}\cos^2\theta\,\sigma_{g_{//}} + g_\perp \sin^2\theta\,\sigma_{g_\perp}) \tag{3.3}$$

Fit to the data yields $\sigma_{g_\perp} = 0.0066 \pm 0.0002$, again approximately $\lambda_{Ge}/\lambda_{Si}$ times larger than the value observed for Si P_b ($\sigma_{g_\perp} \approx 0.00085$) Stesmans and Afanas'ev (1998). This result is also in good agreement with previous measurements on the Ge DB at the Si_xGe_{1-x}/SiO_2 interface giving $\sigma_{g_\perp} \approx 0.0074$ Stesmans et al. (2009).

These experimental evidences open the way to a broad variety of questions, starting from the physical reason behind the impossibility to reveal the DB by conventional EPR to the detailed electrical properties of this center such as the level positioning inside the bandgap. It is, therefore, necessary to move to different characterization techniques and, in particular, to admittance spectroscopy. The jump is substantial and the technical requirements on the samples are very diverse. Admittance spectroscopy requires robust oxides that can withstand intense field ensuring low leakage currents. GeO_2 alone can not meet these specifications, but adding a thin Al_2O_3 film is sufficient to guarantee successful admittance measurements. The last open point is the effect of the additional capping on the properties of the Ge DB.

3.3 Toward Electrical Characterization: $Ge/GeO_2/Al_2O_3$

The preliminary characterization by ToF-SIMS (discussed in the previous chapter) suggest that the interface between Ge and GeO_2 is not affected by the deposition of the alumina

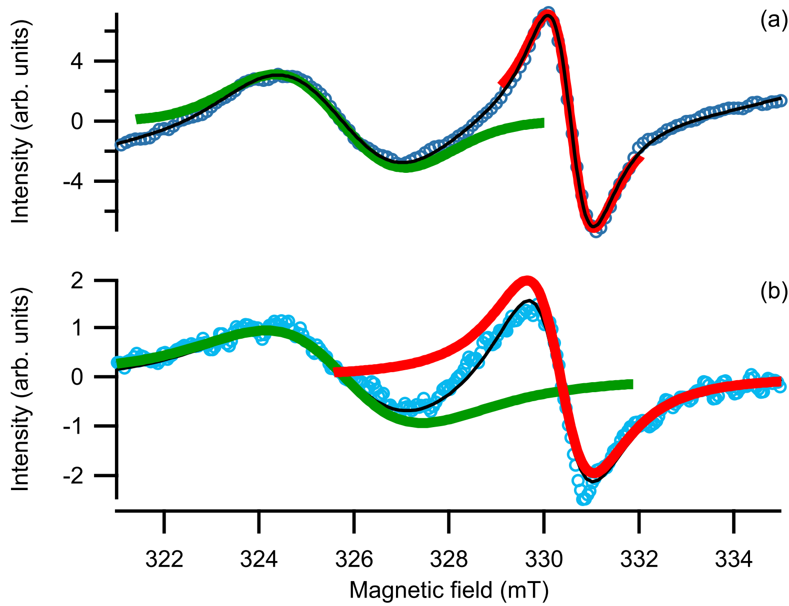

Figure 3.13: First derivative EDMR spectra of (a) sample *G1u* and (b) sample *H1u*. Data are fitted with two Voigt lines. The black line is the sum of the two components and a second order polynomial background. The high field line (red) corresponds to the [111] oriented DBs, while the low field line (green) is attributed to the DBs which are oriented along the other ⟨111⟩, forming an angle of 19° with respect to the surface plane. The two spectra are very similar in terms of g-factor and linewidth.

capping. A detailed account is given on the basis of the published paper (Paleari et al., 2014) reporting on the of the Ge/GeO_2/Al_2O_3 gate stack by EDMR.
EDMR results concur with ToF-SIMS and, as Fig. 3.13 indicates, the spectrum of sample *G1u* closely resembles the spectrum of sample *H1u*. The close similarity in the EDMR spectra between the two samples is further confirmed by scanning the orientation of the magnetic field in a (110) plane. The resulting g-factor pattern is plotted in Fig. 3.14 (dark triangles) and it turns out to be consistent with the reference Ge/GeO_2 data (light squares) for either the main branch (red) and the secondary branch (green). The last branch (yellow), which is predicted for the DBs lying outside the (110) plane, is not clearly resolved in the spectra. This line is expected to be, in general, broader than the others for two reasons. First, in the chosen experimental set-up, the angle formed with the external magnetic field is always close to 90° (see the discussion on strain induced broadening, further in the text). Second, small deviations from ideal sample orientation can split the two otherwise degenerate components, resulting in a broader line. According to the latter argument, three observations support the initial guess on the attribution of the two signals in Fig. 3.13 as follows. 1) The main branch is oriented along the [111] direction. 2) Another branch is present and is shifted from the first by $\approx 71°$. 3) Only a single line is observed when B is oriented parallel to the [001] direction. Therefore, the structure of the DBs at the Ge/GeO2 interface is not affected by the Al_2O_3 overlay and the trigonal symmetry is preserved. The same axial model of Eq. 1.80 is employed to fit the angular roadmap of Fig. 3.14. The principal values of the g-factor resulting from the fitting of the angular map with a trigonal model are gathered into Table 3.3.

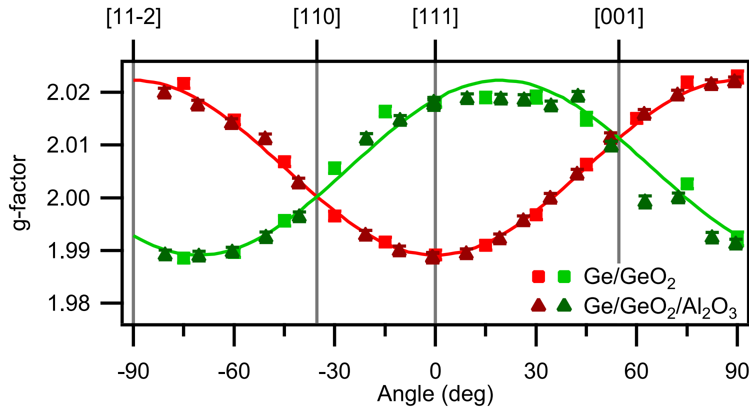

Figure 3.14: g-factor as a function of the orientation of the magnetic field in the $(1\bar{1}0)$ plane. Sample *G1u* (dark triangles) and sample *H1u* (light squares) display the same rotational pattern. A single fit to the data (solid line) reproduces the experimental points of both samples. The different branches are color coded as in Fig. 3.13.

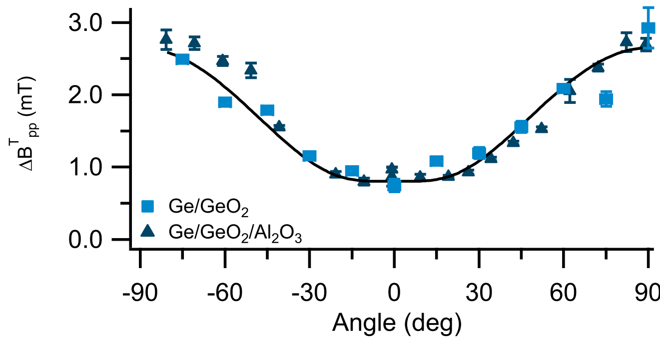

Figure 3.15: Strain induced line broadening in samples *G1u* (dark blue) and *H1u* (light blue). The angular dependence of the peak-to-peak line width ΔB^T_{pp} of the [111] DB is related to the strain induced disorder at the oxide interface. Fit to the data (line) yields $\sigma_{g\perp} = 0.0066 \pm 0.0001$. Sample *G1u* does not show evidences of additional interface disorder induced by the Al_2O_3 capping layer.

Lastly, the strain distribution at the Ge/GeO_2 interface has been investigated by following the variation of the line width of the main branch as a function of the magnetic field orientation. As in sample *H1u*, the larger width observed when **B** is at right angle with the DB principal direction is consistent with the presence of a distribution in the position of the atoms and in the bond angles. Fig. 3.15 shows that the data of sample *G1u* are in excellent agreement with *H1u* points and both fit nicely in the model developed by Brower (1986).

In conclusion, Al_2O_3 has been successfully integrated on top of the GeO_2 preserving the physical quality and the microstructure of the DB at the interface. Therefore, *G* series samples can be considered equivalent to the *H* series samples and they can be used effectively in admittance spectroscopy experiments.

Sample	$g_{//}$	$g_{\perp}$	$\sigma_{g_{\perp}}$
G1u	1.9889(4)	2.0223(4)	0.0066(1)
H1u	1.9889(6)	2.0230(7)	0.0066(2)
(001)Ge/GeO_2	1.9922(3)	2.0238(3)	//

Table 3.3: Principal values of the g matrix and strain induced broadening in samples *G1u*, *H1u*. g-factor extremal values of the (001)Ge DB are shown for comparison (Baldovino et al., 2008).

3.4 Bibliography

Silvia Baldovino, Alessandro Molle, and Marco Fanciulli. Evidence of dangling bond electrical activity at the Ge/oxide interface. *Applied Physics Letters*, 93(24):242105, 2008. ISSN 00036951. doi: 10.1063/1.3050451. URL http://link.aip.org/link/APPLAB/v93/i24/p242105/s1&Agg=doi.

Silvia Baldovino, Alessandro Molle, and Marco Fanciulli. Influence of the oxidizing species on the Ge dangling bonds at the (100)Ge/GeO2 interface. *Applied Physics Letters*, 96 (22):222110, 2010. ISSN 00036951. doi: 10.1063/1.3446839. URL http://link.aip.org/link/APPLAB/v96/i22/p222110/s1&Agg=doi.

Silvia Baldovino, Alessio Lamperti, Marco Fanciulli, and Alessandro Molle. Role of the Oxygen Content in the GeO2 Passivation of Ge Substrates as a Function of the Oxidizer. *Journal of The Electrochemical Society*, 159(6):H555, 2012. ISSN 00134651. doi: 10.1149/2.031206jes. URL http://jes.ecsdl.org/cgi/doi/10.1149/2.031206jes.

K. L. Brower. Strain Broadening of the Dangling-Bond Resonance at the (111)Si-SiO2 Interface. *Physical Review B*, 33(7):4471, 1986. URL http://prb.aps.org/abstract/PRB/v33/i7/p4471_1.

F. Callens, P. Clauws, P. Matthys, E. Boesman, and J. Vennik. Electron paramagnetic resonance of thermal donors in germanium. *Physical Review B*, 39(15):11175–11178, May 1989. ISSN 0163-1829. doi: 10.1103/PhysRevB.39.11175. URL http://link.aps.org/doi/10.1103/PhysRevB.39.11175.

Edward B Hale, John R Dennis, and Shih-Hua Pan. Strain effects on the ESR spectrum from antimony donors in germanium. *Physical Review B*, 12(7):2553–2561, October 1975. ISSN 0556-2805. doi: 10.1103/PhysRevB.12.2553. URL http://link.aps.org/doi/10.1103/PhysRevB.12.2553.

Duygu Kuzum, Abhijit J Pethe, Tejas Krishnamohan, and Krishna C Saraswat. Ge (100) and (111) N- and P-FETs With High Mobility and Low-T Mobility Characterization. *IEEE Transaction on Electron Devices*, 56(4):648–655, 2009.

Alessio Lamperti, Silvia Baldovino, Alessandro Molle, and Marco Fanciulli. Chemical Nature of the Passivation Layer Depending on the Oxidizing Agent in Gd2O3/GeO2/Ge Stacks Grown by Molecular Beam Deposition. *Microelectronic Engineering*, 88(4): 403–406, April 2011. ISSN 01679317. doi: 10.1016/j.mee.2010.10.029. URL http://linkinghub.elsevier.com/retrieve/pii/S0167931710004016.

S. Lebib, M. Schoisswohl, J. L. Cantin, and H. J. von Bardeleben. SiGe/SiGeO2 interface defects. *Thin Solid Films*, 294:242–245, 1997.

F. C. Marques, M. M. de Lima, and P. C. Taylor. Light-induced electron spin resonance in amorphous hydrogenated germanium. *Applied Physics Letters*, 74(25):3797, June 1999. ISSN 00036951. doi: 10.1063/1.124183. URL http://scitation.aip.org/content/aip/journal/apl/74/25/10.1063/1.124183.

Alessandro Molle, Sabina Spiga, and Marco Fanciulli. Stability and interface quality of GeO2 films grown on Ge by atomic oxygen assisted deposition., July 2008. ISSN 1089-7690. URL http://www.ncbi.nlm.nih.gov/pubmed/18624462.

Alessandro Molle, Silvia Baldovino, Marco Fanciulli, Dimitra Tsoutsou, Evangelos Golias, and Athanasios Dimoulas. Impact of post deposition annealing in the electrically active traps at the interface between Ge(001) substrates and LaGeOx films grown by molecular beam deposition. *Journal of Applied Physics*, 110(8):084504, October 2011. ISSN 00218979. doi: 10.1063/1.3651400. URL http://scitation.aip.org/content/aip/journal/jap/110/8/10.1063/1.3651400http://link.aip.org/link/JAPIAU/v110/i8/p084504/s1&Agg=doi.

Stefano Paleari, Silvia Baldovino, Alessandro Molle, and Marco Fanciulli. Evidence of Trigonal Dangling Bonds at the Ge(111)/Oxide Interface by Electrically Detected Magnetic Resonance. *Physical Review Letters*, 110(20):206101, May 2013. ISSN 0031-9007. doi: 10.1103/PhysRevLett.110.206101. URL http://link.aps.org/doi/10.1103/PhysRevLett.110.206101.

Stefano Paleari, A. Molle, F. Accetta, A. Lamperti, E. Cianci, and M. Fanciulli. Electrically detected magnetic resonance study of the Ge dangling bonds at the Ge(111)/GeO2 interface after capping with Al2O3 layer. *Applied Surface Science*, 291:3–5, February 2014. ISSN 01694332. doi: 10.1016/j.apsusc.2013.09.121. URL http://www.sciencedirect.com/science/article/pii/S0169433213017625.

A Stesmans and Valery V. Afanas'ev. Electron spin resonance features of interface defects. *Journal of Applied Physics*, 83(5):2449–2457, 1998.

A. Stesmans, P. Somers, and Valery V. Afanas'ev. Nontrigonal Ge dangling bond interface defect in condensation-grown (100)Si1-xGex/SiO2. *Physical Review B*, 79(19):195301, May 2009. ISSN 1098-0121. doi: 10.1103/PhysRevB.79.195301. URL http://link.aps.org/doi/10.1103/PhysRevB.79.195301.

Andre Stesmans. Electron spin resonance of [1-11],[-111], and [11-1] oriented dangling orbital Pb0 defects at the (111) Si/SiO2 interface. *Applied Physics Letters*, 48(15):972–974, 1986.

D. K. Wilson. Electron Spin Resonance Experiments on Shallow Donors in Germanium. *Physical Review*, 134(1A):A265, 1964.

Admittance Spectroscopy 4

In this chapter are discussed the outcomes of the admittance characterization of the Ge/GeO_2 and Ge/Al_2O_3 interfaces, of both (001) and (111) orientation. *p*- and *n*-type substrate are employed in order to investigate the VB side and the CB side of the bandgap with the same accuracy. The measurements and the analysis is discussed in greatest depth for the first sample, *G0p*.

4.1 *p*-type (001)$Ge/GeO_2/Al_2O_3$

According to the methodology presented in chapter 2.3, R_s is calculated and its contribution is removed from the admittance of sample *G0p*. In all experimental conditions, ranging from room to low temperatures ($300-108$ K), R_s is low, typically $17-23\,\Omega$.

Capacitance-Voltage Curves

A first glance to low frequency $C-V$ curves, shown in Fig. 4.1, already provides indication on the quality of the interface. In accumulation regime, observed at $V_g \lesssim -2$ V, there is little dispersion among the different curves, both in terms of rigid shift along the voltage axis and vertical displacement, as expected for a low density of traps. In depletion and weak inversion regime, on the other hand, D_{it} of the order of 10^{12} eV^{-1}cm^{-2} can contribute appreciably to the capacitance and are revealed by the dispersion in the $C-V$ at different temperatures. In fact, the frequency of the ac component need to be sufficiently low to allow thermal equilibrium between traps and free carriers. At high temperatures capture and emission times are shorter (as predicted by Eq. 1.31), resulting in the T-dispersion observed about -1 V.

In inversion, observed at $V_g \gtrsim 0$ V, the low frequency curve is expected to grow up again to C_{ox}, due to minority response. At room temperature and below, minority carriers at the interface are provided by generation and recombination (GR) mechanisms (Dimoulas et al., 2005)[1]. This explanation is supported quantitatively by the behavior of strong inversion capacitance as a function of frequency, shown in Fig. 4.3. The transition frequency that marks the change from low frequency behavior to high frequency behavior

[1]while above room temperature the dominant mechanism is diffusion of minority carriers from the bulk. Another mechanism is the supply of minority carriers from an inversion layer surrounding the MOS capacitor, but in this case the minority response would be observed also at low temperatures (Martens et al., 2008).

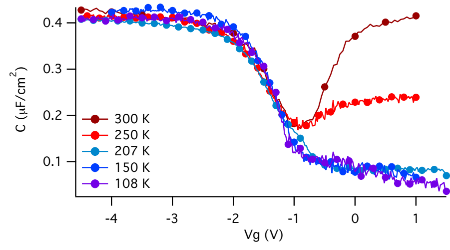

Figure 4.1: Low frequency $C-V$ curves at different temperatures. Sample: *G0p*; ac frequency: 50 Hz.

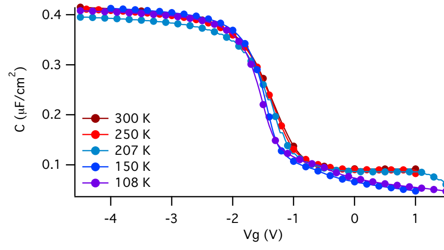

Figure 4.2: High frequency $C-V$ curves at different temperatures. Sample: *G0p*; ac frequency: 1 MHz.

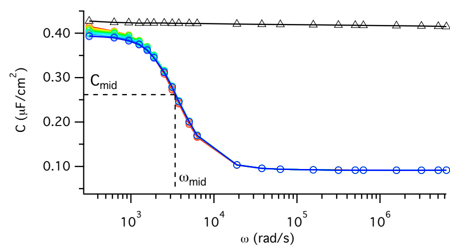

Figure 4.3: C as a function of ω, in accumulation and at different V_g in inversion. Sample *G0p*, $T = 300\,\mathrm{K}$, $V_g = -4.5\,\mathrm{V}, [0.3; 1]\,\mathrm{V}$ in accumulation and inversion, respectively. Accumulation capacitance (black triangles) is independent of frequency, while inversion capacitance (circles) shows τ behavior. Midway capacity is defined according to Eq. 4.1, yielding the corresponding ω_{mid}. $C_{\mathrm{ox}} = 0.432\,\mu\mathrm{F/cm}^2$, $C^{HF} = 0.092\,\mu\mathrm{F/cm}^2$, $C_{\mathrm{mid}} = 0.262\,\mu\mathrm{F/cm}^2$, $\omega_{\mathrm{mid}} = 2\pi 541\,\mathrm{Hz} = 3400\,\mathrm{rad/s}$

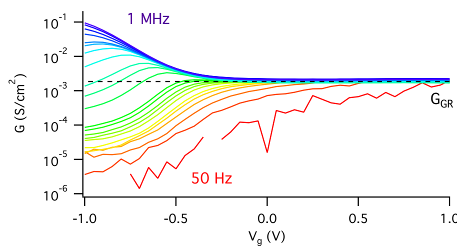

Figure 4.4: G as a function of V_g at different frequencies, sample *G0p*, $T = 300\,\mathrm{K}$. Approaching strong inversion, on the right, the conductance is given exclusively by $G_{\mathrm{GR}} = 1.85 \cdot 10^{-3}\,\mathrm{S/cm}^2$ (dashed line) defined in Eq. 4.2. Therefore, minority carriers GR alone is sufficient to explain the observed inversion C^{LF}.

can be defined as the angular frequency ω_{mid} for which C_{mid} is midway between C_{ox} and C^{HF} (Nicollian and Brews, 2003):

$$C_{\text{mid}} = C_{ox} - \frac{C_{ox} - C^{HF}}{2} \tag{4.1}$$

The conductance associated to the GR of the minority carriers is a function of ω_{mid} and is given by:

$$G_{\text{GR}} = \omega_{\text{mid}} \frac{C_{ox}}{1 - \frac{C^{HF}}{C_{ox}}} \tag{4.2}$$

Fig. 4.4 indicates that G observed in inversion is in very good agreement with Eq. 4.2, therefore supporting that minority carrier GR by the bulk traps is sufficient to explain the low frequency $C - V$ in inversion. A strong contribution from interface states is, thus, unlikely. By looking again at Fig. 4.1, it is now possible to understand the inversion behavior as a function of T: at lower temperatures ω_{mid} decreases and eventually gets lower than the minimum available angular frequency $\omega_{\text{min}} = 2\pi 50\,\text{rad/s}$. When $T = 250\,\text{K}$, then $\omega_{mid} \approx \omega_{\text{min}}$, while for $T \lesssim 200\,\text{K}$, $\omega_{mid} \ll \omega_{\text{min}}$ and the characteristic minority response in inversion is not observed at all. Finally, the evidence of minority carrier response also indicates that the gate leakage is negligible.

Fig. 4.2 displays the high frequency $C - V$ curves. Again, T-dispersion in accumulation is limited and this enables to calculate C_{ox} with good confidence. Following the Kar method (Kar, 2003), $1/C^{HF}_{\text{acc}}$ *vs* $\sqrt{\text{d}/\text{d}V(1/C^{HF}_{\text{acc}})^2}$ is plotted and a linear fit to the points in the strong inversion region gives C_{ox}^{-1} as the y-intercept of the line. Fig. 4.5 shows the fitting to the high frequency $C - V$ curve , recorded at 250 K, in the region $-4.48\,\text{V} < V_g < -3.32\,\text{V}$.

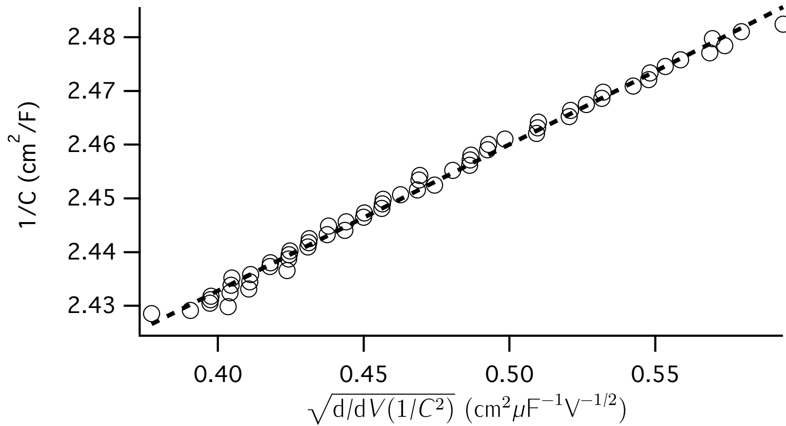

Figure 4.5: $1/C^{HF}_{\text{acc}}$ *vs* $\sqrt{\text{d}/\text{d}V(1/C^{HF}_{\text{acc}})^2}$ plot from sample *G0p*. $T = 250\,\text{K}$ and modulation frequency 1 MHz. Experimental points (red circles) are taken in the strong accumulation region, corresponding to gate voltage in the range $[-4.48; -3.32]\,\text{V}$. Data lie in a straight line, as predicted by Kar's model, and fit to the data (black dashed line) yields $C_{ox} = 0.43\,\mu\text{F/cm}^2$ as the reciprocal of y-intercept.

The depletion region of the high frequency $C - V$ curve (see Fig. 4.2) confirms the limited voltage shift when T is varied. It is interesting to notice that, in inversion, the curves have two distinct behaviors: at T above 200 K the capacitance does not vary

appreciably in the range 0 V $< V_g <$ 1 V, while below 200 K the capacitance decreases asymptotically to the minimum with increasing V_g. This peculiarity can be explained by invoking a weak Fermi level pinning (Simmons and Wei, 1973; Wei and Simmons, 1974; Grassman et al., 2008; Martens et al., 2008). This phenomenon occurs at high D_{it}, when it gets of the same order of magnitude of C_{ox}/q^2, or $\approx 3 \cdot 10^{12}\,\mathrm{eV^{-1}cm^{-2}}$ in the case of sample *G0p*. Weak Fermi level pinning manifests as a pronounced stretch out of the $C - V$ curve along the voltage axis (the extreme case is complete Fermi level pinning). The weak Fermi level pinning is made evident when calculating the apparent doping level by Eq. 2.8. Fig. 4.6 shows that an unphysical high doping level is obtained when $T > 200$ K. Cooling below 200 K results in a flat doping profile, as expected for molten doped samples. Unfortunately, interface traps can distort the $C - V$ shape by inducing a stretch out of the curve resulting in an overestimation of N_A. Resorting to the max-min capacitance method yields $N_A = 3.5 \cdot 10^{16}\,\mathrm{cm^{-3}}$ as best estimate.

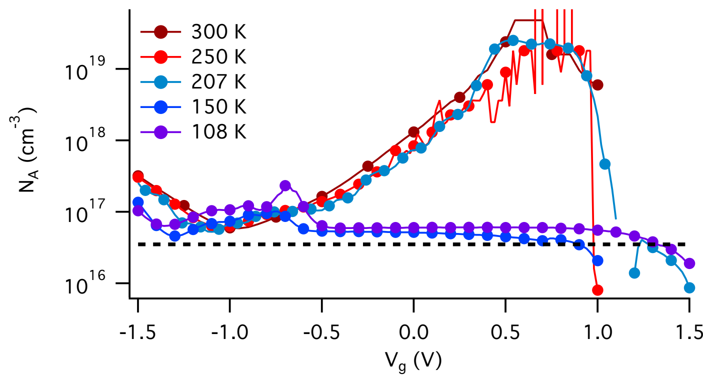

Figure 4.6: Apparent doping concentration N_A in the subinterface region of the semiconductor. N_A is calculated from high frequency $C - V$ curve according to Eq. 2.8 and, in the ideal MOS, represents the density of ionic charge at the edge of the depletion layer. In *p*-type substrates, the depletion layer width increases with positive V_g, extending up to $\approx 0.3\,\mu$m in the bulk for Ge at room temperature and $N_A \approx 10^{16}\,\mathrm{cm^{-3}}$. In real MOS, interface traps cause a stretch out of the $C - V$ curve and the apparent N_A can be regarded as an upper bound. The best estimate based on the max-min capacitance method is $3.5 \cdot 10^{16}\,\mathrm{cm^{-3}}$ and is indicated by the dashed line on the graph.

Following this preliminary analysis, ideal $C - V$ curves are calculated at each experimental temperature, in the high and low frequency limit, using the best estimates of C_{ox} and N_A. Comparison between calculations and experiments is shown in Fig. 4.7 (a) and (b) for the two representative temperatures 300 K and 108 K. Simulations reproduce the experimental data and validate the qualitative analysis above:

- The flatband voltage V_{FB}, visualized as the voltage difference between the zeros of the top and bottom scales, is not affected much by the temperature. The fairly negative value, $V_{FB} \approx -1.4$ V for both high and low T, indicates the presence of positive fixed charges in the oxide. Quantitative substantiation is given in Fig. 4.8, showing the $\psi_S - V_g$ curves calculated according to Eq. 2.9.

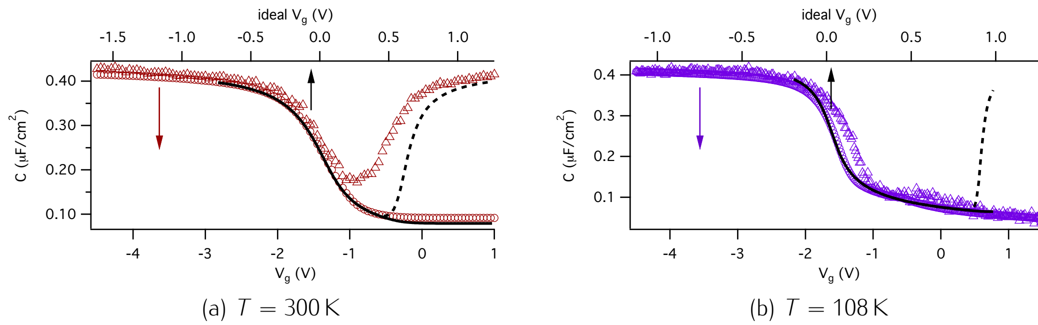

(a) $T = 300\,\mathrm{K}$ (b) $T = 108\,\mathrm{K}$

Figure 4.7: Comparison between ideal and experimental $C-V$ curves of sample *G0p*, for $T = 300\,\mathrm{K}$ (a) and $T = 108\,\mathrm{K}$ (b). Experimental data measured using 1 MHz and 50 Hz ac modulation frequency are displayed with circles and triangles, respectively. Ideal curves in the high and low frequency limits, represented as solid and dashed lines respectively, are simulated using the best estimate values of $C_{ox} = 0.43\,\mu\mathrm{F/cm}^2$ and $N_A = 3.5 \cdot 10^{16}\,\mathrm{cm}^{-3}$. Notice the different scale of the abscissa axis in the ideal (top) and experimental (bottom) case necessary to match the $C-V$. In (b) the increase of C at high positive voltages, due to minority response in the low frequency theoretical curve, is not observed experimentally. Minority carrier generation, in fact, has a very long time constant that, according to Eq. 1.62 and 1.63, requires ac modulation frequencies below $10^{-2}\,\mathrm{Hz}$ to be observed at 110 K.

- The difference in the scale of the x-axes, necessary to match the two curves, evidences an appreciable stretch-out of the experimental $C-V$. This effect is attributed to the charging of interface states due to the V_g sweep.
- In depletion the experimental low frequency curve lies above the theoretical one, as expected when interface traps can follow the ac modulation. Trap contribution to the capacitance is given by Eq. 1.57. At low temperatures the characteristic times of the traps increase and, in the case of deep levels, are extremely long. τ can exceed several seconds and, therefore, very low frequencies are necessary to maintain thermal equilibrium with the free charges. For this reason, the experimental value of $\omega = 2\pi 50\,\mathrm{rad/s}$ does not satisfy the low frequency condition $\omega\tau \ll 1$ over the whole V_g span and the lower frequency curve in Fig. 4.7b approaches the high frequency curve as V_g is increased and deeper lying traps are accessed.
- In inversion, $C-V$ characteristics differ significantly between high and low T. Ideal curves reproduce nicely the data at $T = 108\,\mathrm{K}$, indicating that the estimation of the doping density is correct. The deviation of the experimental high frequency $C-V$ from the simulation observed at $T = 300\,\mathrm{K}$ can be explained, therefore, as a weak Fermi level pinning. Increasing V_g does not contribute to the shift of ψ_S, but the charge is trapped at the interface instead. In turn, the width of the space charge region is not affected by V_g and C does not decrease.
- Minority carrier response is observed in inversion only at high temperatures, when carrier generation and recombination are able to keep in pace with the ac modulation of the surface potential.

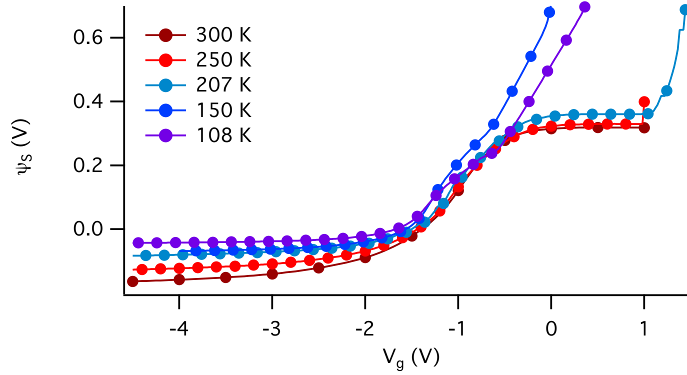

Figure 4.8: $\psi_S - V_g$ curves of sample *G0p*, calculated according to Eq. 2.9.

Conductance Method

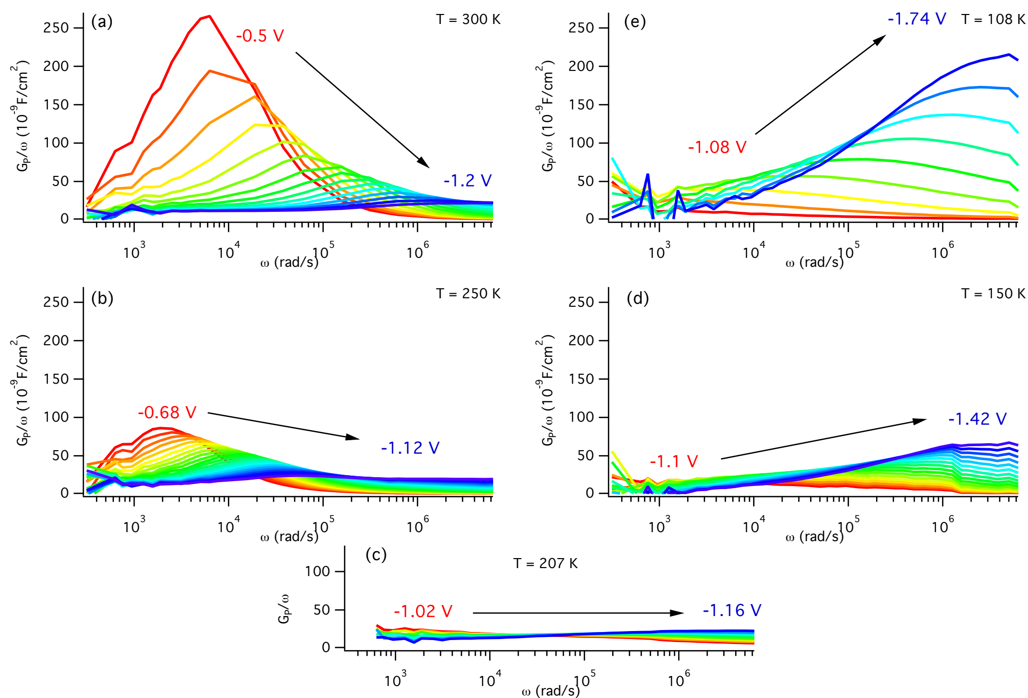

Figure 4.9: $G_P/\omega - \omega$ plots in depletion regime, for different values of V_g, sample *G0p*. Maximum and minimum bias is indicated and the curves are color coded accordingly. The curves show a maximum as a function of ω. The location and the amplitude of the peak vary together with V_g as indicated by the arrow. Measurements at different temperatures are displayed to show the influence of T on the conductance: (a) room temperature, (b) 250 K, (c) 207 K, (d) 150 K, (e) 108 K.

Fig. 4.9 shows the equivalent parallel conductance as a function of ω for selected values of V_g corresponding to MOS in depletion regime. Measurements at different temperatures are displayed: (a) room temperature, (b) 250 K, (c) 207 K, (d) 150 K, (e) 108 K. Every plot has the same characteristic features:

- G_P/ω *vs.* $\log\omega$ curves show a maximum,

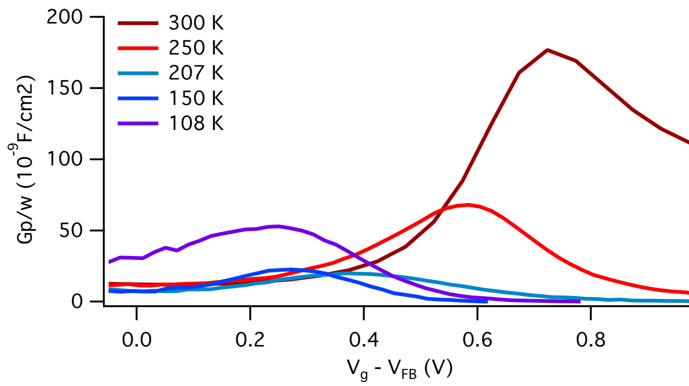

Figure 4.10: G_P/ω as a function of V_g, corrected for flatband voltage shift. Frequency is 3 kHz at all temperatures, sample *G0p*. The conductance shows a maximum and the location of the peak moves with T.

- the location of the G_P/ω peak is a strong function of the bias,
- the amplitude of the G_P/ω peak is a weak function of the bias, if compared to the former,
- by looking at a fixed frequency, G_P/ω as a function of V_g also shows a maximum, as more clearly shown in Fig. 4.10.

These four features are all explained quantitatively only by the interface trap model discussed in chapter 1.2, namely, a distribution of single-level interface traps, isolated from one another, with energies throughout the bandgap subject to band bending fluctuation. A maximum in G_P/ω as a function of ω occurs when the ac modulation frequency matches the capture rate of the traps with energy level crossed by the oscillating chemical potential at the interface. By varying V_g, different trap levels in the bandgap are accessed. Since the capture rate is a strong function of energy, also it is the peak frequency. On the other hand, the amplitude of the peak is proportional to $D_{it}(E = \mu)$. Therefore, a smooth D_{it} leads to a peak amplitude that, on a relative scale, varies much less than the peak frequency when the gate bias is changed. Similarly, at a fixed frequency, a peak in G_P/ω is found when V_g lines up the chemical potential to the traps at the right energy depth in the bandgap, with characteristic time of the order of $1/\omega$.
Temperature affects both τ (through Eq. 1.31) and the position of the chemical potential (through Eq. 1.20). Therefore, at different temperatures, different regions of the bandgap are accessible, resulting in different conductance spectra.

To give quantitative substantiation to the qualitative remarks above, G_P/ω *vs.* $\log\omega$ curves are fitted according to Eq. 2.14 for every V_g separately. The fitting function has three parameters, namely, peak amplitude in terms of maximum conductance $[G_P/\omega]_{\omega=\omega_p}$, peak location in terms of angular frequency at maximum conductance ω_p, and peak width in terms of band bending fluctuation parameter σ_S. Fit to the data is satisfactory over a wide range of frequency and bias[2]. Fig. 4.11 shows the data at $T = 108$ K as a representative case: the model reproduces accurately the shape of the peak, both the maximum and the wings, as confirmed by the plot of the residuals (see Fig. 4.12).

Fitting results ($[G_P/\omega]_{\omega=\omega_p}$, ω_p, and σ_S for any given V_g), can be plotted as a function of the position of the chemical potential by using the $\psi_S - V_g$ relationship obtained before:

[2]The noise in the experimental spectra is inversely proportional to the measurement frequency. In order to improve the quality of the fitting, a ω-dependent error is assumed of the form $W(\omega) = 1 \cdot 10^{-9}$ S/cm^2 $\times$ $(\omega/2\pi\, 10^6\,\text{MHz})^{-1/4}$.

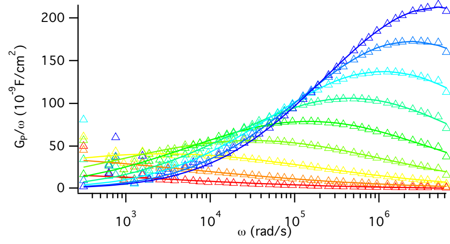

Figure 4.11: G_P/ω as a function of ω at selected V_g in depletion region ($-1.74\,\text{V} < V_g < -1.08\,\text{V}$ as in Fig. 4.9), $T = 108\,\text{K}$, sample *G0p*. Experimental data (triangles) are fitted accurately by the model (solid lines)

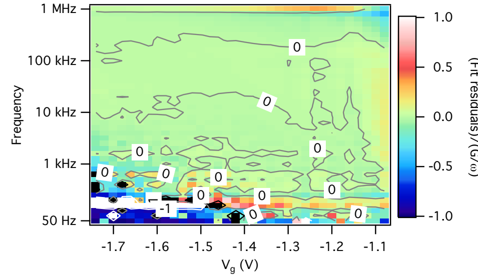

Figure 4.12: 2D representation of the normalized fitting residuals given by (fitting-experimental)/experimental. Bias is on the x-axis and frequency on the y-axis.

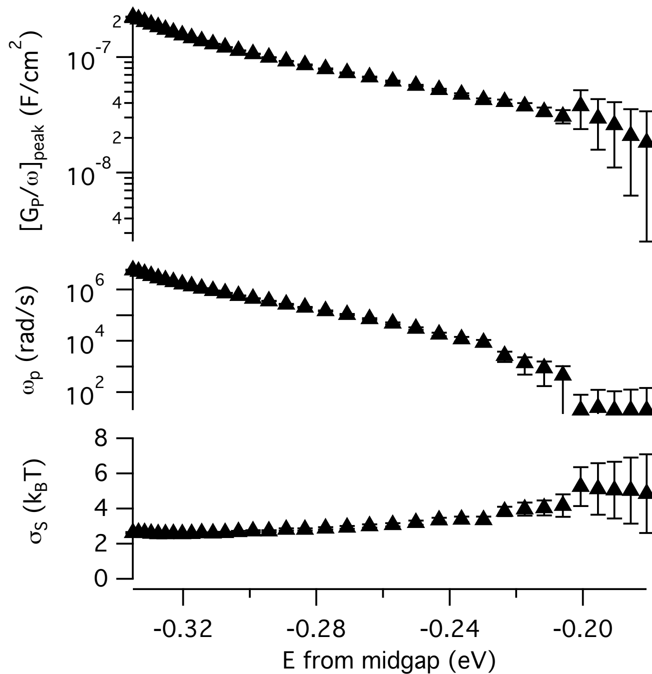

Figure 4.13: Conductance peak fitting results, $T = 108\,\text{K}$, sample *G0p*. On the x-axis it is reported the position of the chemical potential calculated from midgap, according to Eq. 4.3. The first graph on top shows the amplitude of the G_P/ω peak, the graph in the middle shows the location of the G_P/ω peak in terms of angular frequency, and the third graph at the bottom shows the band bending fluctuations, defined as the parameter σ_S in Eq. 2.14.

$$\mu(\psi_S; T) = q\psi_S + q\phi_B(T) + E_i(T) \tag{4.3}$$

where the dependency on the temperature is indicated explicitly. Fig. 4.13 shows that, at $T = 108\,\text{K}$, the amplitude of the peak increases when trap levels closer to the band edge are accessed. This means that D_{it} grows toward the valence band side. In the same way, ω_p increases approaching the band edge, confirming that shallower traps have shorter capture time constants. The last parameter, σ_S, increases slightly when moving the chemical potential away from the VB. This behavior can be interpreted as a growth of band bending fluctuations, which, in turn, indicates an increment of charge at the interface. The broadening of σ_S when traps are filled by electrons suggests that interface

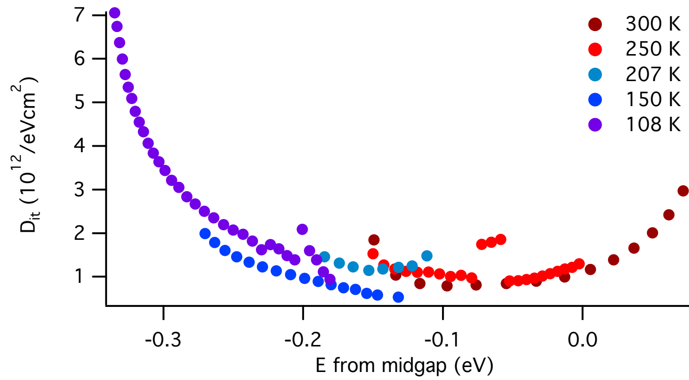

Figure 4.14: D_{it} as a function of energy in the bandgap, sample *G0p*. Data are obtained by fitting the conductance spectra measured at different temperatures, as indicated by colors. D_{it} is then calculated through Eq. 2.12 using $[G_P/\omega]_{\omega=\omega_p}$ and σ_S returned by the fitting. Data at different temperatures overlap nicely and cover continuously the lower half of the bandgap.

traps, in this energy range, are acceptors.

The fitting procedure is repeated for all the different temperatures, calculating, thereafter, D_{it} from $[G_P/\omega]_{\omega=\omega_p}$ and σ_S through Eq. 2.12. The range of temperature has been chosen in order to obtain the full coverage of the energies in the lower half of the bandgap. The results at different temperature, shown in Fig. 4.14, overlap nicely as a continuous distribution, indicating the correctness of the physical model adopted in the analysis.

Error Analysis

Different sources of uncertainty have to be considered in order to estimate the error affecting D_{it} (and the other quantities of interest τ and σ_S). It comes out that the uncertainty in the reading of the instrument, due to the noise either in capacitance or conductance, is negligible. R_s, too, does not affect the results appreciably. The interface trap model reproduces the conductance peaks with good precision and, correspondingly, the relative error of the fitted parameters is below 2% for peak amplitude and σ_S and can be much lower than 1% for ω_p. C_{ox} can be estimated quite accurately through Kar's method (within a few percent), while it is very difficult to calculate $N_{A,D}$ with the same confidence level. Getting an estimation of doping level within the active area of the MOS, of the order of 10^{16} atoms/cm^3, with more than one significant digit can be challenging. $C-V$ based methods are among the most accurate for this application, are simple, do not require calibrated samples or complex equipment (Deal et al., 1965; Shappir et al., 1980; Zohta, 1973). And, above of all, are sensitive exactly to dopants in the active area of the MOS. Hall effect is another accurate electrical technique, but inhomogeneities in doping level at the interface are a limiting factor (Larrabee and Thurber, 1980). Optical techniques, on the other hand, are very sensitive and accurate but quantitative doping measurements require known standards (Burstein et al., 1956; Picus et al., 1956; Charles Baber, 1980; Tajima, 1978). Secondary Ion Mass Spectrometry (SIMS) does not have the sensitivity of electrical and optical techniques and requires precise calibration of the sputtering rate

(Felch, 1996).
Propagating the uncertainty associated to C_{ox} and $N_{A,D}$ down to the D_{it} *vs.* E curve can be quite complicated. These two quantities affect the final result through many highly non-linear relationships: C_{ox} enters the calculation of equivalent parallel conductance, through Eq. 2.10, and the calculation of $N_{D,A}$ itself, by the Max-Min conductance method; $N_{D,A}$ is used to calculate the position of the chemical potential in the bulk, through Eq. 1.20; C_{ox} and $N_{D,A}$, together, determine the $C-V$ curves for the ideal MOS, through Eq. 1.44, Eq. 1.46, Eq. 1.48. In particular, the ideal high frequency $C-V$ curve is the basis for the calculation of the $\psi_S - V_g$ relation that is used to estimate the position of the chemical potential at the interface for any given V_g. Therefore, the uncertainty is translated into an error on the energy scale.
Being impossible to propagate the uncertainty in an analytical way, a heuristic method is adopted to evaluate the confidence interval of the $D_{it} - E$ curve. C_{ox} and $N_{A,D}$ are allowed to vary in a domain $\mathcal{D} = [C_{ox} - \sigma_{C_{ox}}, C_{ox} + \sigma_{C_{ox}}]; [N_{A,D} - \sigma_{N_{A,D}}, N_{A,D} + \sigma_{N_{A,D}}]$, where $\sigma_{C_{ox}}$ and $\sigma_{N_{A,D}}$ are the standard deviation associated to C_{ox} and $N_{A,D}$ respectively. The next step is to pick up a pair $(C_{ox}, N_{A,D}) \in \mathcal{D}$ and repeat the process of extraction of D_{it}: the ideal $C-V$ curves are calculated from the new values and the $\psi_S - V_g$ relation is evaluated again; the equivalent parallel conductance G_P is obtained from C and G, conductance peaks are fitted (for each V_g and T) and, finally, D_{it} is obtained from the peak amplitudes. Fig. 4.15 is obtained by repeating these steps for a number of pairs $(C_{ox}, N_{A,D}) \in \mathcal{D}$ and plotting the resulting $D_{it} - E$ curves, giving a reliable estimation of the uncertainty.

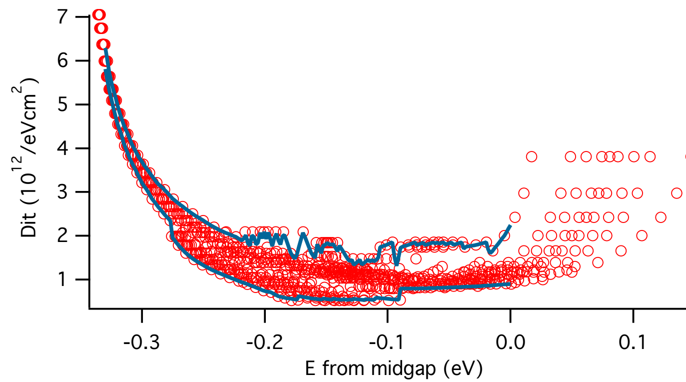

Figure 4.15: Confidence interval of the density of interface traps estimated by the conductance method, sample *G0p*. C_{ox} and N_A are allowed to vary in the domain $[C_{ox} - \sigma_{C_{ox}}, C_{ox} + \sigma_{C_{ox}}]$; $[N_A - \sigma_{N_A}, N_A + \sigma_{N_A}]$, resulting in the dispersion of the curves displayed in the plot (red circles). The envelope of the distribution is evidenced (blue line). $C_{ox} = 0.43 \pm 0.01\,\mu\text{F/cm}^2$, $N_A = 3.5 \cdot 10^{16} \pm 1 \cdot 10^{16}\,\text{cm}^{-3}$.

Capacitance Methods

The D_{it} obtained by the conductance method can be validated using LF and HF/LF methods described in Eq. 2.19 and 2.21. The methods are employed only with the capacitance measured at room temperature, in order to satisfy the low frequency condition. The error analysis adopted for the conductance method is performed also in this case,

varying C_{ox} and N_A in the range $[0.42; 0.44]\,\mu F/cm^2; [2.5 \cdot 10^{16}; 4.5 \cdot 10^{16}]\,cm^{-3}$. The results are shown in Fig. 4.16.

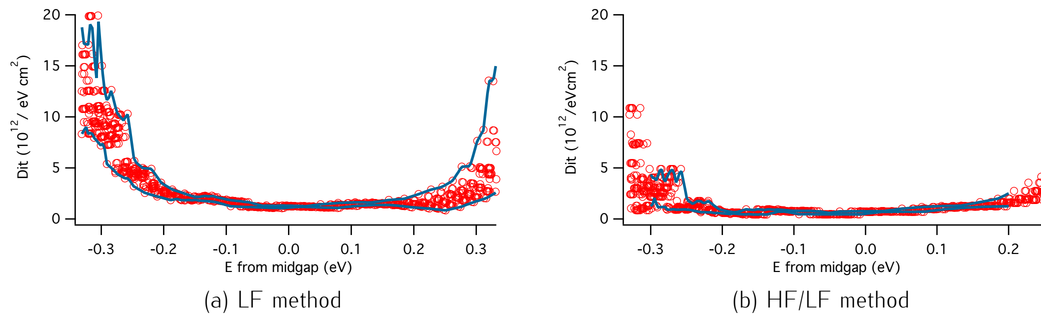

(a) LF method (b) HF/LF method

Figure 4.16: Alternative methods for the estimation of D_{it} in sample *G0p*. In the same way as in Fig. 4.15, the dispersion of the curves resulting from the different choices of C_{ox} and N_A is displayed (red circles) and the envelope of the distribution is outlined (blue line). $C_{ox} \in [0.42; 0.44]\,\mu F/cm^2, N_A \in [2.5 \cdot 10^{16}; 4.5 \cdot 10^{16}]\,cm^{-3}$. Notice that the HF/LF method gives D_{it} only over a limited range of the gap, while the LF method is valid over the whole bandgap.

Summary

It is now possible to compare directly the D_{it} obtained with three different methods. Conductance is the most accurate and sensitive method and the range of the bandgap that can be accessed by this technique can be extended by varying the temperature. Nevertheless, it is open to artifacts, as the depletion region must be identified carefully. Therefore, LF method can help in identifying the trend of the D_{it} across midgap and, except when very low density of interface traps are present, it yields sensible quantitative estimates. HF/LF method has a limited range but it provides a rather independent estimation of the D_{it} in depletion and across midgap without resorting to a theoretical calculation. The comparative analysis is shown in Fig. 4.17. D_{it} calculated with the different methods are consistent, within the experimental errors. LF method results in a slight overestimation of the D_{it}, if compared to conductance method, while HF/LF method yields the lowest values among the three. By looking closer to the midgap region (see Fig. 4.18), Conductance method (green) shows an increase in D_{it} approaching midgap (and an increase in the

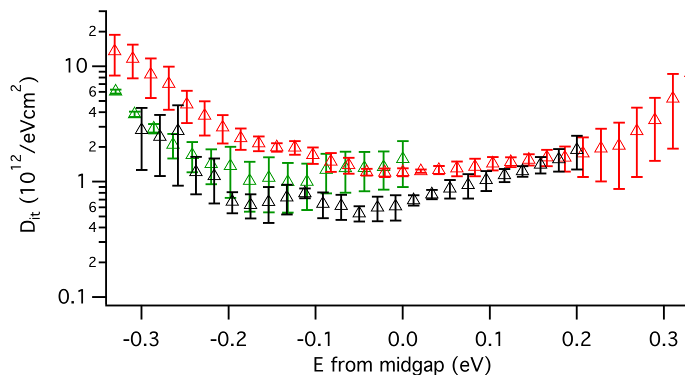

Figure 4.17: D_{it} distribution inside the bangap obtained with three different methods, sample *G0p*. D_{it} from conductance (green) is consistent with the results of LF method (red) and HF/LF method (black), within experimental accuracy.

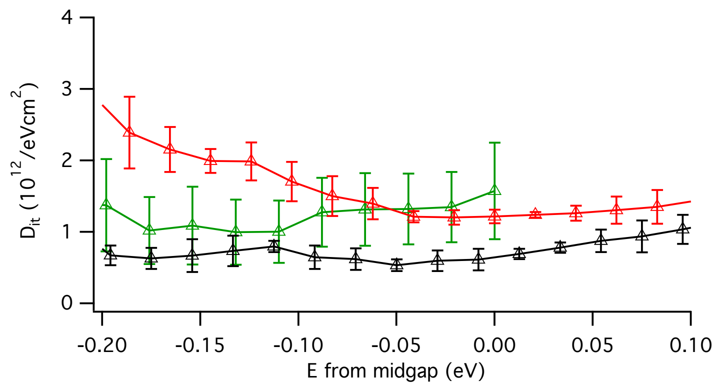

Figure 4.18: D_{it} distribution inside the bangap, sample *G0p*. Close up on the midgap region. Conductance method (green) shows an increase in D_{it} approaching midgap, while LF method (red) and HF/LF method (black) show a smooth, flat, D_{it}.

error, too), while LF method (red) and HF/LF method (black) show a smooth, flat, D_{it}. The mismatch in the curves can be attributed to an artefact of the conductance method. A drawback of the conductance analysis, especially in narrow bangap materials, is that when the depletion region is not clearly identified due to the uncertainty in the $\psi_S - V_g$ relation, weak inversion response can be mistaken for a real growth of the D_{it} (Martens et al., 2008). The admittance characteristic in weak inversion and in depletion are very similar, but the same D_{it} results in much higher G_P/ω peaks in weak inversion than in depletion. The difference can be up to one order of magnitude, leading to an overestimation of the trap density. Weak inversion produces narrower peaks, similar to the response of a single trap level (see Fig. 2.17). The width of the conductance peaks, defined through the parameter σ_S, is shown in Fig. 4.19 as a function of energy in the bandgap. A marked

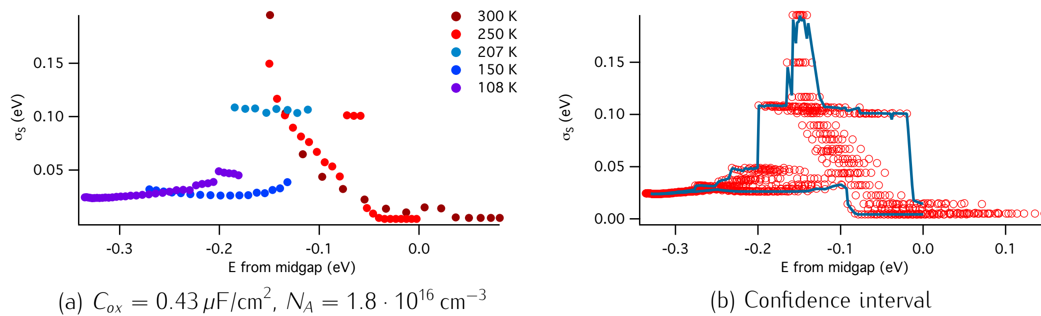

(a) $C_{ox} = 0.43\,\mu$F/cm^2, $N_A = 1.8 \cdot 10^{16}$ cm^{-3}

(b) Confidence interval

Figure 4.19: σ_S as a function of energy in the bandgap, sample *G0p*. σ_S represents the broadening of the peak due to band bending fluctuations. Weak inversion response is characterized by narrower peaks, resulting in a lower σ_S.

reduction in σ_S occurs approaching midgap energy, therefore supporting the attribution to a weak inversion of the response observed in that regime.

The conductance method can provide also an estimate of the capture cross section σ_p of the interface traps. Eq. 2.15 allows to calculate the characteristic time of the traps τ_p

from the peak frequency ω_p [3]. In this way, σ_p can be obtained through Eq. 2.16

$$\begin{aligned}\sigma_p &= \frac{1}{\tau_p v^{th} N_V} \exp\left(\frac{q\phi_S - E_V}{k_B T}\right)\\ &\approx \frac{1}{\tau_p T^2 \times 1.09 \cdot 10^{21}\,\mathrm{cm^{-2}s^{-1}K^{-2}}} \exp\left(\frac{q\phi_S - E_V}{k_B T}\right)\end{aligned}$$

for p-type Ge substrates. Unfortunately, σ_p depends on ψ_S exponentially, therefore the uncertainty in ψ_S is amplified to σ_p. As shown in Fig. 4.20, only the order-of-magnitude of σ_p can be estimated, yielding $\sigma_p \approx 10^{17}\,\mathrm{cm}^2$

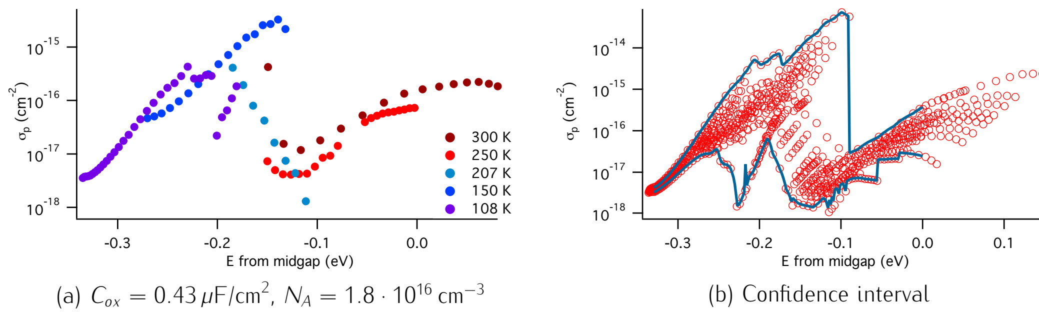

(a) $C_{ox} = 0.43\,\mu\mathrm{F/cm}^2$, $N_A = 1.8 \cdot 10^{16}\,\mathrm{cm}^{-3}$

(b) Confidence interval

Figure 4.20: σ_p as a function of energy in the bandgap, sample *G0p*. σ_p depends on ψ_S exponentially, therefore the uncertainty in ψ_S is amplified to σ_p and only an order-of-magnitude estimation is possible.

LF method provides the first data on the upper side of the bandgap, at energies above midgap. Even though the error bar is quite large, it is interesting to note that the D_{it} is fairly symmetrical, as shown in Fig. 4.21.

[3] τ_p is the characteristic time of holes, the majority carriers in p-type substrates, while ω_p stands for the peak frequency of the conductance spectra.

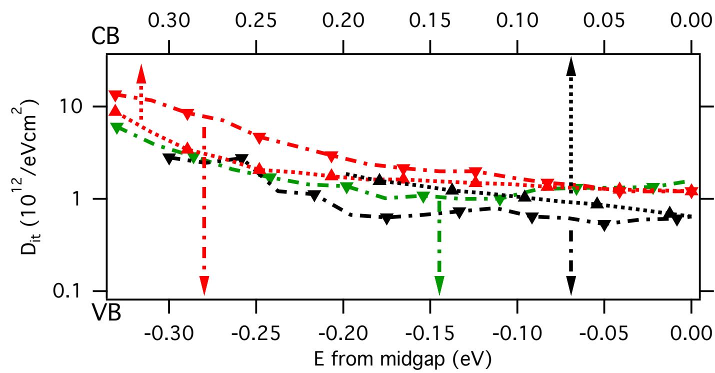

Figure 4.21: D_{it} distribution inside the bangap, sample *G0p*. The figure is equivalent to Fig. 4.17, with the difference that for positive energies (dotted lines) data are reported on the top axis while for negative energies (dashed lines) data are reported on the bottom axis. This provides a convenient way to visualize the symmetry of the D_{it} distribution. LF method (red curve) results in higher D_{it} at the VB side than at the CB side. On the other hand, conductance (green) and HF/LF (black) methods indicate comparable lower D_{it} at the VB side, more in line with the values provided by LF method at the CB side. Error bars are omitted for clarity.

4.2 p-type (111)Ge/GeO$_2$

The (111) oriented surface is expected to be more defective than the (001), owing to the higher number of bonds pointing outside from the surface. The p-MOS capacitors show indeed poorer characteristics, as it shown in the following.
Series resistance did not introduce appreciable distortions in the $C-V$ curves of sample *G1p*. Its value is estimated below 30 Ω in all experimental conditions, and the corresponding contribution to the admittance has been removed.

Capacitance curves display similar features to the previous sample, with well recognizable accumulation, depletion and inversion regimes. A closer look to Fig. 4.22 and 4.23, however, reveals a more pronounced dispersion among the curves recorded at different T, both in accumulation and depletion. Additionally, even at low temperatures, minority carrier response shows up in the low frequency curve in strong inversion. These anomalies are discussed in the following, aided by theoretical curves. Oxide capacitance and substrate doping are estimated as described in the previous section, employing Kar analysis and Max-min capacitance method, respectively. Ideal curves are shown in Fig.

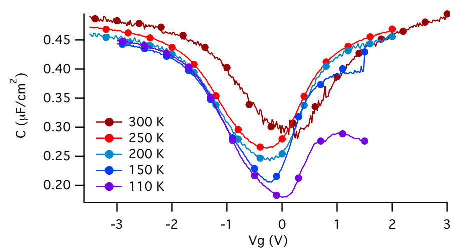

Figure 4.22: Low frequency $C-V$ curves at different temperatures. Sample: *G1p*; ac frequency: 50 Hz.

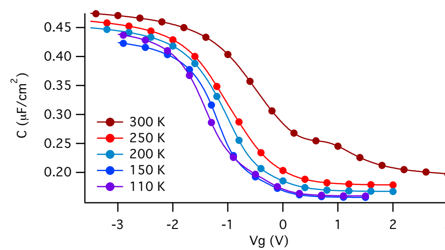

Figure 4.23: High frequency $C-V$ curves at different temperatures. Sample: *G1p*; ac frequency: 1 MHz.

4.24 for the representative cases of $T = 300$ K and $T = 110$ K. By extracting the $\psi_S - V_g$ relationship, the variation of flatband voltage shift with temperature is appreciable. Additionally, a comparison between Fig. 4.8 (sample *G0p*) and Fig. 4.25 (sample *G1p*) lets emerge a more noticeable stretch out in the last sample and a sort of pinning around midgap at lower temperatures. This puzzling behavior is interpreted as an indication of the presence of an inversion layer beyond the gate. Stronger flatband voltage shift is associated to the presence of oxide charge of positive sign. These charges may invert the surface beyond the gate without affecting the MOS characteristics in accumulation and depletion. However, in inversion regime the layer beyond the gate is put in communication with the charge build-up at the interface below the gate and it can act as a sink and a source of electrons. This mechanism is very efficient in providing carriers if compared to generation-recombination or diffusion. As a consequence, minority electrons can follow the ac modulation even at low temperatures (Nicollian and Goetzberger, 1965). The pinning in ψ_s at low temperatures is a further indication of a communication with an efficient reservoir of electrons.

The inversion layer beyond the gate does not influence significantly the admittance in depletion, provided the surface potential is not too close to the onset of inversion (this

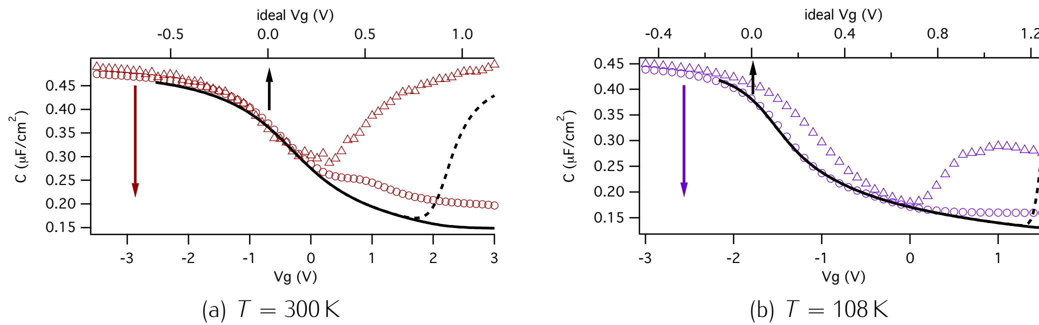

(a) $T = 300\,\mathrm{K}$ (b) $T = 108\,\mathrm{K}$

Figure 4.24: Comparison between ideal and experimental $C - V$ curves of sample *G1p*. Experimental data measured using 1 MHz and 50 Hz ac modulation frequency are displayed with circles and triangles, respectively. Ideal curves in the high and low frequency limits, represented as solid and dashed lines respectively, are simulated using the best estimate values of $C_{ox} = 0.48\,\mu\mathrm{F/cm}^2$ and $N_A = 2 \cdot 10^{17}\,\mathrm{cm}^{-3}$. Notice the different scale of the abscissa axis in the ideal (top) and experimental (bottom) case necessary to match the $C - V$.

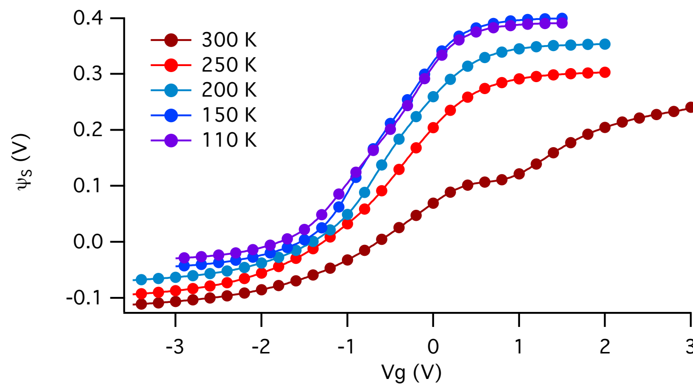

Figure 4.25: $\psi_S - V_g$ curves of sample *G1p*, calculated according to Eq. 2.9.

requirement is of course more stringent at room temperature). Clean conduction peaks are shown in Fig. 4.26 for $T < 300\,\mathrm{K}$: experimental data are well reproduced by the fitting function based on a continuous distribution of interface trap level model, together with band bending fluctuations induced by local charges. Conduction peak fitting allowed the estimation of the density of interface traps, the capture cross section, and the amount of band bending fluctuations. By using the $\psi_S - V_g$ relation and Eq. 4.3, it is possible to plot D_{it}, σ_p, and σ_S as a function of the position of the chemical potential (see Fig. 4.27). The qualitative features of the extracted D_{it} are very similar to what is observed in sample *G0p*. The density of interface traps increases towards VB edge, while it sets down to about $10^{12}\,\mathrm{eV}^{-1}\mathrm{cm}^{-2}$ approaching midgap. High temperature curves do not match very well, indicating the onset of weak inversion. By looking at Fig. 4.27 as a whole, it is possible to recognize the spurious nature of the increasing D_{it} at midgap: data at 250 K (red) show higher D_{it} and lower σ_S compared to data at 200 K (light blue) in the same energy region. Weak inversion, indeed, results in artificially narrowed peaks and overestimated D_{it}.

Capacitance methods provide an independent estimation for D_{it}, though, they are less accurate than conductance method. As it is observed in sample *G0p*, LF and HF/LF

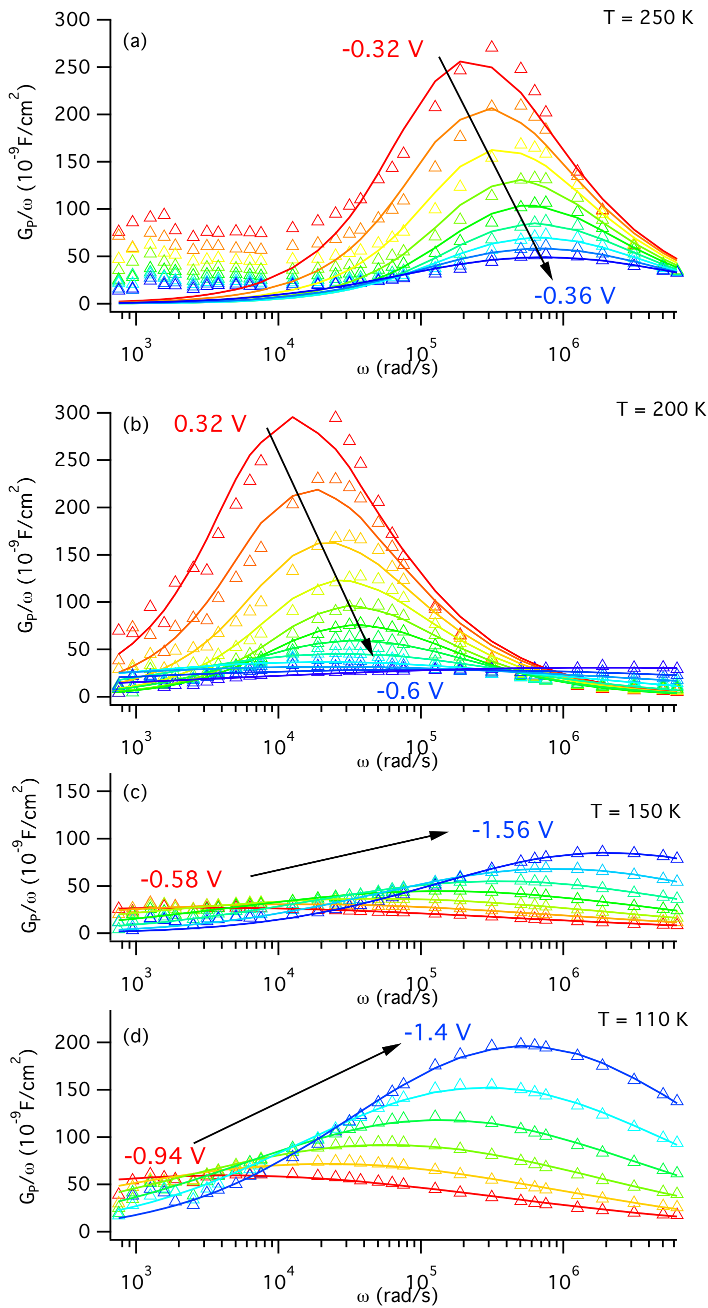

Figure 4.26: $G_P/\omega - \omega$ plots in depletion regime, for different values of V_g, sample *G1p*. Maximum and minimum bias is indicated and the curves are color coded accordingly. Experimental data (triangles) show a maximum as a function of ω. The location and the amplitude of the peak vary together with V_g as indicated by the arrow. Fitting to the data (solid line) indicates that the continuous distribution of interface trap level model and band bending fluctuations is accurate. Measurements at different temperatures are displayed to show the influence of T on the conductance: (a) 250 K, (b) 207 K, (c) 150 K, (d) 108 K.

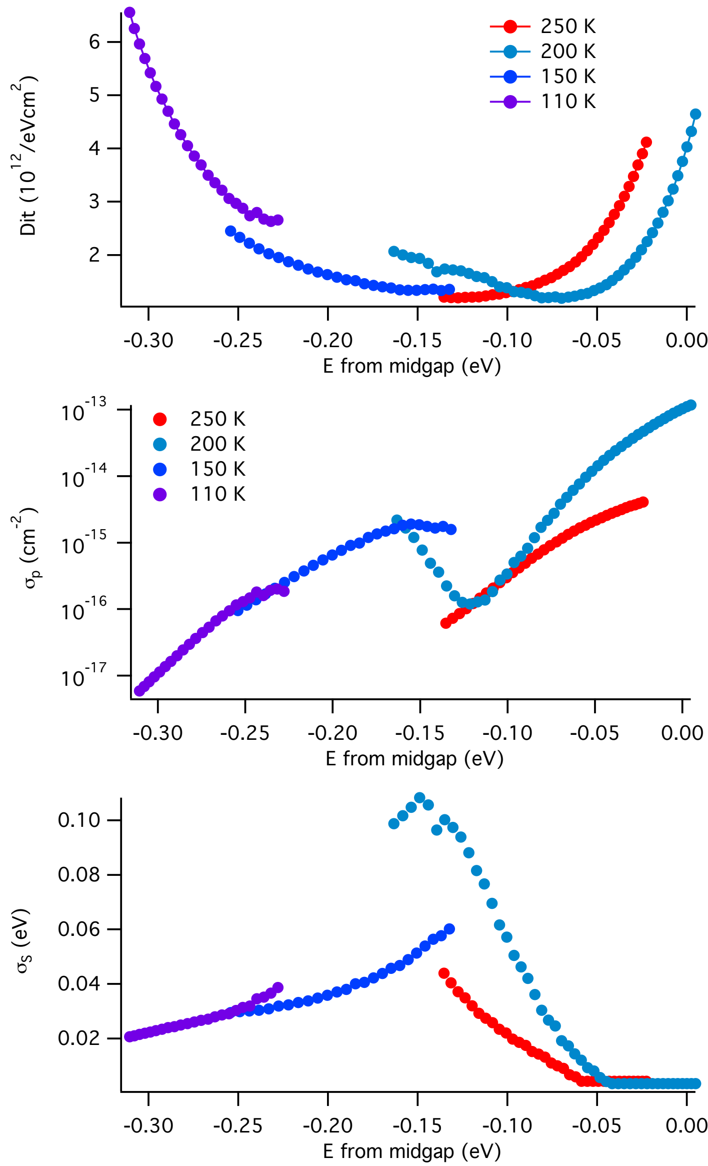

Figure 4.27: Outcomes of the conductance method, sample *G1p*. Colors indicate data at different temperatures. Top, D_{it} as a function of energy distance from midgap. Data at the lower temperatures nicely overlap, while the inversion layer beyond the gate can affect slightly the midgap region (see text for more detail). Middle, hole capture cross section. σ_p is in good qualitative and quantitative agreement with the data of sample *G0p*, confirming the similarity of the two interfaces. Bottom, band bending fluctuations due to local charges. As observed in sample *G0p*, fluctuations increase towards midgap, up to about -0.15 eV. The decrease at higher energy can be related to the onset of weak inversion.

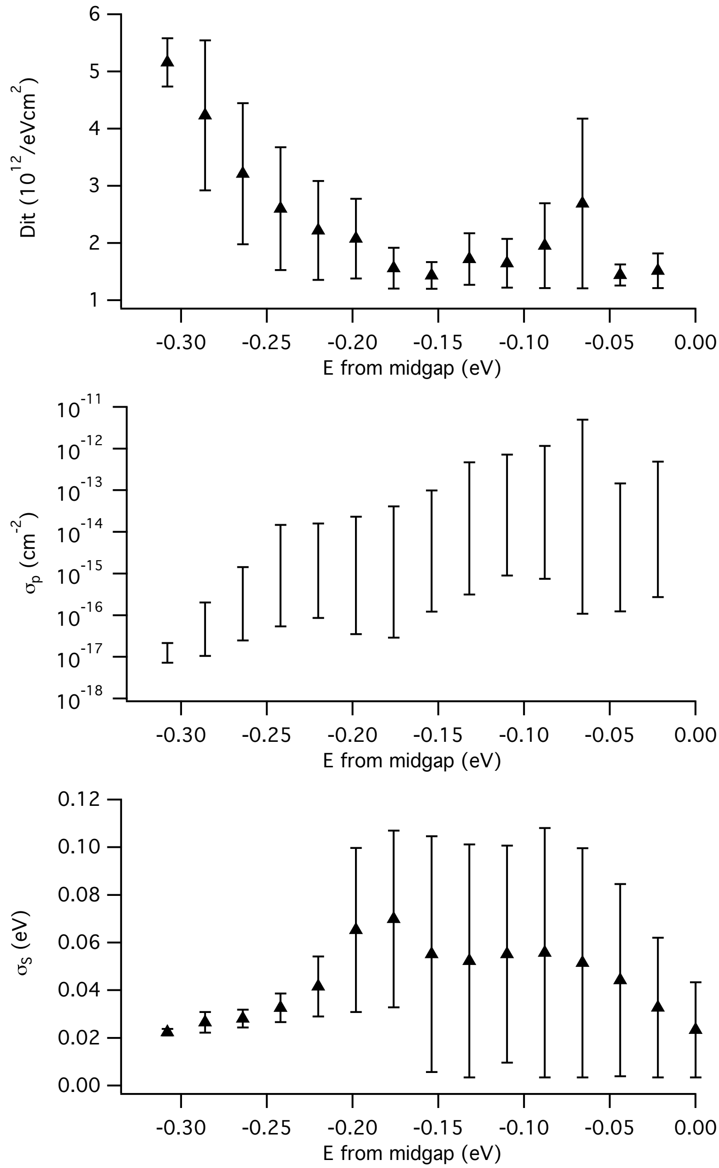

Figure 4.28: Outcomes of the conductance method, including error analysis. D_{it}, σ_p, and σ_S are plotted as function of energy distance from midgap in top, middle and bottom graphs, respectively. Error bands are obtained by varying oxide capacitance and substrate doping level as parameters, following the procedure described in the previous section. $C_{ox} \in [0.47; 0.49]\,\mu$F/cm^2 and $N_A \in [1 \cdot 10^{17}; 4 \cdot 10^{17}]\,$cm^{-3}.

methods confirm the overall U shape of the density of interface states, excluding any bump at midgap. Results are plotted in Fig. 4.29.

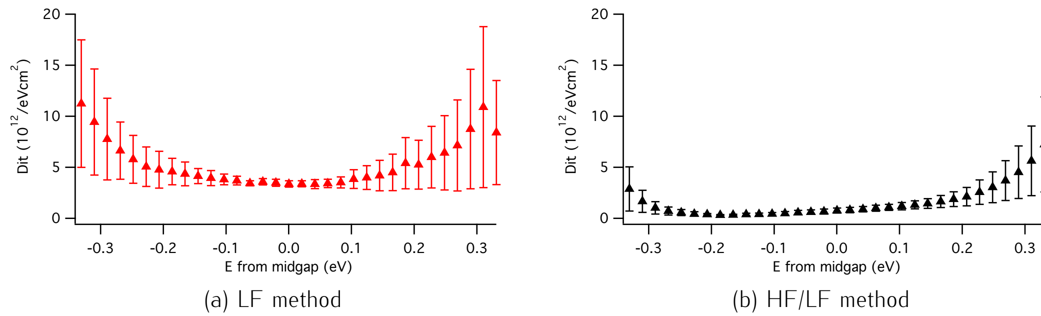

(a) LF method (b) HF/LF method

Figure 4.29: Alternative methods for the estimation of D_{it} in sample *G1p*. In the same way as in Fig. 4.28, the error bar reflects the dispersion of the curves resulting from the different choices of C_{ox} and N_A. $C_{ox} \in [0.47; 0.49]\,\mu\text{F/cm}^2$,$N_A \in [1 \cdot 10^{17}; 4 \cdot 10^{17}]\,\text{cm}^{-3}$. HF/LF method gives a reliable D_{it} over only a limited range of the gap, from the onset of accumulation to inversion, while the LF method is valid over the whole bandgap.

Fig. 4.30 indicates that the HF/LF method underestimate D_{it}. Many evidences support the presence of a relevant density of interface traps, starting from the stretch out of the curves and the frequency dispersion at low temperatures apparent in Fig. 4.24. The discrepancy with the other methods may indicate that a residual contribution of the interface traps can be present in the higher frequency capacitance curve. On the other hand, conductance method yields the most accurate quantitative estimation for D_{it}, provided that conductance peaks are obtained in strict depletion and trap capacitance do not exceed oxide capacitance (Martens et al., 2008). The extracted D_{it} at midgap indicates that trap capacitance $C_{it} = q^2 D_{it} \approx 0.3\,\mu\text{F/cm}^2$ is very close to $C_{ox} = 0.47\,\mu\ \text{F/cm}^2$, therefore it should be taken as a lower bound.

Concluding, from the interface trap standpoint, sample *G1p* shares the same qualitative features with sample *G0p*, but the density is comparatively higher, as shown in Fig. 4.31.

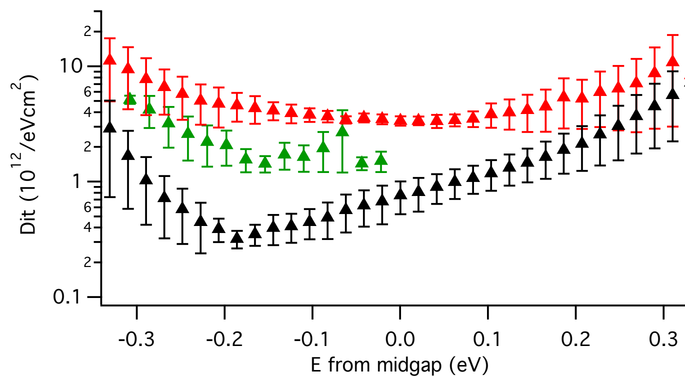

Figure 4.30: D_{it} distribution inside the bangap obtained with three different methods, sample *G1p*. D_{it} from conductance (green) is midway between the results of LF method (red) and HF/LF method (black).

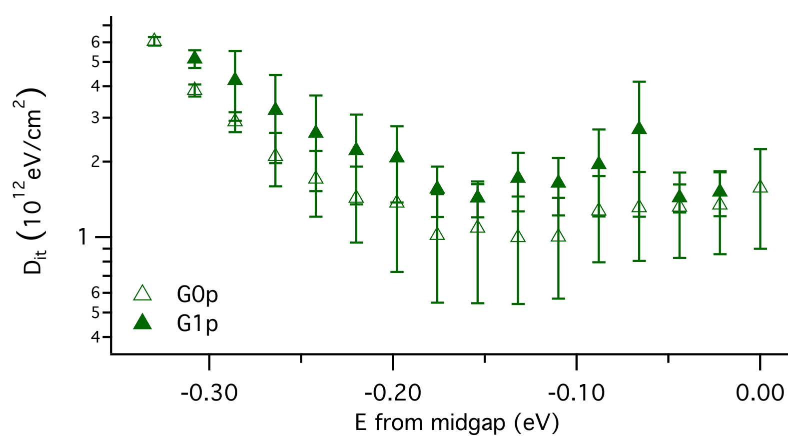

Figure 4.31: Comparison between D_{it} distributions in the lower half of the bangap obtained with the conductance method for samples *G0p* (outlined) and *G1p* (solid). The two surface orientations show D_{it} within experimental error, with the (111) more toward higher density of states.

The next two sections show the admittance data for n-type *G0p* and *G1p* samples. The $C-V$ characteristics are indicative of a good interface quality, both for the (001) oriented and the (111) oriented substrates. In contrast to the p-type substrates, the depletion conductance does not show peaks consistent with interface trap response. The minority carrier response is present in high temperature measurements for surface potential in the proximity of the midgap, while only a broad background is observed elsewhere, preventing the application of the conductance method to the extraction of interface trap properties. Therefore, the density of interface traps is estimated by capacitance methods only. LF and HF/LF methods yield reciprocally consistent results, reporting a low D_{it} in the upper half of the bandgap.

4.3 n-type (001)Ge/GeO_2

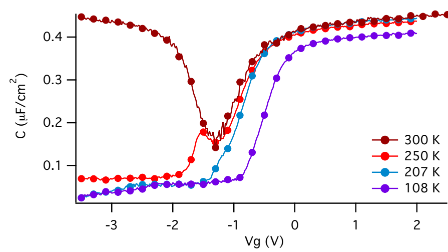

Figure 4.32: Low frequency $C-V$ curves at different temperatures. Sample: *G0n*; ac frequency: 50 Hz.

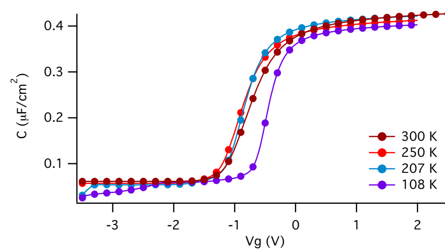

Figure 4.33: High frequency $C-V$ curves at different temperatures. Sample: *G0n*; ac frequency: 1 MHz.

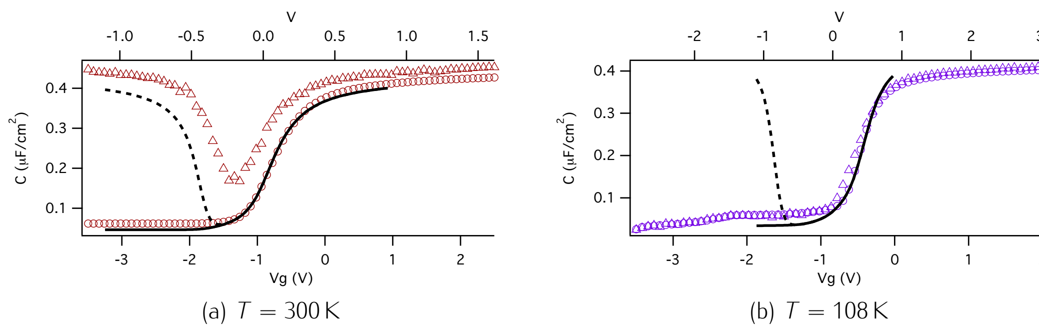

(a) $T = 300\,\mathrm{K}$ (b) $T = 108\,\mathrm{K}$

Figure 4.34: Comparison between ideal and experimental $C-V$ curves of sample *G0n*. Experimental data measured using 1 MHz and 50 Hz ac modulation frequency are displayed with circles and triangles, respectively. Ideal curves in the high and low frequency limits, represented as solid and dashed lines respectively, are simulated using the best estimate values of $C_{ox} = 0.43\,\mu\mathrm{F/cm}^2$ and $N_A = 0.8 \cdot 10^{16}\,\mathrm{cm}^{-3}$. Notice the different scale of the abscissa axis in the ideal (top) and experimental (bottom) case necessary to match the $C-V$.

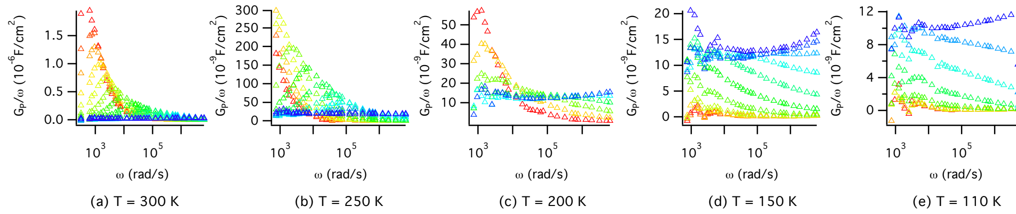

Figure 4.35: $G_P/\omega - \omega$ plots in depletion regime, for different values of V_g, sample *G0n*. In contrast to sample *G0p*, the curves do not show a maximum as a function of ω, except at room temperature where the peak is due to minority response in inversion. Measurements at different temperatures: (a) room temperature, (b) 250 K, (c) 207 K, (c) 150 K, (e) 108 K.

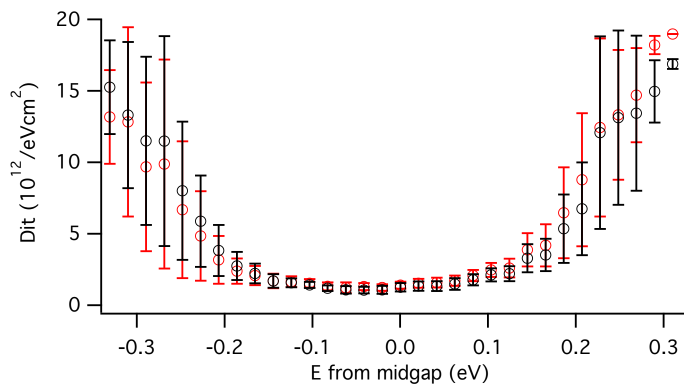

Figure 4.36: D_{it} distribution inside the bandgap obtained with capacitance methods, sample *G0n*. D_{it} from LF method (red) and HF/LF method (black) are in excellent agreement, well within experimental accuracy.

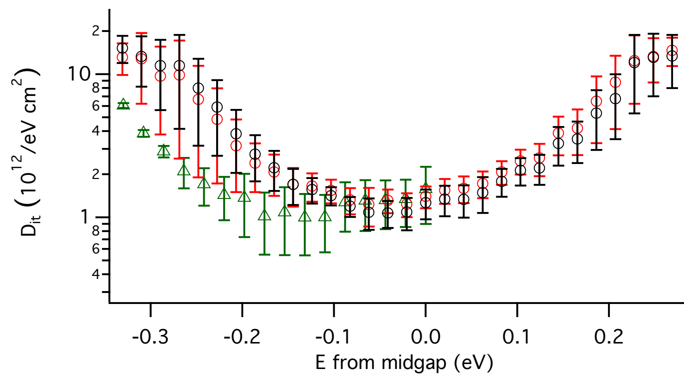

Figure 4.37: Comparison between *G0n* data (circles) and *G0p* data (triangles). Even though D_{it} extracted from *n*-type sample (red – LF method – and black – HF/LF method) is higher than D_{it} extracted from *p*-type sample (green), the two distributions are still within experimental accuracy. Conductance data are more accurate but available only in depletion. Capacitance data, on the other hand, are obtained over the whole bandgap, but the error in energy can be relevant in the strong inversion region (corresponding to the lower half of the bandgap in the figure).

4.4 n-type (111)Ge/GeO_2

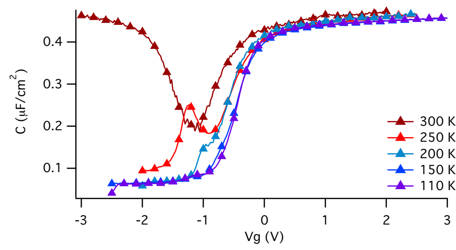

Figure 4.38: Low frequency $C-V$ curves at different temperatures. Sample: *G1n*; ac frequency: 50 Hz.

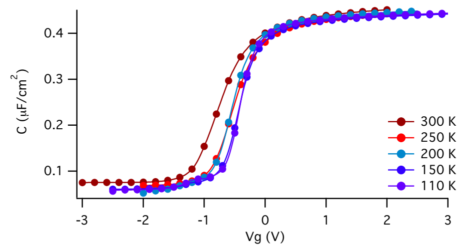

Figure 4.39: High frequency $C-V$ curves at different temperatures. Sample: *G1n*; ac frequency: 1 MHz.

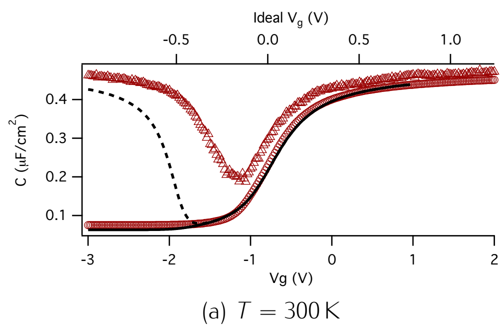

(a) $T = 300\,\text{K}$

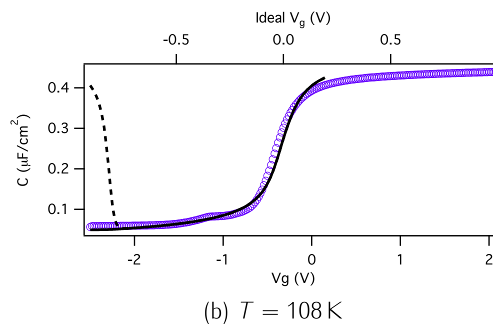

(b) $T = 108\,\text{K}$

Figure 4.40: Comparison between ideal and experimental $C-V$ curves of sample *G1n*. Experimental data measured using 1 MHz and 50 Hz ac modulation frequency are displayed with circles and triangles, respectively. Ideal curves in the high and low frequency limits, represented as solid and dashed lines respectively, are simulated using the best estimate values of $C_{ox} = 0.48\,\mu\text{F/cm}^2$ and $N_A = 1.8 \cdot 10^{16}\,\text{cm}^{-3}$. Notice the different scale of the abscissa axis in the ideal (top) and experimental (bottom) case necessary to match the $C-V$.

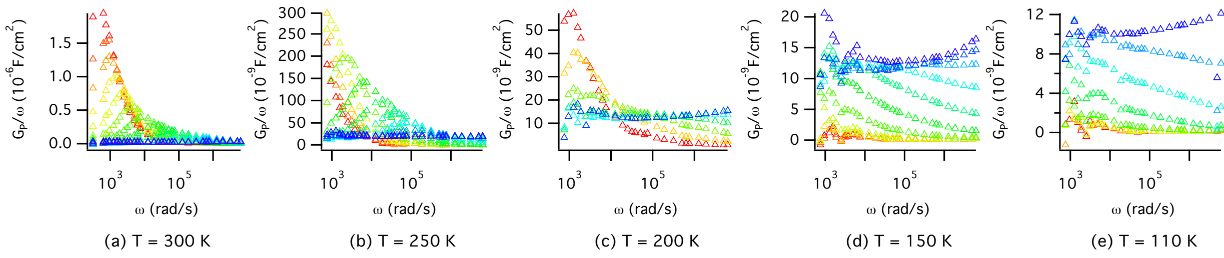

Figure 4.41: $G_P/\omega - \omega$ plots in depletion regime, for different values of V_g, sample *G1n*. In contrast to sample *G0p* and *G1p*, the curves do not show a maximum as a function of ω, except at room temperature where the peak is due to minority response in inversion. Measurements at different temperatures: (a) room temperature, (b) 250 K, (c) 207 K, (c) 150 K, (e) 108 K.

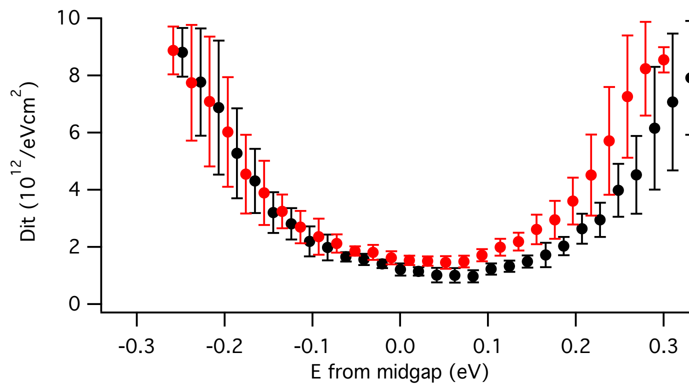

Figure 4.42: D_{it} distribution inside the bandgap obtained with capacitance methods, sample *G1n*. D_{it} from LF method (red) and HF/LF method (black) are in excellent agreement, well within experimental accuracy.

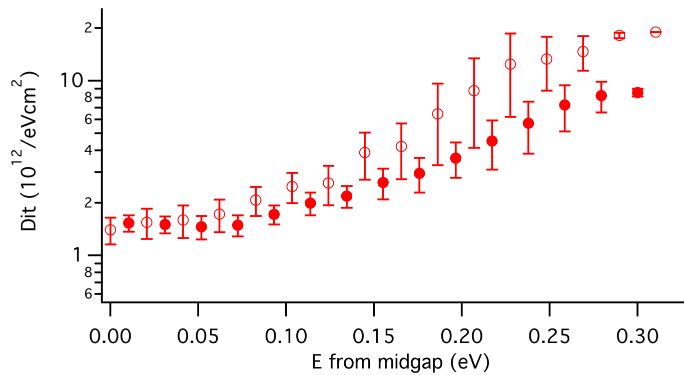

Figure 4.43: Resume of D_{it} distributions in the upper half of the bandgap obtained with LF capacitance method, in *n*-type samples. The (111) surface (filled circles) shows a smaller D_{it} than the (001) surface (outlined circles). This contrasts the results in *p*-type samples, where the (111) surface is more defective. HF/LF method is consistent with LF method at both surfaces, and it is omitted for clarity.

4.5 Comparative Analysis

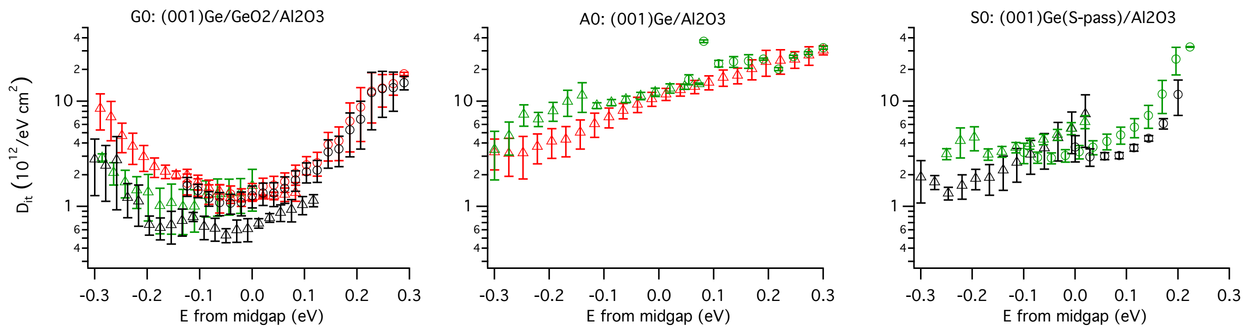

Figure 4.44: Overview of the D_{it} extracted from admittance spectroscopy of Ge/GeO$_2$ (left), Ge/Al$_2$O$_3$ (center), and Ge(S-passivated)/Al$_2$O$_3$ (001) oriented interfaces. Results from conductance (green), LF (red) and HF/LF (black) methods are shown. Data obtained with *p*-type substrates are indicated by triangles, while data obtained with *n*-type substrates are indicated by circles.

Aside the admittance spectroscopy measurement on the Ge/GeO$_2$ interface (series *G* samples), the $C - V$ and $G - \omega$ characteristics of series *A* and *S* samples have been examined, by the same procedure. The interface quality of the Ge/Al$_2$O$_3$ is sensibly lower, as expressed by D_{it} as a function of energy, especially around midgap and at the CB edge. The ammonium sulfide treatment prior to the deposition of the alumina layer proves to be effective in reducing D_{it} over the whole bandgap. Even though the comparatively low D_{it} specific of the Ge/GeO$_2$ interface are not reproduced, especially at midgap, the treatment is promising.
Approaching the regime $D_{it} \gtrsim q^2 C_{ox}$, the results of the conductance method must be regarded only as qualitative indications, and, in the same way, the extraction of the $\psi_S - V_g$ relationship is affected by a large uncertainty (Martens et al., 2008). Fig. 4.44 shows a comparative view on the interface trap density resulting from the admittance spectroscopy investigation of samples *G0p*, *G0n*, *A0p*, *A0n*, *S0p*, and *S0n*. The (111) oriented interfaces perform very similarly to the (001) oriented interfaces.

4.6 Bibliography

E. Burstein, G. Picus, B. Henvis, and R. Wallis. Absorption spectra of impurities in silicon-I. *Journal of Physics and Chemistry of Solids*, 1(1-2):65–74, September 1956. ISSN 00223697. doi: 10.1016/0022-3697(56)90012-9. URL http://www.sciencedirect.com/science/article/pii/0022369756900129.

S. Charles Baber. Net and total shallow impurity analysis of silicon by low temperature fourier transform infrared spectroscopy. *Thin Solid Films*, 72(1):201–210, September 1980. ISSN 00406090. doi: 10.1016/0040-6090(80)90575-1. URL http://www.sciencedirect.com/science/article/pii/0040609080905751.

B. E. Deal, A. S. Grove, E. H. Snow, and C. T. Sah. Observation of Impurity Redistribution During Thermal Oxidation of Silicon Using the MOS Structure. *Journal of The Electrochemical Society*, 112(3):308, March 1965. ISSN 00134651. doi: 10.1149/1.2423529. URL http://jes.ecsdl.org/content/112/3/308.abstract.

A. Dimoulas, G. Vellianitis, G. Mavrou, E. K. Evangelou, and A. Sotiropoulos. Intrinsic carrier effects in HfO2-Ge metal-insulator-semiconductor capacitors. *Applied Physics Letters*, 86(22):223507, May 2005. ISSN 00036951. doi: 10.1063/1.1944227. URL http://scitation.aip.org/content/aip/journal/apl/86/22/10.1063/1.1944227.

S. B. Felch. Comparison of different analytical techniques in measuring the surface region of ultrashallow doping profiles. *Journal of Vacuum Science & Technology B: Microelectronics and Nanometer Structures*, 14(1):336, January 1996. ISSN 0734211X. doi: 10.1116/1.588471. URL http://scitation.aip.org/content/avs/journal/jvstb/14/1/10.1116/1.588471.

Tyler J. Grassman, Sarah R. Bishop, and Andrew C. Kummel. An atomic view of Fermi level pinning of Ge(100) by O2. *Surface Science*, 602(14):2373–2381, July 2008. ISSN 00396028. doi: 10.1016/j.susc.2008.05.019. URL http://linkinghub.elsevier.com/retrieve/pii/S0039602808003002.

S. Kar. Extraction of the capacitance of ultrathin high-K gate dielectrics. *IEEE Transactions on Electron Devices*, 50(10):2112–2119, October 2003. ISSN 0018-9383. doi: 10.1109/TED.2003.817271. URL http://ieeexplore.ieee.org/lpdocs/epic03/wrapper.htm?arnumber=1232931.

R.D. Larrabee and W.R. Thurber. Theory and application of a two-layer Hall technique. *IEEE Transactions on Electron Devices*, 27(1):32–36, January 1980. ISSN 0018-9383. doi: 10.1109/T-ED.1980.19815. URL http://ieeexplore.ieee.org/lpdocs/epic03/wrapper.htm?arnumber=1480608.

Koen Martens, Chi On Chui, Guy Brammertz, Brice De Jaeger, Duygu Kuzum, Marc Meuris, Marc Heyns, Tejas Krishnamohan, Krishna Saraswat, Herman E. Maes, and Guido Groeseneken. On the Correct Extraction of Interface Trap Density of MOS Devices With High-Mobility Semiconductor Substrates. *IEEE Transactions on Electron Devices*, 55(2):547–556, February 2008. ISSN 0018-9383. doi: 10.1109/TED.2007.912365. URL http://ieeexplore.ieee.org/lpdocs/epic03/wrapper.htm?arnumber=4436002.

E.H. Nicollian and J.R. Brews. *MOS (Metal Oxide Semiconductor) Physics and Technology*. A Wiley-Interscience publication. Wiley, 2003. ISBN 9780471430797. URL http://books.google.it/books?id=HaRwngEACAAJ.

E.H. Nicollian and A. Goetzberger. Lateral AC current flow model for metal-insulator-semiconductor capacitors. *IEEE Transactions on Electron Devices*, 12(3):108–117, March 1965. ISSN 0018-9383. doi: 10.1109/T-ED.1965.15465. URL http://ieeexplore.ieee.org/lpdocs/epic03/wrapper.htm?arnumber=1473929.

G. Picus, E. Burstein, and B. Henvis. Absorption spectra of impurities in silicon-II. *Journal of Physics and Chemistry of Solids*, 1(1-2):75–81, September 1956. ISSN 00223697. doi: 10.1016/0022-3697(56)90013-0. URL http://www.sciencedirect.com/science/article/pii/0022369756900130.

J. Shappir, A. Kolodny, and Y. Shacham-Diamand. Diffusion profiling using the graded C(V) method. *IEEE Transactions on Electron Devices*, 27(5):993–995, May 1980. ISSN 0018-9383. doi: 10.1109/T-ED.1980.19970. URL http://ieeexplore.ieee.org/lpdocs/epic03/wrapper.htm?arnumber=1480763.

J.G. Simmons and L.S. Wei. Theory of dynamic charge and capacitance characteristics in MIS systems containing discrete surface traps. *Solid-State Electronics*, 16(1):43–52, January 1973. ISSN 00381101. doi: 10.1016/0038-1101(73)90124-X. URL http://www.sciencedirect.com/science/article/pii/003811017390124X.

Michio Tajima. Determination of boron and phosphorus concentration in silicon by photoluminescence analysis. *Applied Physics Letters*, 32(11):719, August 1978. ISSN 00036951. doi: 10.1063/1.89897. URL http://scitation.aip.org/content/aip/journal/apl/32/11/10.1063/1.89897.

L.S. Wei and J.G. Simmons. Effect of temperature and voltage sweep rate on characteristics of MIS capacitors. *Solid-State Electronics*, 17(10):1021–1028, October 1974. ISSN 00381101. doi: 10.1016/0038-1101(74)90141-5. URL http://www.sciencedirect.com/science/article/pii/0038110174901415.

Y. Zohta. Rapid determination of semiconductor doping profiles in MOS structures. *Solid-State Electronics*, 16(1):124–126, January 1973. ISSN 00381101. doi: 10.1016/0038-1101(73)90134-2. URL http://www.sciencedirect.com/science/article/pii/0038110173901342.

Discussion on the Nature of the Ge Interface Centers 5

Jacke: I HAVE SEEN THE LIGHT
The blues brothers – 1980

The experimental observation of the centers at germanium – oxide interfaces, following the EDMR and admittance characterization, which were presented in chapter 3 and 4, respectively, are compared with the outcomes of analogous investigations of the silicon – oxide interfaces. The broad knowledge gathered about the Si/SiO_2 system is an invaluable guidance in the interpretation of nature of defects at the similar, but still potentially surprising, germanium surface.

5.1 Defects at the Silicon Interface

Defects at the Si/SiO_2 interface have been the subject of many studies in the last decades, in view of their relevance in the operation of MOS-based devices. Admittance spectroscopy has been developed mainly to address the study of interface traps in silicon. Many textbooks describe the technological and scientific efforts that culminate in the realization and characterization of almost perfect interfaces with charge density below the $10^{10}\,\text{cm}^{-2}$ level, that is less than one defect in ten thousand atoms at the interface (Sze and Ng, 2006; Schroder, 2006; Nicollian and Brews, 2003). Fundamental contributions also came in from different characterization techniques. The nature of interface centers has been unraveled with the aid of electrical techniques such as Deep Level Transient Spectroscopy (DLTS) (Dobaczewski et al., 2008), conventional resonance EPR spectroscopy (Poindexter et al., 1981; Brower, 1986; Stesmans and Afanas'ev, 1998), pulsed EDMR spectroscopy (Hoehne et al., 2011), and positron annihilation spectroscopy (Asoka-Kumar et al., 1994). Theoretical calculations had a primary role, as well, in describing the atomistic details of the electrically active centers (Pasquarello et al., 1998; Stirling et al., 2000).

The long-standing investigations indicate that the prevalent defects occurring at the Si/SiO_2 interface are unsaturated dangling bonds (DBs). Due to the paramagnetic nature of these defects, EPR spectroscopy plays a leading role revealing the microscopic structures and the passivation behavior. The dangling bond observed at the (111) oriented surface is called P_b center and it is sketched in Fig. 5.1. The g-factor matrix is extracted from the experimental values of the g-factor as a function of the orientation of the external magnetic

field (also called *angular map*), shown in Fig. 5.3a. The angular map indicates a trigonal symmetry and, together with the information provided by the hyperfine coupling, these evidences identify the P_b center as a sp^3 orbital in a •Si≡Si$_3$ structure pointing along the [111] direction, orthogonal to the interface. The defect originates from the mismatch between the silicon crystal lattice and the amorphous oxide (Poindexter et al., 1981; Brower, 1986).

Two different centers are present at the (001) oriented surface. The more abundant DB, conventionally denoted as P_{b0}, shares with the P_b center an axial symmetry, with principal axis oriented along the [111] direction. Pulsed EDMR spectroscopy revealed only recently its location at a monolayer step with a dimerized upper part (Hoehne et al., 2011), shown in Fig. 5.2a. Such steps are always likely to occur in extended surfaces, due to surface roughness or slight off-axis cut. The other center is commonly referred to as P_{b1} and it is distinguished by a lower, monoclinic-*I*, symmetry. A first-neighbor oxygen atom was initially supposed to explain the distorted structure, but no contribution from the nuclear spin of ^{17}O was observed. Successive EPR measurements of the full hyperfine structure evidenced a distorted bond as the origin of the lower symmetry (Stesmans et al., 1998a,b), and theoretical calculations disclosed the presence of asymmetrically oxidized dimers in the transition region between silicon and its oxide (Stirling et al., 2000). The currently accepted model for P_{b1} is shown in Fig. 5.2b. The angular maps of the g-factor of the P_{b0} and of the P_{b1} are shown in Fig. 5.3b and 5.3c, respectively. At the (110) surface a DB with the same properties of the P_{b0} is found out (Keunen et al., 2011).

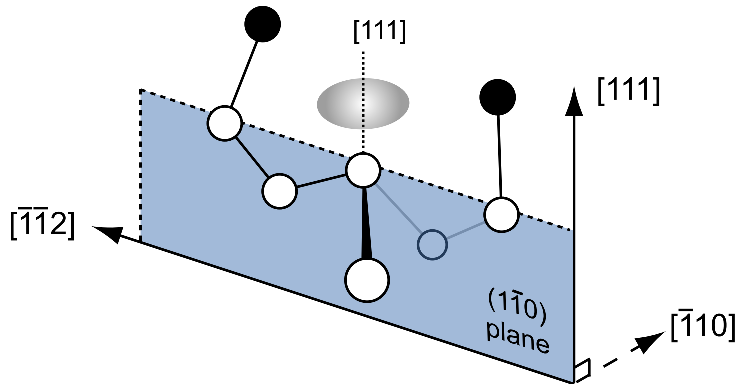

Figure 5.1: Schematic picture of the currently accepted dangling bond microstructure at the (111) oriented Si/SiO$_2$ interface. This center is called P_b and it is characterized by trigonal symmetry with principal axis oriented into the [111] direction. Open circles represent Si atoms, filled circles represent O atoms, and the DB is sketched by the shaded ellipsoid.

The salient EPR characteristics of the P_b-type centers are summarized in Table 5.1. Generally, resonance features such as g-matrix and line width depend on the oxidation condition, with temperature playing a decisive role because of the relevance of the strain in the formation of the DB center. Quantitative comparison among the different surface orientations shows a direct correlation between signal intensity and an effective areal atom density (defined as the density of interface atoms divided by the number of bonds

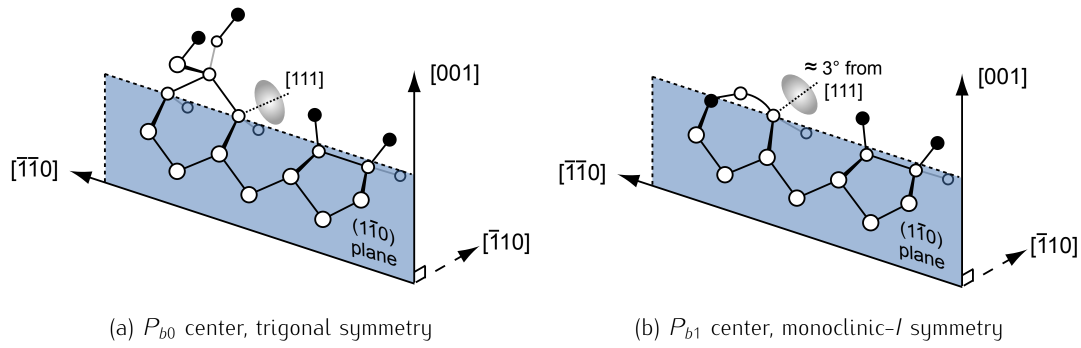

(a) P_{b0} center, trigonal symmetry (b) P_{b1} center, monoclinic-I symmetry

Figure 5.2: Schematic picture of the currently accepted dangling bond microstructure at the (001) oriented Si/SiO_2 interface. Two different centers are distinguished. The more abundant P_{b0} (left) recalls the features of the P_b center observed at the (111) oriented interface, but the configuration of the neighboring atoms is different. On the other hand, the P_{b1} (right) has a different point symmetry and according to the asymmetrically oxidized dimer model it features a distorted dimer configuration, after Stirling et al. (2000). Open circles represent Si atoms, filled circles represent O atoms, and the DB is sketched by the shaded ellipsoid as in Fig. 5.1.

center	$g_{//}$	$g_\perp$	$\sigma g_\perp$
P_b	2.00136 ± 0.00003	2.0088 ± 0.0001	0.0009 ± 0.0001
P_{b0}	2.00185 ± 0.0001	2.0081 ± 0.0001	0.0009 ± 0.00005
P_{b1}	$g_3 = 2.0022 \pm 0.0001$	$g_2 = 2.00735 \pm 0.0001$	//
		$g_1 = 2.0057 \pm 0.0001$	

Table 5.1: The salient EPR characteristics of P_b-type centers at the Si/SiO_2 interface (Stesmans and Afanas'ev, 1998). The principal values $g_{//}$ and $g_\perp$ are reported for the trigonal P_b and P_{b0} centers, observed when $\mathbf{B}//[111]$, and $\mathbf{B} \perp [111]$, respectively. For the monoclinic-I P_{b1} are shown the principal values g_1, g_2, g_3, observed when $\mathbf{B}$ is oriented along $[\bar{1}\bar{1}0]$, $3° \pm 1°$ off from [111], and $3° \pm 1°$ off from $[2\bar{1}\bar{1}]$, respectively. The stress induced g-factor spread $\sigma g_\perp$, as defined by Brower (1986) is also included.

oriented toward the oxide).

Admittance spectroscopy makes evidences of the electrical properties of the DBs. Fig. 5.4 is indicative of a twofold structure, with peaks at energies 0.26 eV and 0.84 eV above the VB edge, responsible for the electron trapping in MOS devices. These peaks were correlated by Poindexter et al. (1984) to the P_b resonance observed by EPR spectroscopy in a large area MOS capacitor made on a (111) Si substrate. The intensity of the EPR signal A, shown in Fig. 5.5, is proportional to the number of paramagnetic P_b states and the areal density of such states throughout the gap is the absolute value of the derivative $\mathrm{d}A/\mathrm{d}E$. The two figures are interpreted as follows: In the lower half of the gap, one electron is added to the DB as the chemical potential is raised. The center exhibits a donor character as it goes from a positive to a neutral state (+/0 transition), giving rise to a peak in the D_{it} and becoming paramagnetic. In the upper half of the gap, another electron is added when the chemical potential increases sufficiently toward the CB. Then,

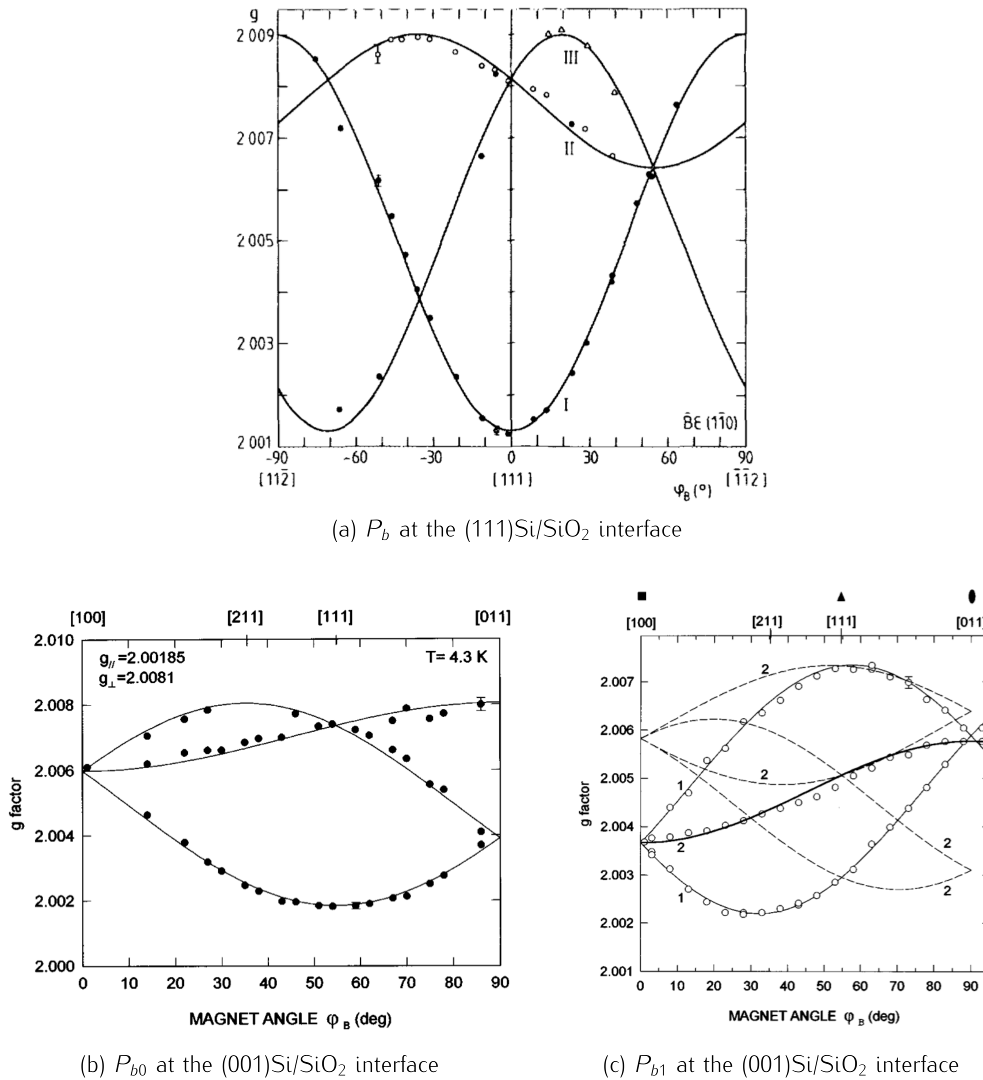

(a) P_b at the (111)Si/SiO_2 interface

(b) P_{b0} at the (001)Si/SiO_2 interface

(c) P_{b1} at the (001)Si/SiO_2 interface

Figure 5.3: g-values as a function of the orientation of the external magnetic field **B** for the three paramagnetic silicon dangling bond structures, identified at the Si/SiO_2 interfaces. (a) After Stesmans (1986). (b) and (c) after Stesmans and Afanas'ev (1998).

the center behaves as an acceptor state as it goes from neutral to negatively charged (0/– transition) giving rise to another peak in the D_{it} and returning diamagnetic. The transition is not sharp and the substantial peak width (about 0.1 eV) is associated with the variable interface environment, where the local stress and the uneven distribution of charges affect each P_b center in a different way. These results are further confirmed by DLTS measurements (Dobaczewski et al., 2008) and are at present unquestioned.

In summary, both spin resonance and electrical spectroscopies coherently recognize the DBs as the prevailing defects at the Si/SiO_2 interface, which take their origin from the strain release due to the mismatch between the crystalline substrate and the amorphous oxide. The number of P_b-type defects is related to the degree of relaxation of the SiO_2 structure and the number of available bonds. The DB has three charge states: the

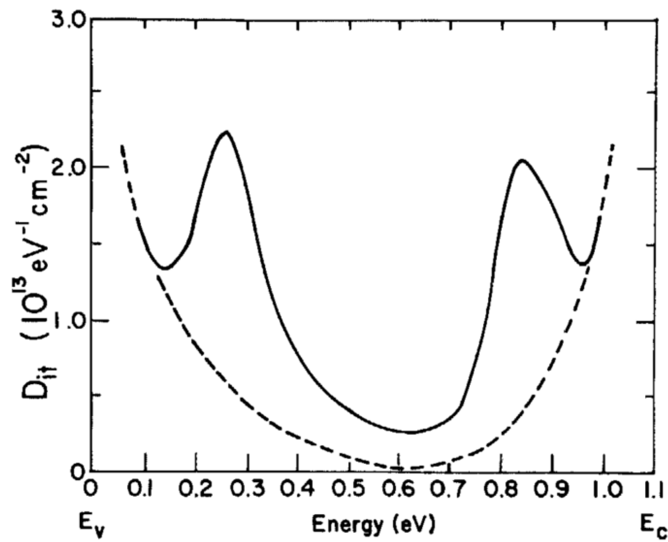

Figure 5.4: D_{it} distribution in the bandgap extracted in as-oxidized (111) oriented p-type silicon MOS. The contribution of DBs is visualized as the difference between the observed D_{it} (solid line) and the extrapolated continuum background (dashed line). After Poindexter et al. (1984).

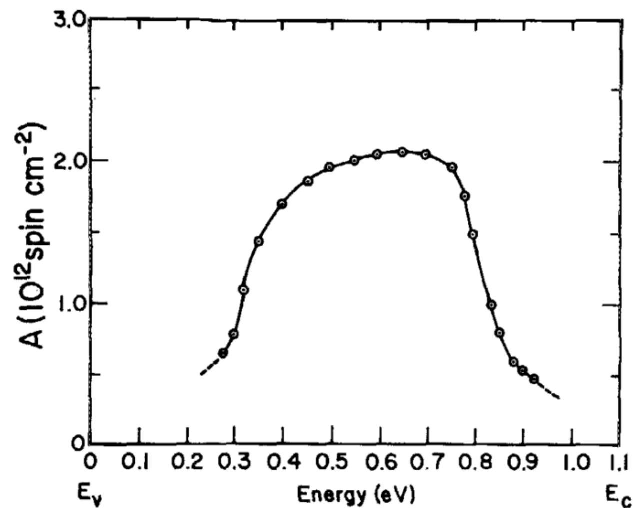

Figure 5.5: EPR intensity A as a function of the position of the chemical potential within the bandgap, for the same sample of Fig. 5.4. Only paramagnetic centers contribute to the EPR signal and the plot indicates that the transitions to diamagnetic states occur at 0.26 eV and 0.84 eV above the VB edge. Therefore, the density of energy states is obtained as dA/dE and compares directly with Fig. 5.4. After Poindexter et al. (1984).

paramagnetic neutral state, and two diamagnetic states (positive and negative charged state).

A last feature of the P_b-type defects at the interface between silicon and silicon oxide is the possibility to passivate it with hydrogen. The importance of this characteristic for the semiconductor industry can hardly be overestimated, as it enabled the fabrication of high performance devices with interface charge density below 10^{10} eV^{-1}cm^{-2}.

5.2 Experimental Observations at the Germanium Interface

One may reasonably expect that Ge interface centers would resemble the Si ones as due to the structural similarity between the two group IV semiconductor surfaces. However, this is not the case.

First, conventional EPR did not evidence any paramagnetic center consistent with a dangling bond residing at the Ge/GeO_2 interface. After extensive investigations with a sensitivity better than 10^{12} eV^{-1}cm^{-2}, no clues of the equivalent Ge-P_b centers have been found in planar interfaces, (Afanas'ev et al., 2005). At the interface with amorphous oxidized Ge, broad signals with g-factors in the range of interest have been observed (Graf et al., 2003), but the absence of crystalline order hinders the determination of the g-matrix. In other Ge interfaces, such as the (111)Ge/epi-Ge_3N_4, signals are related to •Ge≡X structures (Nguyen et al., 2010), but X differs from Ge_3. These kind of DBs are present at the interface between SiGe alloys and oxide (Zvanut and Carlos, 1992; Lebib et al., 1997; Stesmans et al., 2009; Somers et al., 2012), but the resonances disappear as the Ge fraction is increased above 80% (Fanciulli et al., 2005).

Even admittance spectroscopy failed in revealing prominent features in the D_{it} in Ge MOS or MOSFET devices, despite the overwhelming abundance of literature reporting on many different processes, employing many different insulators and many surface treatments (Chui et al., 2002; Afanas'ev et al., 2005; Kamata, 2008; Kuzum et al., 2009; Sasada et al., 2009; Bellenger et al., 2010; Molle et al., 2011; Sioncke et al., 2011; Swaminathan et al., 2010; Zhang et al., 2011; Lee et al., 2012; Murad et al., 2012; Wang et al., 2012; Kasahara et al., 2014). The observed D_{it} as a function of energy displays a regular, featureless U shape recalling that of the continuum background due to tail band states observed in silicon.

Interpretation of Electrically Detected Magnetic Resonance Data

The first experimental evidence of P_b-like dangling bonds at the interface between germanium and germanium oxide has been reported by Baldovino et al. (2008), as described thoroughly in the present work (see chapter 3.1). Due to the specific features of the EDMR spectroscopy, that work establishes the presence of paramagnetic centers and their electrical activity at the (001)Ge/GeO_2 interface. Nonetheless, the energy positioning within the bandgap and a clear microstructure determination are still lacking, together with a quantitative determination of the density of centers per unit area.

New EDMR data concerning the (111)Ge interfaces (see chapter 3.2) confirm the presence of electrically active and paramagnetic DBs levels, located at the interface (Paleari et al., 2013, 2014). At the (111) oriented surface, however, it is possible to recognize a trigonal symmetry marking a sharp difference with the DBs at the (001) surface oxidized in the same condition. The role of the surface orientation is not trivial and a possible interpretation necessarily invokes the comparison with the Si/SiO_2 interface.
Silicon and germanium exposing the (111) surface are quite similar: both semiconductors present a prominent axially symmetrical center formed to accommodate the structural mismatch between the crystal lattice and the amorphous oxide. EPR and EDMR spectroscopies, indeed, reveal homogeneous features suggesting the structure depicted in Fig. 5.1 as a possible model for the Ge P_b defect.
On the other hand, by looking at the (001) surface, the differences between the oxidized Si and Ge can be rationalized in terms of trigonal, P_{b0}-like, and non-trigonal, P_{b1}-like, centers. With the aid of Fig. 5.2a and Fig. 5.2b, it can be noticed that the first is oriented into the [111] direction, corresponding to the orientation of the sp^3 bonds, and the second is tilted off from the $[2\bar{1}\bar{1}]$, which is not a regular bond direction. While they are both present in Si (with a prevalence of the P_{b0}), only non-trigonal DBs can be observed in Ge.

As above-mentioned, the distortion introduced in the DB wave function by strained bonds in the close neighborhood of the center is responsible for the lower symmetry of the non-trigonal center (Stirling et al., 2000). In turn, the strained bond is formed upon asymmetrical oxidation of dimer structures existing in the suboxide region. Actually, both Si and Ge oxide free (001) surfaces reconstruct in dimers with a dominance of (2×1) periodicity. Ge is more thermodynamically prone to form asymmetric dimers – $c(4 \times 2)$ or $p(2 \times 2)$ reconstructions – due to bond buckling even at room temperature (Gurlu et al., 2004; Zandvliet, 2003), while Si exhibits stable buckled structures only in correspondence with steps and defects or at low temperatures (Zandvliet, 2000; Bokes et al., 2002). At least in the case of Si, this tendency is retained even at the oxidized subinterface, where a transition layer is responsible for dimer reconstruction at the buried interface (Pasquarello et al., 1998). A similar mechanism in Ge could be responsible for the non-trigonal structure observed at the (001) surface: the partial subinterface reconstruction may promote the backbond oxidation at dimer sites.

Moreover, the absence of the trigonal P_{b0}-like counterpart could be tentatively explained in terms of surface relaxation argument (Paleari et al., 2013). As discussed at the beginning of the chapter, the Si P_{b0} is located at a monolayer step with a dimerized upper part (see Fig. 5.2b). This DB structure could be mainly suppressed in Ge, because of the higher viscosity of the GeO_2 compared to the SiO_2 (Houssa et al., 2008). The softer germanium oxide could then allow stress relaxation, reducing the number of broken bonds at monolayer steps.

Interpretation of Admittance Spectroscopy Data

The analysis of the admittance spectroscopy data obtained in Ge MOS capacitors and described in detail in chapter 2.3 are in line with the present literature. D_{it} ranges from $\approx 10^{12}\,\mathrm{eV^{-1}cm^{-2}}$ at midgap to $\approx 10^{13}\,\mathrm{eV^{-1}cm^{-2}}$ close to the band edges in the samples with thermal GeO_2, in a smooth U shape. The distinctive features of the DBs observed in silicon are not visible, even though EDMR reveals both the presence and the electrical activity of P_b-like centers.

But, this does not necessarily mean that the contribution of these paramagnetic centers is negligible for the overall D_{it}.
By looking back at the results of the conductance method, it can be noticed that the characteristic response time for the holes displays an anomalous behavior shown in Fig. 5.6. According to Eq. 1.62, τ is expected to vary as $\sim \exp v_S$ at fixed T, with v_s being the

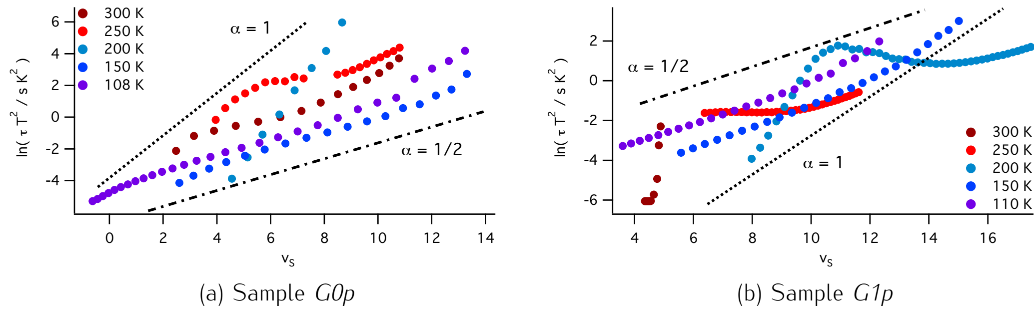

(a) Sample *G0p*

(b) Sample *G1p*

Figure 5.6: Hole characteristic time as a function of the distance in energy from trap level to VB edge in p-type (001)Ge/GeO_2 (right) and p-type (111)Ge/GeO_2 (left) MOS capacitor. The experimental points are color coded according to the measurement temperature, as shown in the legend, and are obtained from the same fittings described in chapter 2.3, in the same range of V_g and ω. The y-axis is rescaled according to $\ln T^2$ to facilitate the comparison between data at different temperatures. The parameter α is defined in Eq. 5.1 and can be regarded as the slope in the $\ln \tau - v_S$ diagram. The straight dotted and dashed lines, corresponding to $\alpha = 1$ and $\alpha = 1/2$, respectively, are shown as guides to the eye.

band bending induced by applied bias to the MOS capacitor. In p-type Ge/GeO_2 MOS capacitors a different dependence is observed, described by a more general expression

$$\tau_p \sim \exp \alpha v_S \tag{5.1}$$

where the additional parameter α is introduced. α is the slope of the $\tau - v_S$ relationship on a log scale and can be readily visualized by rewriting Eq. 1.62 through Eq. 4.3

$$\tau_p \sim \exp \alpha \left(\mu - E_V\right) \tag{5.2}$$

where α is representative of the shift in the chemical potential required to activate the emission process. As discussed in chapter 1.1, in order to leave the VB and be captured in a trap, the electron needs to overcome a barrier amounting to the difference between the top of the VB (the reservoir of electrons) and the energy level of the trap E_T. Since only traps that satisfy $E_T \approx \mu$ contribute to the admittance signal, a shift of the chemical potential should result in exactly the same change of energy necessary to activate the trapping process. Therefore, α equals strictly unity.
Fig. 5.6 shows that at low temperatures and at energies below 0.2 eV from the VB, α is very close to 1/2. In this energy range, therefore, the process is activated by half of the energy distance between the level of the trap and the top of the VB. In other words, two carriers are trapped or emitted at the same time. Outside this energy range, at $T > 200\,\text{K}$, it is not possible to establish a clear trend due to the influence of minority carrier response when approaching the weak inversion regime (Martens et al., 2008).

Instead, data at low temperatures taken from different samples are coherent and can be readily interpolated, as shown in Fig. 5.7. Fitting yields $\alpha = 0.56 \pm 0.04$, in excellent

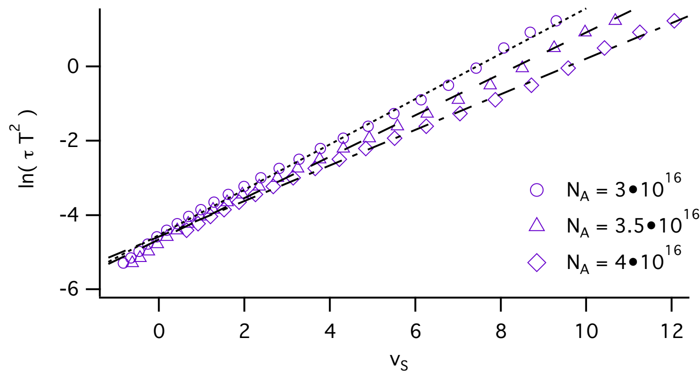

Figure 5.7: Average hole characteristic time τ_p as a function of dimensionless surface band bending v_S, observed in sample *G0p* at 108 K. The three curves are the best estimate (center) and upper and lower bounds of the confidence interval resulting from experimental errors in the determination of the $v_S - V_g$ relationship. Linear fitting to the data yields an angular coefficient $\alpha = 0.56 \pm 0.04$.

agreement with the *ansatz* $\alpha = 1/2$.

The robustness of the estimate of the parameter α is bound to the uncertainty in the $V_g - v_S$ relationship, and hence to the accuracy of the N_A determination as already described in chapter 2.3. By varying N_A arbitrarily, it is possible to push α closer or farther from unity, as shown in Fig. 5.8. For each value of N_A, the ideal $C - V$ curve is simulated and used to extract the $V_g - v_S$ relationship. Then, $\ln \tau$ is plotted against v_S and fitted by a straight line, obtaining the slope α.

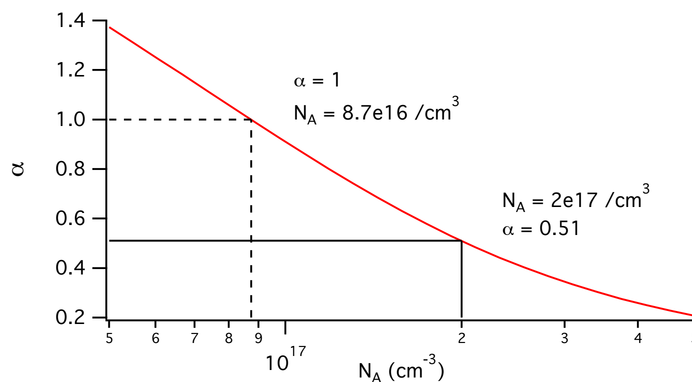

Figure 5.8: Parameter α as a function of the substrate doping level N_A, sample *G1p*, $T = 108$ K. The uncertainty in substrate doping level propagates to the slope of the $\tau - v_S$ relationship through the $\psi_S - V_g$ curve (Eq. 2.9). The best estimate from Max-min capacitance is $N_A = 2.0 \cdot 10^{17}$, resulting in $\alpha \approx 1/2$ (see Fig. 5.7). The doping level needed to resort to the regular exponent $\alpha = 1$ leads to unphysical MOS characteristics.

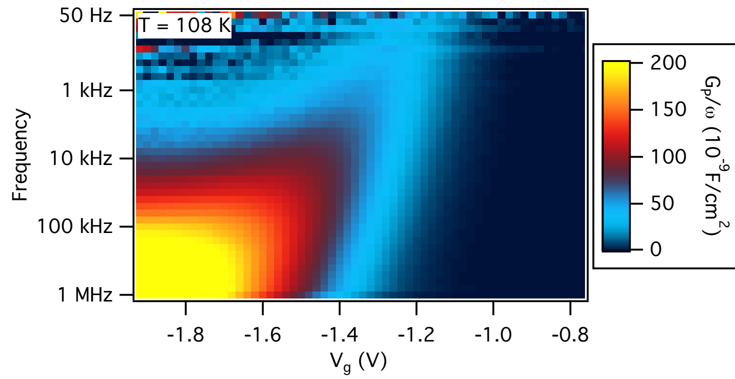

Figure 5.9: 2D map showing G_P/ω as a function of V_g (x-axis) and frequency $\omega/2\pi$ (y-axis), sample *G0p*, $T = 108\,\mathrm{K}$. Conductance peaks lie on a path that satisfies $\omega_p \tau(V_g) \approx 1$.

Two options can be taken into account:

1) If N_A is forced to match $\alpha = 1$, unrealistic MOS characteristics are obtained. This is better visualized by considering the two dimensional representation of conductance data. G_P/ω is a function of both V_g and ω with maxima extended on a path that satisfies $\omega_p \tau_p(V_g; \sigma_p, T) \approx 1$, namely, conductance maxima occur when the modulation frequency matches the characteristic time of the traps. The characteristic time is, in turn, a function of the energy positioning and the capture cross section. This is shown in Fig. 5.9. A convenient diagram, shown below in Fig. 5.10, is obtained by rescaling the frequency axis to read the capture cross section by the relationship

$$\sigma_p = \frac{\omega}{T^2 \times 1.09 \cdot 10^{21}\,\mathrm{cm^{-2}s^{-1}K^{-2}}} \exp\left(\frac{q\phi_S - E_V}{k_B T}\right) \tag{5.3}$$

and the V_g axis can be replaced by the distance from VB edge. With this prescription, the conductance is made independent from the measurement conditions (i.e. T and V_g) and reflects only the properties of the interface trap actually probed, namely D_{it} (color scale) as a function of energy (x-axis) and capture cross section (y-axis). It follows that the conductance maps at different temperatures must overlap, provided that σ_p is not strongly dependent on T. Fig. 5.10 collects the maps obtained at different temperatures, for sample *G1p*. When N_A is arbitrarily fixed so as to yield $\alpha = 1$ (left), the overlap is comparatively poorer and, more significantly, the minority carrier response (evidenced by the huge increase in conductance) is found well within the depletion regime. This is not a physically realistic situation, because minority carriers come into play only when midgap is crossed.

2) By taking N_A obtained from Max-min capacitance method, maps overlap smoothly and the minority carrier response is observed at energies above midgap, as expected. Then $\alpha = 1/2$ results and τ shows a discrepancy from the regular v_S dependence beyond the experimental errors that cannot be attributed to artifacts. Data indicate that two carriers are involved in the trapping and emission events investigated by admittance spectroscopy. This behavior is a characteristic of negative-$\mathcal{U}$ centers (Look, 1981), whose doubly occupied state is qualified by two energy levels, E_1 and E_2, with $E_2 < 2E_1$. The theoretical foundations and the implication of negative-$\mathcal{U}$ interface centers are reviewed in the next section. The hole capture cross section can be calculated again by taking into account the factor $\alpha = 1/2$. As shown in Fig. 5.11, the capture cross section is

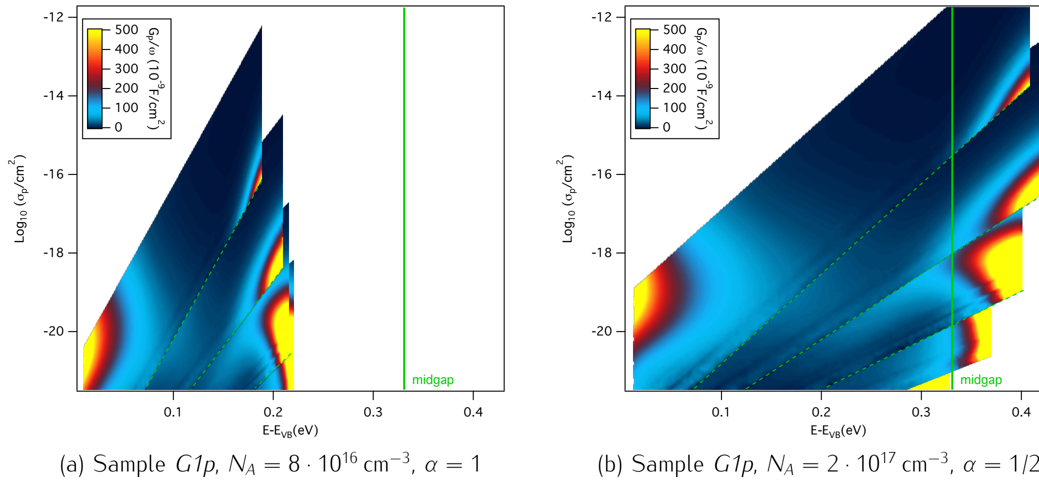

(a) Sample *G1p*, $N_A = 8 \cdot 10^{16}\,\mathrm{cm}^{-3}$, $\alpha = 1$ (b) Sample *G1p*, $N_A = 2 \cdot 10^{17}\,\mathrm{cm}^{-3}$, $\alpha = 1/2$

Figure 5.10: 2D conductance maps as a function of energy and capture cross section. Measurement temperatures are 110 K, 150 K, 200 K, 250 K, and 300 K, from top to bottom, respectively. In this diagram, maps are expected to overlap seamlessly, provided the capture cross section does not depend on temperature.

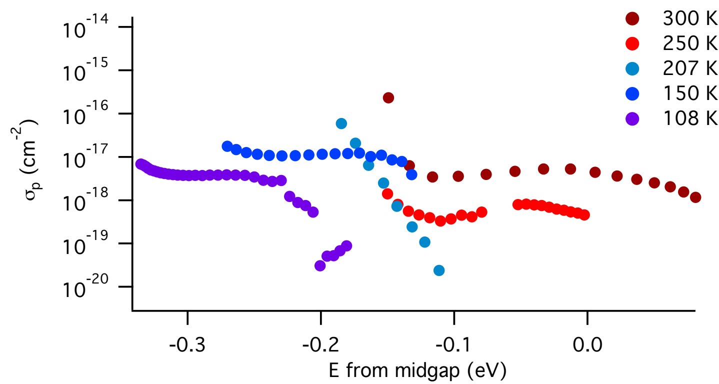

Figure 5.11: Hole capture cross section in sample *G0p*, according to a negative-$\mathcal{U}$ model.

homogeneous over the whole bandgap, as expected for trapping centers with the same structure, and is estimated $\sigma_p \approx 10^{17}\,\mathrm{cm}^2$.

5.3 The Negative-$\mathcal{U}$ Model for Interface Defects

In 1975 Anderson proposed the concept of a defect where the energy gain associated with electron pairing in an orbital, coupled with large lattice relaxation, might overcome the Coulomb repulsion between the two electrons. The net effective attractive interaction between the two electrons (which yields the name negative-$\mathcal{U}$) causes electrons to be trapped by pairs at the defect (Anderson, 1975). Baraff et al. (1980) predicted that the Jahn-Teller relaxation energy for the Si vacancy in the doubly occupied state might be large enough to overcome the repulsive energy between the electrons. Examples of this peculiar type of defect have been discovered in Si, notably the Si vacancy (V) and the boron interstitial (B_i) after the work of Watkins (1975) and Watkins and Troxell (1980).
The statistic of the negative-$\mathcal{U}$ centers is described by Eq. 1.15, where $E_2 < 2E_1$. As

described in chapter 1.1 when single electron transitions are involved, the term *energy level* denote a part of the energy difference between two states of the system composed of a defect and the reservoir. The total energy change is $E_l - \mu$. It is convenient to be more explicit, by speaking in terms of *occupancy level* $E(n/n+1)$, *i.e.* the energy level at which the transition from n to $n+1$ charge occurs. In this case, the energy change of the double electron state is $2E(n/n+2) - 2\mu$.

Since the deduced statistic of the Ge interface traps is consistent with the electrical activity of a double electron state, it is reasonable to wonder if defects with a negative-$\mathcal{U}$ character may set in at the interface between Ge and Ge oxide. To scrutinize this surmise, we first examine the DB center in Si furthermore. In Si, DBs exist in three distinct charge state: positive, neutral and negative. By increasing the chemical potential, two levels are crossed, the $E(-/0)$ first, then the $E(0/+)$, as was gleaned from Fig. 5.4 and Fig. 5.5. The three charge states are thermodynamically stable and which one can be observed depends on the position of the chemical potential.
In negative-$\mathcal{U}$ centers, on the other hand, two carriers are involved in the transition and the intermediate charge state is missed out. In other words, only one occupancy level manifests: $E(+/-)$. In a negative-$\mathcal{U}$ DB model, only two charge states are thermodynamically stable, namely the positive DB^+ and the negative DB^- state. As a comparison, Fig. 5.12 displays the occupancy level structure for conventional and negative-$\mathcal{U}$ models of the DB. The neutral state DB^0 is not the ground state for any position of the chemical potential but it is a *metastable* state decaying through the reaction

$$2DB^0 \rightarrow DB^- + DB^+ \tag{5.4}$$

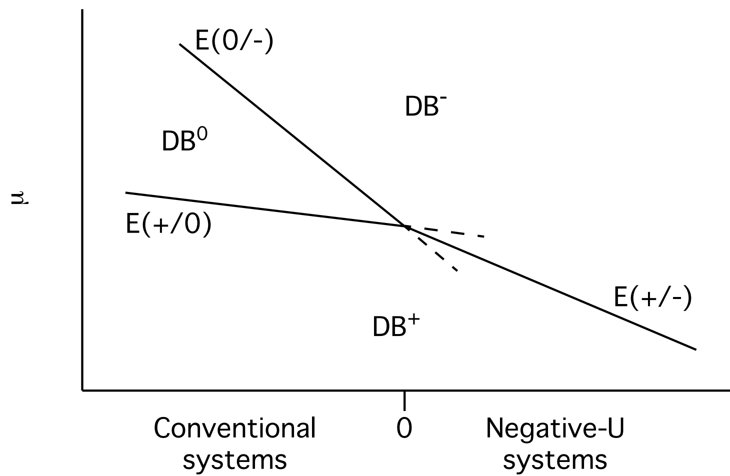

Figure 5.12: Occupancy level diagram for conventional and negative-$\mathcal{U}$ DB models. The region of stability of the DB^+, DB^0, and DB^- charge states are delimited by the occupancy levels, which are functions of the character of the center. Approaching the negative-$\mathcal{U}$ region from left, the region where DB^0 is the ground state shrinks and then disappears.

The negative-$\mathcal{U}$ character of the Ge DB has been investigated through theoretical modeling of the interface. The estimation of the energy levels requires detailed calcula-

tions based on density functional theory (DFT), first-principles computational approaches or molecular dynamics simulations. Replicating the DB structure at the interface is a difficult task. DBs occur in a variety of different configurations, the local chemical environment influences the electronic properties, and tail band states participate in the bond wave function. As pointed out by Houssa et al. (2011) and Binder et al. (2012), the Si/SiO_2 bonding pattern is not satisfactory to model the Ge interface because Ge—O bonds have reduced strength if compared to Si—O bonds. Therefore fully relaxed *ab initio* and molecular dynamics simulation are a prerequisite to access a full understanding of the Ge DB. The delicate nature of the matter is reflected in the diversity of the conclusion drawn by different studies. The location of the energy levels of the DB has been postulated below the VB (Weber et al., 2007; Broqvist et al., 2009), or within the bandgap (Broqvist et al., 2008; Binder et al., 2010), and the vacancy in Ge has been described either as a negative-$\mathcal{U}$ center (Weber et al., 2007) or as a positive-$\mathcal{U}$ center (Weber et al., 2013).

At present, the most accurate and solid model for the Ge DB at the interface between Ge and GeO_2 is described in the works by Broqvist et al. (2008, 2012), and Binder et al. (2010, 2012). The main features can be summarized as follows:

1. Energy levels exist within the bandgap of Ge.
2. The levels are located in the lower half of the bandgap:
   $E(+/0) = 0.05\,\text{eV}$ and $E(0/-) = 0.11\,\text{eV}$ above the VB edge.
3. The level distribution is broad due to the disorder at the interface. In Si the typical dispersion in the levels is evaluated in 0.1 eV (Poindexter et al., 1984), but in Ge it can be more pronounced due to the interaction with closer VB tail states.
4. Charging levels are affected by the local chemical environment. This may lead to additional broadening in charging level distribution, caused by the simultaneous occurrence of Ge, GeO_x, GeO_2 at the interface.

Si DBs are characterized by a neutral ground state over a large range of μ. Being this state paramagnetic, the DB^0 can be observed by EPR. Fig. 5.4 and Fig. 5.13a show a one-to-one correspondence between the number of paramagnetic centers and resonance intensity *as a function of* μ. The Ge DB is not predicted to be rigorously a negative-$\mathcal{U}$ center, as the average energy levels satisfy the condition $E(0/-) < 2E(+/0)$. Nevertheless, following point 3 and 4 it emerges a *quasi-negative-*$\mathcal{U}$ behavior: the broad distribution of levels results in a significant portion of centers exhibiting a $+/-$ transition due to the overlap (or even the inversion) of the $E(+/0)$ and $E(0/-)$ levels. These features are represented graphically in Fig. 5.13. Apparently it would be quite difficult to observe the EPR signal of a Ge DB corresponding to the model by Broqvist et al. (2008), as the small area under the gold curve in Fig. 5.13b suggests. Even disregarding the broadening of the charging levels, there is only a limited range of μ where the paramagnetic state is populated and, at optimal μ positioning, too, only a fraction of the DBs can be neutral. From the EPR point of view, the situation is much worse in the realistic case where broadening occurs. As shown in the inset of Fig. 5.13b, the majority of the centers exhibit a $+/-$ transition even when $E(-/0) \gtrsim 2E(0/+)$. Therefore the number of paramagnetic DB^0 is a tiny fraction of the total number.

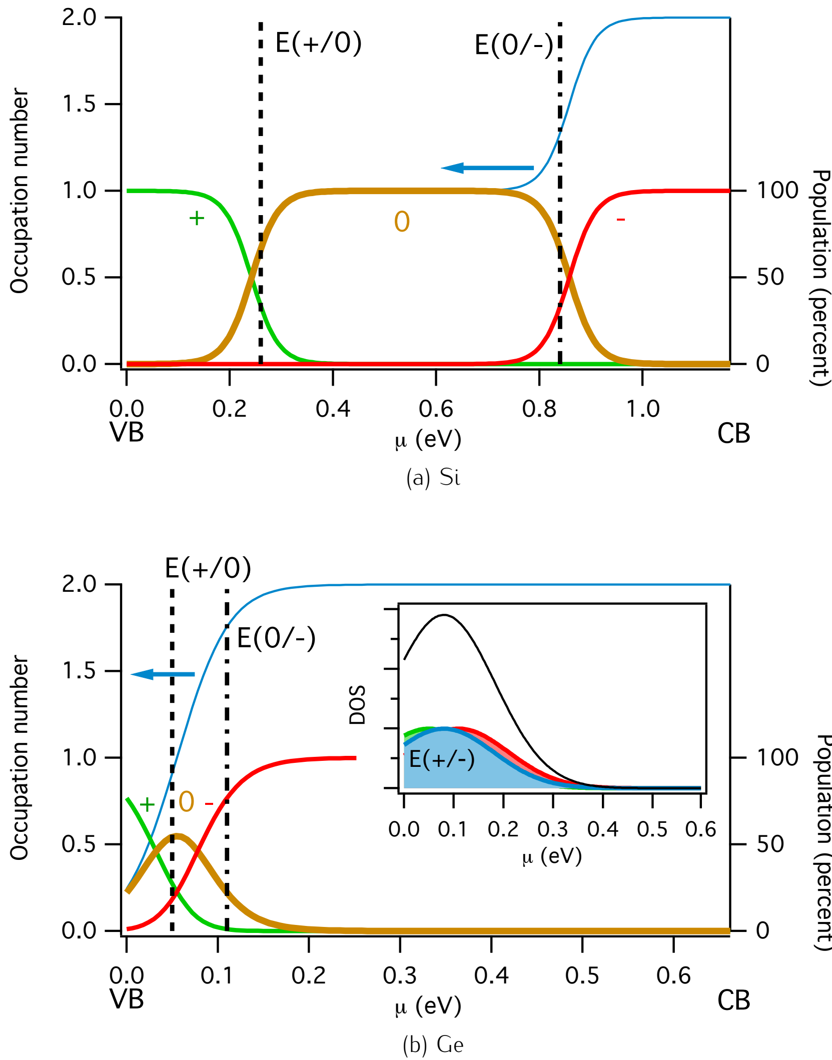

Figure 5.13: Population of the different charge levels (right axis) and occupation number (left axis) as a function of the chemical potential for the DB in Si (a) and Ge (b), drawn for $T = 300\,\mathrm{K}$ and no level broadening. The population for the $+$, 0, $-$ levels is given by Eq. 1.15, where $n^{+} \equiv n_0$, $n^{0} \equiv n_1$, and $n^{-} \equiv n_2$. The occupation number is the ensamble average of the number of electrons bound to the DB and equals $n^0 + 2n^-$. The inset in (b) shows the break down of density of states (DOS) in terms of the transition levels +/0 (red), 0/− (green), and +/− (blue). Level broadening is taken as 0.1 eV, as observed for the P_b center in silicon, but in germanium it could be substantially larger due to the vicinity of VB edge. The position of the DB charging levels of Si and Ge is taken from Poindexter et al. (1984) and Broqvist et al. (2008), respectively.

At this point, it is plausible to wonder if it is really possible to observe paramagnetic resonance from negative-$\mathcal{U}$ dangling bonds. In the attempt to address this non trivial question, it must be taken into account that in this work of thesis the EDMR signal from Ge DBs has been observed, indicating that a paramagnetic state necessarily exists. The apparent contradiction is resolved by examining the details of the EDMR spectroscopy. In fact, a distinctive feature of EDMR operated in the contactless mode is the use of larger than bandgap light to generate carriers and to reveal the variation of the photocurrent induced by the resonance.

Light is the point to solve the above mentioned apparent discrepancy.

Negative-$\mathcal{U}$ centers that are present in silicon, such as the bulk vacancy and the interstitial boron, can be observed by EPR spectroscopy using light to excite the defects to the metastable paramagnetic state (Watkins, 1975; Watkins and Troxell, 1980; Troxell and Watkins, 1980). In the case of the Ge DBs, both the **enhanced sensitivity** of the electrical detection *and* the **illumination** played a role in the unprecedented observation of the paramagnetic resonance.

Besides EDMR data, other experimental facts concur with the DB model described above. First of all, the anomalous behavior of the characteristic time of the interface traps in the lower half of the bandgap strongly suggest that two electrons are involved in the capture and emission process. Otherwise, in order to account for the experimental data, the capture cross section had to depend exponentially on the energy depth (with the unrealistic consequence of a cross section at midgap being three order of magnitude larger than at the band edge). Centers with the same structure are expected to have similar capture cross section despite the shift in energy positioning induced by interface disorder and it would be difficult to justify such an ample variation.

On the other hand, the capture cross section is constant over the lower half of the bandgap if we assume $\alpha = 1/2$. Moreover, the magnitude of σ_p is below the typical values observed in silicon where the capture cross section $\sigma_{p,n}^{\mathrm{Si}} \approx 10^{15}\,\mathrm{cm}^2$ (Nicollian and Goetzberger, 1967). This fact may be related to the necessity of exchanging two carriers in a single event, instead of one, with a consequent reduction of the cross section.

Additionally, the negative-$\mathcal{U}$ model of the DB can explain the featureless U-shaped D_{it} obtained by admittance analysis, reported both in this thesis and in the literature. The large broadening of the charging levels, induced by the vicinity of the VB, effectively spreads out the DB peak, that becomes almost indistinguishable from the continuum background.

The location of the charging levels close to the VB is supported by measurements of the position of the charge neutrality level (CNL), defined as the crosspoint at which the densities of acceptor-like and donor-like interface states equals. Experimental works on Ge-based Schottky junctions established CNL $= 0.09$ eV above VB (Dimoulas et al., 2006; Nishimura et al., 2007). It is known that CNL is related to the position of the charging levels, as discussed by Tersoff (1984), giving additional quantitative substantiation to the model.

Theoretical calculations predict the existence of other centers with negative-$\mathcal{U}$ character in the close vicinity of the Ge interface, such as valence alternation pairs located in the interfacial GeO_x suboxide (Binder et al., 2012). These defects may act as trapping centers and concur to the broad D_{it} background. The presence of negative-$\mathcal{U}$ centers has been observed in silicon by Dobaczewski et al. (2008) while studying the emission properties of the silicon DBs at the (001) interface. This characteristic was tentatively associated with a P_{b1} center.

A last striking argument supports the negative-$\mathcal{U}$ model for the Ge DB. Trying to replicate the remarkable success of the hydrogen passivation for the defects at the interface between silicon and silicon oxide, many attempts failed in obtaining comparable results at the germanium counterpart. Defects in Ge appear to be resistant to H passivation (Afanas'ev et al., 2005). According to detailed calculations (Weber et al., 2007), hydrogen diffusing through germanium is in a negatively charged state. In the negative-$\mathcal{U}$ model, Ge DB is prevalently in the DB^- state and therefore, H^- can not saturate the dangling bond. Additionally, the theoretical calculations attributing a negative-$\mathcal{U}$ character to the DB predict that the formation of Ge-H bonds leads to little structure relaxation with negligible energy gain. The stronger O-H bond would then be favored on an energetic ground promoting Ge-H dissociation (Tsetseris and Pantelides, 2009, 2011; Houssa et al., 2011).

In conclusion, the discovery of the trigonal symmetry of the Ge DB at the (111)Ge/GeO_2 interface and the identification of a P_b-like microstructure by EDMR spectroscopy opened the question of the DB positioning inside the bandgap. Admittance spectroscopy does not yield a direct evidence of localized energy levels but indicates that the electrical activity of the traps has a differing capture and emission dynamics from what is observed at the Si/SiO_2 interface. Stimulated by the absence of the EPR identification of the interface Ge DB, a negative-$\mathcal{U}$ model has been considered, in accordance with theoretical modeling of the Ge-related interfaces and experimental evidences as well. The model recognizes the key role of the light in enabling the detection of the paramagnetic resonance, by effectively populating the active DB^0 state. On the contrary, even employing suitable light, conventional EPR lacks the sensitivity required to detect interface defects. The size of a sample that can fit into a microwave cavity is of the order of $0.5\,\text{cm}^2 \times 0.1\,\text{cm}$. Typically many slices are packed to increase the interface area inside the cavity, up to a factor 20, but this prevents the use of above bandgap light to illuminate the whole surface. Observing the resonance of negative-$\mathcal{U}$ interface centers by conventional EPR will not be trivial.
The results of admittance spectroscopy fit well with the proposed picture. The anomalous dependence of the time constant as a function of the surface potential, observed in this thesis, is naturally explained as the effect of the emission and capture of two carriers in a single charge state transition. The smooth and U-shaped D_{it} results from the large broadening of the charging levels due to the vicinity of the VB tail states, in addition to the intrinsic chemical and electrostatic disorder occurring at the interface. The location of the charging levels in the lower half of the bandgap is confirmed by independent experiments, such as measurements of the CNL.

5.4 Bibliography

Valery V. Afanas'ev, Y. G. Fedorenko, and A. Stesmans. Interface traps and dangling-bond defects in (100)Ge/HfO2. *Applied Physics Letters*, 87(3):032107, 2005. ISSN 00036951. doi: 10.1063/1.1947372. URL http://link.aip.org/link/APPLAB/v87/i3/p032107/s1&Agg=doi.

P. W. Anderson. Model for the Electronic Structure of Amorphous Semiconductors. *Physical Review Letters*, 34(15):953–955, April 1975. ISSN 0031-9007. doi: 10.1103/PhysRevLett.34.953. URL http://link.aps.org/doi/10.1103/PhysRevLett.34.953.

P. Asoka-Kumar, K. G. Lynn, and D. O. Welch. Characterization of defects in Si and SiO2-Si using positrons. *Journal of Applied Physics*, 76(9):4935, November 1994. ISSN 00218979. doi: 10.1063/1.357207. URL http://scitation.aip.org/content/aip/journal/jap/76/9/10.1063/1.357207.

Silvia Baldovino, Alessandro Molle, and Marco Fanciulli. Evidence of dangling bond electrical activity at the Ge/oxide interface. *Applied Physics Letters*, 93(24):242105, 2008. ISSN 00036951. doi: 10.1063/1.3050451. URL http://link.aip.org/link/APPLAB/v93/i24/p242105/s1&Agg=doi.

G. Baraff, E. Kane, and M. Schlüter. Theory of the silicon vacancy: An Anderson negative-U system. *Physical Review B*, 21(12):5662–5686, June 1980. ISSN 0163-1829. doi: 10.1103/PhysRevB.21.5662. URL http://link.aps.org/doi/10.1103/PhysRevB.21.5662.

Florence Bellenger, Brice De Jaeger, C Merckling, Michel Houssa, Julien Penaud, Laura Nyns, E. Vrancken, Matty Caymax, Thomas Hoffmann, K. De Meyer, and Marc Heyns. High FET Performance for a Future CMOS GeO2 - Based Technology. *IEEE Electron Device Letters*, 31(5):402–404, 2010. URL https://lirias.kuleuven.be/handle/123456789/286389.

Jan Felix Binder, Peter Broqvist, and Alfredo Pasquarello. Electron trapping in substoichiometric germanium oxide. *Applied Physics Letters*, 97(9):092903, 2010. ISSN 00036951. doi: 10.1063/1.3486175. URL http://link.aip.org/link/APPLAB/v97/i9/p092903/s1&Agg=doi.

Jan Felix Binder, Peter Broqvist, and Alfredo Pasquarello. Stability of valence alternation pairs across the substoichiometric region at Ge / GeO 2 interfaces. *Physica B: Physics of Condensed Matter*, 407(15):2939–2942, 2012. ISSN 0921-4526. doi: 10.1016/j.physb.2011.08.075. URL http://dx.doi.org/10.1016/j.physb.2011.08.075.

P Bokes, I Štich, and L Mitas. Ground-state reconstruction of the Si (0 0 1) surface : symmetric versus buckled dimers. *Chemical physics letters*, 362(August):559–566, 2002. URL http://www.sciencedirect.com/science/article/pii/S0009261402010813.

Peter Broqvist, Audrius Alkauskas, and Alfredo Pasquarello. Defect levels of dangling bonds in silicon and germanium through hybrid functionals. *Physical Review B*, 78(7):075203, August 2008. ISSN 1098-0121. doi: 10.1103/PhysRevB.78.075203. URL http://link.aps.org/doi/10.1103/PhysRevB.78.075203.

Peter Broqvist, Jan Felix Binder, and Alfredo Pasquarello. Atomistic model structure of the Ge(100)-GeO2 interface. *Microelectronic Engineering*, 86(7-9):1589–1591, July 2009. ISSN 01679317. doi: 10.1016/j.mee.2009.03.087. URL http://linkinghub.elsevier.com/retrieve/pii/S0167931709002500.

Peter Broqvist, Jan Felix Binder, and Alfredo Pasquarello. First principles study of electronic and structural properties of the Ge/GeO2 interface. *Physica B: Condensed Matter*, 407(15):2926–2931, August 2012. ISSN 09214526. doi: 10.1016/j.physb.2011.08.037. URL http://linkinghub.elsevier.com/retrieve/pii/S0921452611007903.

K. L. Brower. Strain Broadening of the Dangling-Bond Resonance at the (111)Si-SiO2 Interface. *Physical Review B*, 33(7):4471, 1986. URL http://prb.aps.org/abstract/PRB/v33/i7/p4471_1.

Chi On Chui, Shriram Ramanathan, Baylor B Triplett, Paul C Mcintyre, and Krishna C Saraswat. Germanium MOS Capacitors Incorporating Ultrathin high-k gate dielectric. *IEEE Electron Device Letters*, 23(8):473–475, 2002.

Athanasios Dimoulas, P. Tsipas, A. Sotiropoulos, and E. K. Evangelou. Fermi-level pinning and charge neutrality level in germanium. *Applied Physics Letters*, 89(25):252110, 2006. ISSN 00036951. doi: 10.1063/1.2410241. URL http://link.aip.org/link/APPLAB/v89/i25/p252110/s1&Agg=doi.

L. Dobaczewski, S. Bernardini, P. Kruszewski, P. K. Hurley, V. P. Markevich, I. D. Hawkins, and a. R. Peaker. Energy state distributions of the Pb centers at the (100), (110), and (111) Si/SiO2 interfaces investigated by Laplace deep level transient spectroscopy. *Applied Physics Letters*, 92(24):242104, 2008. ISSN 00036951. doi: 10.1063/1.2939001. URL http://link.aip.org/link/APPLAB/v92/i24/p242104/s1&Agg=doi.

Marco Fanciulli, Omar Costa, Simone Cocco, Gabriele Seguini, Enrico Prati, and Giovanna Scarel. Defects in High-κ Gate Dielectric Stacks. In *NATO Advanced Studies Institute, Series II: Mathematics, Physics and Chemistry*, page 26. Plenum, New York, 2005.

T. Graf, T. Ishikawa, K. Itoh, E. Haller, M. Stutzmann, and M. Brandt. Hyperfine interactions at dangling bonds in amorphous germanium. *Physical Review B*, 68(20):205208, November 2003. ISSN 0163-1829. doi: 10.1103/PhysRevB.68.205208. URL http://link.aps.org/doi/10.1103/PhysRevB.68.205208.

Oguzhan Gurlu, Harold Zandvliet, and Bene Poelsema. Electronic Properties of (2x1) and c(4x2) Domains on Ge(001) Studied by Scanning Tunneling Spectroscopy. *Physical Review Letters*, 93(6):066101, August 2004. ISSN 0031-9007. doi: 10.1103/PhysRevLett.93.066101. URL http://link.aps.org/doi/10.1103/PhysRevLett.93.066101.

Felix Hoehne, Jinming Lu, Andre Stegner, Martin Stutzmann, Martin Brandt, Martin Rohrmüller, Wolf Schmidt, and Uwe Gerstmann. Electrically Detected Electron-Spin-Echo Envelope Modulation: A Highly Sensitive Technique for Resolving Complex Interface Structures. *Physical Review Letters*, 106(19):196101, May 2011. ISSN 0031-9007. doi: 10.1103/PhysRevLett.106.196101. URL http://link.aps.org/doi/10.1103/PhysRevLett.106.196101.

M. Houssa, G. Pourtois, M. Caymax, M. Meuris, M. M. Heyns, Valery V. Afanas'ev, and A. Stesmans. Ge dangling bonds at the (100)Ge/GeO[sub 2] interface and the viscoelastic properties of GeO[sub 2]. *Applied Physics Letters*, 93(16):161909, 2008. ISSN 00036951. doi: 10.1063/1.3006320. URL http://link.aip.org/link/APPLAB/v93/i16/p161909/s1&Agg=doi.

M. Houssa, G. Pourtois, Valery V. Afanas'ev, and A. Stesmans. First-principles study of Ge dangling bonds in GeO2 and correlation with electron spin resonance at Ge/GeO2 interfaces. *Applied Physics Letters*, 99(21):212103, 2011. ISSN 00036951. doi: 10.1063/1.3662860. URL http://link.aip.org/link/APPLAB/v99/i21/p212103/s1&Agg=doi.

Yoshiki Kamata. High-k/Ge MOSFETs for Future Nanoelectronics. *Materials Today*, 11 (1-2):30–38, January 2008. ISSN 13697021. doi: 10.1016/S1369-7021(07)70350-4. URL http://linkinghub.elsevier.com/retrieve/pii/S1369702107703504.

K. Kasahara, S. Yamada, T. Sakurai, K. Sawano, H. Nohira, M. Miyao, and K. Hamaya. Reliable reduction of Fermi-level pinning at atomically matched metal/Ge interfaces by sulfur treatment. *Applied Physics Letters*, 104(17):172109, April 2014. ISSN 0003-6951. doi: 10.1063/1.4875016. URL http://scitation.aip.org/content/aip/journal/apl/104/17/10.1063/1.4875016.

K. Keunen, A. Stesmans, and Valery V. Afanas'ev. Inherent Si dangling bond defects at the thermal (110)Si/SiO_{2} interface. *Physical Review B*, 84(8):085329, August 2011. ISSN 1098-0121. doi: 10.1103/PhysRevB.84.085329. URL http://link.aps.org/doi/10.1103/PhysRevB.84.085329.

Duygu Kuzum, Abhijit J Pethe, Tejas Krishnamohan, and Krishna C Saraswat. Ge (100) and (111) N- and P-FETs With High Mobility and Low-T Mobility Characterization. *IEEE Transaction on Electron Devices*, 56(4):648–655, 2009.

S. Lebib, M. Schoisswohl, J. L. Cantin, and H. J. von Bardeleben. SiGe/SiGeO2 interface defects. *Thin Solid Films*, 294:242–245, 1997.

CH Lee, Tomonori Nishimura, Toshiyuki Tabata, Kosuke Nagashio, Koji Kita, and Akira Toriumi. Variation of Surface Roughness on Ge Substrate by Cleaning in Deionized Water and its Influence on Electrical Properties in Ge Metal–Oxide–Semiconductor Field-. *Japanese journal of Applied Physics*, 51:104203, October 2012. ISSN 0021-4922. doi: 10.1143/JJAP.51.104203. URL http://jjap.jsap.jp/link?JJAP/51/104203/http://adsabs.harvard.edu/abs/2012JaJAP..51j4203L.

DC Look. Statistics of multicharge centers in semiconductors: Applications. *Physical Review B*, 24(10):5852, 1981. URL http://prb.aps.org/abstract/PRB/v24/i10/p5852_1.

Koen Martens, Chi On Chui, Guy Brammertz, Brice De Jaeger, Duygu Kuzum, Marc Meuris, Marc Heyns, Tejas Krishnamohan, Krishna Saraswat, Herman E. Maes, and Guido Groeseneken. On the Correct Extraction of Interface Trap Density of MOS Devices With High-Mobility Semiconductor Substrates. *IEEE Transactions on Electron Devices*, 55(2):547–556, February 2008. ISSN 0018-9383. doi: 10.1109/TED.2007.912365. URL http://ieeexplore.ieee.org/lpdocs/epic03/wrapper.htm?arnumber=4436002.

Alessandro Molle, Silvia Baldovino, Marco Fanciulli, Dimitra Tsoutsou, Evangelos Golias, and Athanasios Dimoulas. Impact of post deposition annealing in the electrically active traps at the interface between Ge(001) substrates and LaGeOx films grown by molecular beam deposition. *Journal of Applied Physics*, 110(8):084504, October 2011. ISSN 00218979. doi: 10.1063/1.3651400. URL http://scitation.aip.org/content/aip/journal/jap/110/8/10.1063/1.3651400http://link.aip.org/link/JAPIAU/v110/i8/p084504/s1&Agg=doi.

S.N.a. Murad, P.T. Baine, D.W. McNeill, S.J.N. Mitchell, B.M. Armstrong, M. Modreanu, G. Hughes, and R.K. Chellappan. Optimisation and scaling of interfacial GeO2 layers for high-κ gate stacks on germanium and extraction of dielectric constant of GeO2. *Solid-State Electronics*, 78:136–140, December 2012. ISSN 00381101. doi: 10.1016/j.sse.2012.05.048. URL http://linkinghub.elsevier.com/retrieve/pii/S0038110112001852.

A.P.D. Nguyen, A. Stesmans, Valery V. Afanas'ev, R.R. Lieten, and G. Borghs. Observation of a paramagnetic defect at the epitaxial Ge3N4/(111)Ge interface by electron spin resonance. *Thin Solid Films*, 518(9):2361–2364, February 2010. ISSN 00406090. doi: 10.1016/j.tsf.2009.09.181. URL http://linkinghub.elsevier.com/retrieve/pii/S0040609009017763.

E.H. Nicollian and J.R. Brews. *MOS (Metal Oxide Semiconductor) Physics and Technology*. A Wiley-Interscience publication. Wiley, 2003. ISBN 9780471430797. URL http://books.google.it/books?id=HaRwngEACAAJ.

EH Nicollian and A Goetzberger. The Si-SiO2 Interface-Electrical Properties as Determined by the Metal-Insulator-Silicon Conductance Technique. *Bell System Technical Journal*, 46:1055, 1967. URL http://onlinelibrary.wiley.com/doi/10.1002/j.1538-7305.1967.tb01727.x/abstract.

Tomonori Nishimura, Koji Kita, and Akira Toriumi. Evidence for strong Fermi-level pinning due to metal-induced gap states at metal/germanium interface. *Applied Physics Letters*, 91(12):123123, September 2007. ISSN 00036951. doi: 10.1063/1.2789701. URL http://scitation.aip.org/content/aip/journal/apl/91/12/10.1063/1.2789701.

Stefano Paleari, Silvia Baldovino, Alessandro Molle, and Marco Fanciulli. Evidence of Trigonal Dangling Bonds at the Ge(111)/Oxide Interface by Electrically Detected Magnetic Resonance. *Physical Review Letters*, 110(20):206101, May 2013. ISSN 0031-9007. doi: 10.1103/PhysRevLett.110.206101. URL http://link.aps.org/doi/10.1103/PhysRevLett.110.206101.

Stefano Paleari, A. Molle, F. Accetta, A. Lamperti, E. Cianci, and M. Fanciulli. Electrically detected magnetic resonance study of the Ge dangling bonds at the Ge(111)/GeO2 interface after capping with Al2O3 layer. *Applied Surface Science*, 291:3–5, February 2014. ISSN 01694332. doi: 10.1016/j.apsusc.2013.09.121. URL http://www.sciencedirect.com/science/article/pii/S0169433213017625.

Alfredo Pasquarello, MS Hybertsen, and R Car. Interface structure between silicon and its oxide by first-principles molecular dynamics. *Nature*, 396(November):58, 1998. URL http://www.nature.com/nature/journal/v396/n6706/abs/396058a0.html.

E. H. Poindexter, G. J. Gerardi, M.-E. Rueckel, P. J. Caplan, N. M. Johnson, and D. K. Biegelsen. Electronic traps and Pb centers at the Si/SiO2 interface: Band-gap energy distribution. *Journal of Applied Physics*, 56(10):2844, November 1984. ISSN 00218979. doi: 10.1063/1.333819. URL http://scitation.aip.org/content/aip/journal/jap/56/10/10.1063/1.333819.

Edward H. Poindexter, Philip J. Caplan, Bruce E. Deal, and Reda R. Razouk. Interface states and electron spin resonance centers in thermally oxidized (111) and (100) silicon wafers. *Journal of Applied Physics*, 52(2):879–884, 1981.

Takashi Sasada, Yosuke Nakakita, Mitsuru Takenaka, and Shinichi Takagi. Surface orientation dependence of interface properties of GeO[sub 2]/Ge metal-oxide-semiconductor structures fabricated by thermal oxidation. *Journal of Applied Physics*, 106(7):073716, 2009. ISSN 00218979. doi: 10.1063/1.3234395. URL http://link.aip.org/link/JAPIAU/v106/i7/p073716/s1&Agg=doi.

D.K. Schroder. *Semiconductor Material and Device Characterization*. Wiley, 2006. ISBN 9780471749080. URL http://books.google.it/books?id=OX2cHKJWCKgC.

S. Sioncke, H. C. Lin, G. Brammertz, A. Delabie, T. Conard, A. Franquet, M. Meuris, H. Struyf, S. De Gendt, M. Heyns, C. Fleischmann, K. Temst, A. Vantomme, M. Mueller, M. Kolbe, B. Beckhoff, and M. Caymax. Atomic Layer Deposition of High-κ Dielectrics on Sulphur-Passivated Germanium. *Journal of The Electrochemical Society*, 158(7): H687, 2011. ISSN 00134651. doi: 10.1149/1.3582524. URL http://jes.ecsdl.org/cgi/doi/10.1149/1.3582524.

P. Somers, A. Stesmans, L. Souriau, and Valery V. Afanas'ev. Electron spin resonance features of the Ge Pb1 dangling bond defect in condensation-grown (100)Si/SiO2/Si1-xGex/SiO2 heterostructures. *Journal of Applied Physics*, 112(7):074501, 2012. ISSN 00218979. doi: 10.1063/1.4748313. URL http://link.aip.org/link/JAPIAU/v112/i7/p074501/s1&Agg=doi.

A Stesmans and Valery V. Afanas'ev. Electron spin resonance features of interface defects. *Journal of Applied Physics*, 83(5):2449–2457, 1998.

A Stesmans, B Nouwen, and Valery V. Afanas'ev. hyperfine structure of the interface defect in thermal. *Journal of Physics: Condensed Matter*, 10(27):L465–L472, July 1998a. ISSN 0953-8984. doi: 10.1088/0953-8984/10/27/004. URL http://iopscience.iop.org/0953-8984/10/27/004/fulltext/.

A. Stesmans, B. Nouwen, and Valery V. Afanas'ev. Pb1 interface defect in thermal (100)Si/SiO2: 29Si hyperfine interaction. *Physical Review B*, 58(23):15801–15809, December 1998b. ISSN 0163-1829. doi: 10.1103/PhysRevB.58.15801. URL http://link.aps.org/doi/10.1103/PhysRevB.58.15801.

A. Stesmans, P. Somers, and Valery V. Afanas'ev. Nontrigonal Ge dangling bond interface defect in condensation-grown (100)Si1-xGex/SiO2. *Physical Review B*, 79(19):195301, May 2009. ISSN 1098-0121. doi: 10.1103/PhysRevB.79.195301. URL http://link.aps.org/doi/10.1103/PhysRevB.79.195301.

Andre Stesmans. Electron spin resonance of [1-11],[-111], and [11-1] oriented dangling orbital Pb0 defects at the (111) Si/SiO2 interface. *Applied Physics Letters*, 48(15): 972–974, 1986.

A. Stirling, Alfredo Pasquarello, J. Charlier, and R. Car. Dangling bond defects at Si-SiO2 interfaces: atomic structure of the P(b1) center. *Physical review letters*, 85(13):2773–6, September 2000. ISSN 1079-7114. URL http://www.ncbi.nlm.nih.gov/pubmed/10991230.

Shankar Swaminathan, Michael Shandalov, Yasuhiro Oshima, and Paul C. McIntyre. Bilayer metal oxide gate insulators for scaled Ge-channel metal-oxide-semiconductor devices. *Applied Physics Letters*, 96(8):082904, 2010. ISSN 00036951. doi: 10.1063/1.3313946. URL http://link.aip.org/link/APPLAB/v96/i8/p082904/s1&Agg=doi.

S.M. Sze and K.K. Ng. *Physics of Semiconductor Devices*. Wiley, 2006. ISBN 9780470068304. URL http://books.google.it/books?id=o4unkmHBHb8C.

J. Tersoff. Schottky Barrier Heights and the Continuum of Gap States. *Physical Review Letters*, 52(6):465–468, February 1984. ISSN 0031-9007. doi: 10.1103/PhysRevLett.52.465. URL http://link.aps.org/doi/10.1103/PhysRevLett.52.465.

J. Troxell and G. Watkins. Interstitial boron in silicon: A negative-U system. *Physical Review B*, 22(2):921–931, July 1980. ISSN 0163-1829. doi: 10.1103/PhysRevB.22.921. URL http://link.aps.org/doi/10.1103/PhysRevB.22.921.

L. Tsetseris and S. T. Pantelides. Morphology and defect properties of the Ge-GeO2 interface. *Applied Physics Letters*, 95(26):262107, 2009. ISSN 00036951. doi: 10.1063/1.3280385. URL http://link.aip.org/link/APPLAB/v95/i26/p262107/s1&Agg=doi.

L. Tsetseris and S.T. Pantelides. Defect formation and annihilation at interfaces. *Microelectronic Engineering*, 88(4):395–398, April 2011. ISSN 01679317. doi: 10.1016/j.mee.2010.08.027. URL http://linkinghub.elsevier.com/retrieve/pii/S0167931710003291.

Dong Wang, Shuta Kojima, Keita Sakamoto, Keisuke Yamamoto, and Hiroshi Nakashima. An accurate characterization of interface-state by deep-level transient spectroscopy for Ge metal-insulator-semiconductor capacitors with SiO2/GeO2 bilayer passivation. *Journal of Applied Physics*, 112(8):083707, 2012. ISSN 00218979. doi: 10.1063/1.4759139. URL http://link.aip.org/link/JAPIAU/v112/i8/p083707/s1&Agg=doi.

G. Watkins. Defects in irradiated silicon: EPR and electron-nuclear double resonance of interstitial boron. *Physical Review B*, 12(12):5824–5839, December 1975. ISSN 0556-2805. doi: 10.1103/PhysRevB.12.5824. URL http://link.aps.org/doi/10.1103/PhysRevB.12.5824.

G. Watkins and J. Troxell. Negative-U Properties for Point Defects in Silicon. *Physical Review Letters*, 44(9):593–596, March 1980. ISSN 0031-9007. doi: 10.1103/PhysRevLett.44.593. URL http://link.aps.org/doi/10.1103/PhysRevLett.44.593.

J. Weber, A. Janotti, and C. Van de Walle. Dangling bonds and vacancies in germanium. *Physical Review B*, 87(3):035203, January 2013. ISSN 1098-0121. doi: 10.1103/PhysRevB.87.035203. URL http://link.aps.org/doi/10.1103/PhysRevB.87.035203.

J. R. Weber, a. Janotti, P. Rinke, and C. G. Van de Walle. Dangling-bond defects and hydrogen passivation in germanium. *Applied Physics Letters*, 91(14):142101, 2007. ISSN 00036951. doi: 10.1063/1.2793184. URL http://link.aip.org/link/APPLAB/v91/i14/p142101/s1&Agg=doi.

H. Zandvliet. Energetics of Si(001). *Reviews of Modern Physics*, 72(2):593–602, April 2000. ISSN 0034-6861. doi: 10.1103/RevModPhys.72.593. URL http://link.aps.org/doi/10.1103/RevModPhys.72.593.

Harold J.W. Zandvliet. The Ge(001) surface. *Physics Reports*, 388(1):1–40, December 2003. ISSN 03701573. doi: 10.1016/j.physrep.2003.09.001. URL http://linkinghub.elsevier.com/retrieve/pii/S037015730300334X.

R. Zhang, T. Iwasaki, N. Taoka, M. Takenaka, and S. Takagi. Impact of GeOx interfacial layer thickness on Al2O3/Ge MOS interface properties. *Microelectronic Engineering*, 88(7):1533–1536, July 2011. ISSN 01679317. doi: 10.1016/j.mee.2011.03.130. URL http://linkinghub.elsevier.com/retrieve/pii/S0167931711003893.

ME Zvanut and WE Carlos. Interfacial point defects in heavily implanted silicon germanium alloys. *Journal of Vacuum Science & Technology B: Microelectronics and Nanometer Structures*, 10(4):2026–2029, 1992. URL http://ieeexplore.ieee.org/xpls/abs_all.jsp?arnumber=4962130.

Conclusions and Outlook 6

E quindi uscimmo a riveder le stelle.
Inferno XXXIV, 139
Dante Alighieri

Germanium has been the subject of a renewed interest as a promising material for future electronic devices. In particular its integration as channel material in CMOS architectures would be beneficial to operation speed, thanks to one of the highest hole mobility among semiconductors. Nevertheless, in real devices it is essential that the excellent property of the bulk are retained at the interfaces, where the devices are actually built. Despite many decades of efforts, the realization of the performance promises has been hindered by the poor quality of the interface and the lack of effective passivation strategies.
The experimental work undertaken in this thesis did not aim at achieving groundbreaking records in the new lowest-possible D_{it} or in the highest-ever seen mobility, but a deeper understanding of the fundamental structure and electronic properties of the interface centers. Motivated by the necessity of a deeper understanding of the physical nature of the interface traps that are responsible for the performance degradation, several germanium – oxides interfaces have been investigated by Electrically Detected Magnetic Resonance (EDMR) spectroscopy.
After the recent observation of germanium dangling bonds (DBs) at the (001) oriented Ge/GeO_2 interface by Baldovino et al. (2008), the (111) oriented Ge/GeO_2 interface was studied. That is, indeed, the most interesting for MOSFET application due to the inherent higher mobility according to band structure theory and experimental observations Kuzum et al. (2009). EDMR measurements led to the unprecedented identification of a Ge DB with trigonal symmetry and principal axis oriented along the [111] direction (Paleari et al., 2013), similar to the well characterized Si P_b center. In contrast with this result, the (001)Ge/GeO_2 interface does not reveal the trigonal center, analogous to the P_{b0} observed at the (001)Si/SiO_2 interface, but a dangling bond with a lower point symmetry. This fact is rationalized in terms of suboxide interface rearrangement and oxide viscoelasticity. The suboxide rearrangement at the (001) interface promotes the generation of the non-axial centers at distorted dimers, while the viscoelasticity of the germanium oxide impedes the occurrence of the trigonal centers, which are located at monolayer steps.
Moving from the identification of the microstructure features, the complementary study of

the electrical properties in both surface orientations was undertaken. Accurate characterizations require the fabrication of Metal-Oxide-Semiconductor (MOS) capacitors with low gate leakage. The gate stack comprising a thermal grown GeO_2 layer and a Atomic Layer Deposited Al_2O_3 capping was chosen as the better compromise in terms of performance and simplicity. X-ray Photoemission Spectroscopy (XPS) and Time-of-Flight Secondary Ion Mass Spectrometry (ToF-SIMS) attested the chemical and compositional consistency between the as grown and the capped GeO_2. EDMR confirmed that the structure of the trigonal Ge DBs and local stress distribution are not affected by the capping (Paleari et al., 2014).
Supported by the preliminary work, p- and n- type MOS capacitors fabricated on (001) and (111) substrate were characterized by admittance spectroscopy in the temperature range $300-110$ K. Consistently with the current literature (Afanas'ev et al., 2005; Kuzum et al., 2009; Lee et al., 2012), the density of interface traps D_{it} as a function of energy results in a smooth U-shaped curve. It is not possible to recognize the specific features of energy localized levels, such as in the case of the Si DBs (Poindexter et al., 1984).
Other germanium interfaces have been investigated. EDMR spectroscopy detected the trigonal Ge DB at the untreated (111)Ge/Al_2O_3 interface, possibly due to the presence of a suboxide GeO_x transition layer. The DB signature has been found also when the Ge surface was treated with ammonium sulfide prior to the Al_2O_3 deposition. Admittance spectroscopy demonstrated the good properties of thermal GeO_2 in terms of D_{it}, unparalleled in the direct Ge/Al_2O_3 interface, especially in the upper half region of the bandgap. Ammonium sulfide treatment is effective in reducing the defect density at the interface, but the GeO_2 performance are, on the whole, superior. As a general trend, it is observed a slightly higher D_{it} in (111)-oriented substrates with respect to (001)-oriented substrates.
Analyzing in detail the admittance curves of p-type Ge/GeO_2 MOS capacitors, an anomalous behavior has been recognized. The characteristics of the response time of interface traps, as the chemical potential is swept from the valence band to midgap, hints at double electron occupancy statistic for the electrically active defects.
A negative-$\mathcal{U}$ model is invoked to explain the experimental facts that emerged from the EDMR and admittance spectroscopy investigations, together with the information available in the literature. This phenomenological model is able to explain the observation of the DB resonance by the contactless EDMR technique and the concurrent absence of EPR signals by recognizing the key role of the light in effectively populating the paramagnetic DB^0 state. Also, the anomalous trapping dynamics is explained in a natural way as the effect of the emission and capture of two carriers in a single charge state transition. The smooth and U-shaped D_{it} is the result of the large broadening of the charging levels due to the vicinity of the VB tail states and the inherent chemical and electrostatic disorder occurring at the interface.

Future work will be directed to refine the present conclusions. In particular, to reduce the error bar in admittance results by improved determination of the doping level in the close vicinity of the interface. This represents the main source of uncertainty in the present analysis. This aim will be prosecuted by resorting to advanced local characterization techniques, *e.g.* dynamic SIMS measurement with the aid of calibrated standards. This technique is accredited to enable 1 - 5 % relative error on dopant concentration in the range of interest, well beneath the present confidence level.
Further experimental tests of the negative-$\mathcal{U}$ model can involve other electrical spectroscopies such as Deep Level Transient Spectroscopy. For a successful investigation of

surface states DLTS should be operated in constant capacitance mode to avoid artefacts induced by high trap densities and resort to Laplace transform to extract carrier emission dynamics at fixed temperatures (Dobaczewski et al., 2008).
On the other hand, it will be interesting to explore the role of the light in populating the paramagnetic DB^0 state. By tuning the excitation wavelength, it could be possible to find a threshold for the photo-induced reaction $DB^- \rightarrow DB^0 + e$ and infer an energy level of the metastable neutral state. Complementary, applying light pulses and observing the decay of the DB^0 population could be a viable alternative to gain an insight into the energy difference between the excited and the ground states.
In view of a general deployment of EDMR as a tool for interface defects characterization, the spectroscopic resolution in probing selectively the DB centers can be exploited to evaluate the efficiency of novel passivation strategies. Passivation schemes based on sulfur already showed promising results (Kasahara et al., 2014), and in the future they may be tailored to specifically target Ge DBs.
The ultimate playground for interface defect characterization, in terms of both structural and electronic properties, would be a fully processed MOSFET with a transparent gate electrode. This architecture will enable EDMR admittance, and transient spectroscopies as a function of excitation wavelength on the same device with an unprecedented experimental freedom.

This, is just the beginning.

6.1 Bibliography

Valery V. Afanas'ev, Y. G. Fedorenko, and A. Stesmans. Interface traps and dangling-bond defects in (100)Ge/HfO2. *Applied Physics Letters*, 87(3):032107, 2005. ISSN 00036951. doi: 10.1063/1.1947372. URL http://link.aip.org/link/APPLAB/v87/i3/p032107/s1&Agg=doi.

Silvia Baldovino, Alessandro Molle, and Marco Fanciulli. Evidence of dangling bond electrical activity at the Ge/oxide interface. *Applied Physics Letters*, 93(24):242105, 2008. ISSN 00036951. doi: 10.1063/1.3050451. URL http://link.aip.org/link/APPLAB/v93/i24/p242105/s1&Agg=doi.

L. Dobaczewski, S. Bernardini, P. Kruszewski, P. K. Hurley, V. P. Markevich, I. D. Hawkins, and a. R. Peaker. Energy state distributions of the Pb centers at the (100), (110), and (111) Si/SiO2 interfaces investigated by Laplace deep level transient spectroscopy. *Applied Physics Letters*, 92(24):242104, 2008. ISSN 00036951. doi: 10.1063/1.2939001. URL http://link.aip.org/link/APPLAB/v92/i24/p242104/s1&Agg=doi.

K. Kasahara, S. Yamada, T. Sakurai, K. Sawano, H. Nohira, M. Miyao, and K. Hamaya. Reliable reduction of Fermi-level pinning at atomically matched metal/Ge interfaces by sulfur treatment. *Applied Physics Letters*, 104(17):172109, April 2014. ISSN 0003-6951. doi: 10.1063/1.4875016. URL http://scitation.aip.org/content/aip/journal/apl/104/17/10.1063/1.4875016.

Duygu Kuzum, Abhijit J Pethe, Tejas Krishnamohan, and Krishna C Saraswat. Ge (100) and (111) N- and P-FETs With High Mobility and Low-T Mobility Characterization. *IEEE Transaction on Electron Devices*, 56(4):648–655, 2009.

CH Lee, Tomonori Nishimura, Toshiyuki Tabata, Kosuke Nagashio, Koji Kita, and Akira Toriumi. Variation of Surface Roughness on Ge Substrate by Cleaning in Deionized Water and its Influence on Electrical Properties in Ge Metal–Oxide–Semiconductor Field-. *Japanese journal of Applied Physics*, 51:104203, October 2012. ISSN 0021-4922. doi: 10.1143/JJAP.51.104203. URL http://jjap.jsap.jp/link?JJAP/51/104203/http://adsabs.harvard.edu/abs/2012JaJAP..51j4203L.

Stefano Paleari, Silvia Baldovino, Alessandro Molle, and Marco Fanciulli. Evidence of Trigonal Dangling Bonds at the Ge(111)/Oxide Interface by Electrically Detected Magnetic Resonance. *Physical Review Letters*, 110(20):206101, May 2013. ISSN 0031-9007. doi: 10.1103/PhysRevLett.110.206101. URL http://link.aps.org/doi/10.1103/PhysRevLett.110.206101.

Stefano Paleari, A. Molle, F. Accetta, A. Lamperti, E. Cianci, and M. Fanciulli. Electrically detected magnetic resonance study of the Ge dangling bonds at the Ge(111)/GeO2 interface after capping with Al2O3 layer. *Applied Surface Science*, 291:3–5, February 2014. ISSN 01694332. doi: 10.1016/j.apsusc.2013.09.121. URL http://www.sciencedirect.com/science/article/pii/S0169433213017625.

E. H. Poindexter, G. J. Gerardi, M.-E. Rueckel, P. J. Caplan, N. M. Johnson, and D. K. Biegelsen. Electronic traps and Pb centers at the Si/SiO2 interface: Band-gap energy distribution. *Journal of Applied Physics*, 56(10):2844, November 1984. ISSN 00218979.

doi: 10.1063/1.333819. URL http://scitation.aip.org/content/aip/journal/jap/56/10/10.1063/1.333819.

Acknowledgments
Ringraziamenti

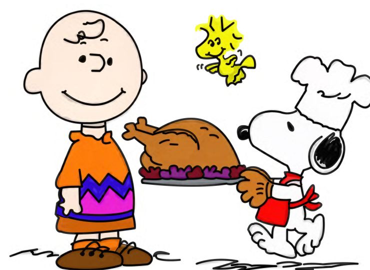

Charles M. Schulz

Questo lavoro di tesi è stato possibile grazie al contributo di molte persone, a partire dal mio relatore, il professor Marco Fanciulli, che mi ha sempre dato piena fiducia e sostegno, oltre al supporto materiale indispensabile per intraprendere l'attività di ricerca nel campo dell'EPR. Senza dimenticare le preziose *scientific discussions* che spero proseguano fruttuose.

Un ringraziamento speciale va ad Alessandro Molle, al quale devo molti dei risultati raggiunti, per aver indirizzato con successo i miei sforzi e per il sostegno continuo. Indispensabile il suo contributo alla revisione di questa tesi, per il quale ha dedicato tempo in orari molto oltre quelli *di ufficio*.

Ringrazio anche Silvia Baldovino per avermi introdotto allo studio delle interfacce germanio–ossidi (nonché per lo scatolone pieno di articoli).

Special thanks go to professor Abdelmadjid Mesli of the Institut Matériaux Microélectronique Nanosciences de Provence IM2NP, or more friendly, to Madjid, first of all for his great humanity and hospitality. His warm reception made my stay in Marseille more than confortable, like at home. I deeply acknowledge for the privilege of being introduced into the details of the Deep Level Transient Spectroscopy by one of the most important contributors to the field. His enthusiasm and the very stimulating discussions were the basis for the subsequent advances of the thesis.

Большое спасибо Яне Гуримскае, for the huge experimental work done in the two months shared at the IM2NP and for the few weekends spent visiting the city of Marseille.

Un ringraziamento doveroso è rivolto alle persone del laboratorio MDM-IMM CNR di Agrate, in particolare a Mario Alìa per la fabbricazione dei campioni, a Elena Cianci e Marcello Ghidina per le crescite ALD, a Alessio Lamperti per le misure ToF-SIMS, a Sabina Spiga per il supporto per le misure elettriche, a Roberto Fallica e a Roberto Mantovan per le misure Hall e a Flavio Volpe per l'aiuto con ogni tipo di setup elettrico. Grazie specialmente a Matteo Belli per la sua infinita disponibilità, generosità e pazienza (tre qualità indispensabili per chi si dedica all'EPR e a *sua maestà la Scienza* in generale). I suoi insegnamenti in laboratorio sono stati di notevole

valore e molto ancora mi rimane da imparare. L'aiuto di Simone Cocco si è rivelato prezioso in molte occasioni, a partire dalla cura degli spettrometri Varian e Bruker.

Dopo i ringraziamenti "istituzionali" arrivano quelli meno formali, in primo luogo indirizzati ai miei genitori Arduino e Mariella, per avermi sempre sostenuto in questi anni di dottorato e durante la scrittura della tesi – e, sì, questa è l'ultima. Davvero!

A Chiara, che mi è sempre vicina, esempio di tenacia, a volte tumultuosa; generosa e unica.

Grazie a Robi, Elena e ai due splendidi nipotini Federico e Alessandro. Grazie a mio zio Piero. E un pensiero è rivolto a mia nonna Ebe e a mia zia Maria, che mi hanno sempre incoraggiato sin da bambino.

Non possono mancare i ringraziamenti verso tutti i miei amici, quelli per cui sono "Pale", "il Pale", "il prof.", "Monza" oppure "Ste"; quelli in terra brianzola, quelli a Trieste, Monaco, Parigi, Pisa, Delft, Londra, e quelli in terra d'Alpago; quelli di sempre, quelli nuovi, quelli di passaggio.

Un grande grazie è per coloro che in questi anni di tesi sono stati per me dei compagni, non solo di laboratorio. A partire da Andrea, con il quale ho condiviso molti *venerdì di delirio*® e qualche figura nella tesi, per il fondamentale contributo al software SimpleEPR® e al *design* in laboratorio: in bocca al lupo per il tuo dottorato a Grenoble! Grazie a Federico, instancabile nelle lunghe giornate di misure elettriche e EDMR, alcune delle quali sono riportate in questa tesi. A Lorenzo, che ha affrontato vittorioso le millemila sfide della sua tesi. Alla Marty perché... Perché è la Marty, e chi la conosce lo sa! Infine grazie ai supergiovani studenti magistrali che sono passati sotto le grinfie del lab EPR.